

University of Alberta

Lag Measurement in an a-Se active matrix flat-panel imager

by

Charles Edward Schroeder



A thesis submitted to the Faculty of Graduate Studies and Research in partial fulfillment  
of the requirements for the degree of Master of Science

in

Medical Physics

Department of Physics

Edmonton, Alberta

Spring 2004



Library and  
Archives Canada

Bibliothèque et  
Archives Canada

Published Heritage  
Branch

Direction du  
Patrimoine de l'édition

395 Wellington Street  
Ottawa ON K1A 0N4  
Canada

395, rue Wellington  
Ottawa ON K1A 0N4  
Canada

*Your file* *Votre référence*  
*ISBN: 0-612-96578-3*  
*Our file* *Notre référence*  
*ISBN: 0-612-96578-3*

The author has granted a non-exclusive license allowing the Library and Archives Canada to reproduce, loan, distribute or sell copies of this thesis in microform, paper or electronic formats.

L'auteur a accordé une licence non exclusive permettant à la Bibliothèque et Archives Canada de reproduire, prêter, distribuer ou vendre des copies de cette thèse sous la forme de microfiche/film, de reproduction sur papier ou sur format électronique.

The author retains ownership of the copyright in this thesis. Neither the thesis nor substantial extracts from it may be printed or otherwise reproduced without the author's permission.

L'auteur conserve la propriété du droit d'auteur qui protège cette thèse. Ni la thèse ni des extraits substantiels de celle-ci ne doivent être imprimés ou autrement reproduits sans son autorisation.

---

In compliance with the Canadian Privacy Act some supporting forms may have been removed from this thesis.

Conformément à la loi canadienne sur la protection de la vie privée, quelques formulaires secondaires ont été enlevés de cette thèse.

While these forms may be included in the document page count, their removal does not represent any loss of content from the thesis.

Bien que ces formulaires aient inclus dans la pagination, il n'y aura aucun contenu manquant.

# Canada

## Abstract

Lag and residual contrast have been quantified in an amorphous selenium active matrix flat-panel imager as a function of frame time, kilovoltage (kV) and megavoltage (MV) x-ray photon energy and amount of incident radiation. The detector contains a 200  $\mu\text{m}$  thick a-Se layer deposited on a thin film transistor array of size 8.7 x 8.7  $\text{cm}^2$  with an 85  $\mu\text{m}$  pitch.

For all energies, the lag for the  $n=1$  and  $n=2$  frame after exposure ranges from 0.45 to 0.91 % and from 0.29 to 0.51 %, respectively. The amount of lag was determined to be a function of the time after exposure irrespective of frame time or magnitude of exposure. The lag for MV energies was slightly less than that for kV energies. The residual contrast for all energies studied ranges from 0.41 to 0.75 % and from 0.219 to 0.41 % for the  $n=1$  and  $n=2$  frame, respectively.

**But the LORD is the true God;  
He is the living God and the everlasting King.  
It is He who made the earth by His power,  
Who established the world by His wisdom;  
And by His understanding He has stretched out the heavens.**

**Jeremiah 10:10a,12**

## **To Grandma and Grandpa Schroeder**

You went to work before completing high school  
in order to help support your parents and siblings.  
You have always believed in me, encouraged me,  
prayed for me and have been amongst my greatest  
supporters in all of my post-secondary endeavors.

This work is dedicated to you.

I love you!

## **Acknowledgments**

I thank my Lord and Saviour Jesus Christ for health, strength and the ability and opportunity to study at a university graduate level. You created the world in wisdom and it is astounding!

Christine became my wife on August 2, 2003 and I revel in her love. Thank-you for believing in me, holding my hand and walking graciously with me as I completed my degree.

Thank-you to my parents Ed and Lisa Schroeder. Your prayers and encouragement helped to equip me to finish this race. Phone calls, emails and visits from my brothers James, Bryan (along with his wife Amanda) and David brought back into focus the deep commitment and friendship that is within us from growing up together. Your humour and life help to keep my perspective wide. Thank-you to my family for always believing in me.

Thank-you to my grandparents, Grandma and Grandpa Schroeder, to whom this thesis is dedicated. Your home has always been a peaceful refuge and your friendship a priceless treasure. You remind me that education is not a right but a rich and wonderful opportunity and privilege.

It has been a gift to study within the experienced Department of Medical Physics at the Cross Cancer Institute in Edmonton, Alberta. In particular I am grateful to my supervisor and the department director, Dr. Gino Fallone. I have observed and learned much from your example of leadership, communication, diligence, integrity and commitment to excellence. Your encouragement and stimulation of good judgement and initiative have traveled me further than when I first came. Thank-you to Dr. Satyapal

Rathee for the many hours spent reading manuscripts and discussing the particulars of experiment, theory and what is and is not important. Thank-you to Dr. Stephen Steciw and Teo Stanescu for many helpful discussions regarding amorphous selenium and experimental procedures and results. Thank-you to Ken Hennig and Gary Morrison in the machine shop; Len Johnson, Doug Tymofichuk, Jeff Mrochuk and Cory Lambert in the technology management group; and to Linda Harris as the Librarian in the Abdul Khaliq Library at the Cross Cancer Institute. Your many contributions made the completion of this thesis a possibility. A special thank-you to Brad Warkentin, Debbi Howorko and Charlie Kirkby for being great friends during my time at the Cross Cancer Institute.

Throughout my stay in Edmonton, particular people re-couraged me, helped to fix my car and exchanged life stories with me. These people brought wisdom, grace, and laughter into my person. The three years I lived with the Loewen family (Jace, Elvira, Calvin, Anika and Karsten) will always resonate in my memory. Thank-you for your generosity and loving-kindness. Don and Kae Neufeld as well as Neil Parker enriched my life greatly. Thank-you for your prayers, vulnerability and practical assistance. I also appreciate the companions I made at McKernan Baptist Church and the small groups that I was a part of while attending there. Thank-you for your care, encouragement and friendship.

I am very grateful to Specialized Support and Disability Services (SSDS) at the University of Alberta. Thank-you specifically to Pat Sears who put in many hours of administration and filling out application forms for the acquisition of voice recognition

software and a personal computer to assist me with the chronic tendonitis in both of my arms.

I thankfully acknowledge the Alberta Cancer Board (ACB Graduate Studentship), the Natural Sciences and Engineering Research Council of Canada (NSERC Postgraduate Scholarship A) and the University of Alberta (Walter H. Johns Graduate Fellowship) for the receipt of significant scholarships during my time as a graduate student at the University of Alberta.



## Table of Contents

<b>Chapter 1: Introduction</b> .....	<b>1</b>
1.1 Flat-Panel Detectors .....	1
1.2 Indirect and Direct Conversion Active Matrix Flat-Panel Imagers .....	2
1.3 Thesis Objectives .....	3
1.4 Notes .....	4
<b>Chapter 2: Background</b> .....	<b>10</b>
2.1 Digital Projection Radiography .....	10
2.2 Amorphous Selenium as a Photoconductor .....	15
2.2.1 The Element Selenium .....	15
2.2.2 Properties of Amorphous Selenium .....	15
2.2.3 A Brief Historical Review .....	19
2.3 Notes .....	21
<b>Chapter 3: Methods and Materials</b> .....	<b>27</b>
3.1 Amorphous Selenium Active Matrix Flat-Panel Imager .....	27
3.2 Lag and Ghosting in Diagnostic and Megavoltage Imaging .....	33
3.2.1 Lag .....	35
3.2.2 Ghosting due to Lag .....	36
3.3 Lag Measurement .....	37
3.4 Quantification of Ghosting due to Lag .....	46
3.5 Post Processing Correction for Variations in Pixel Sensitivity .....	47
3.5.1 Lag .....	47
3.5.2 Ghosting due to Lag .....	50
3.6 Notes .....	54
<b>Chapter 4: Results and Discussion</b> .....	<b>58</b>
4.1 Lag .....	58
4.2 Ghosting due to Lag .....	84
4.3 Notes .....	93
<b>Chapter 5: Conclusions</b> .....	<b>95</b>
5.1 Future Work .....	95
<b>Bibliography</b> .....	<b>96</b>
<b>Appendix</b> .....	<b>108</b>

## List of Tables

<i>Table 3.1:</i> Exposure and air kerma equivalence (corrected for temperature and pressure dependence). . . . .	p. 40
<i>Table 3.2:</i> Lag values ( $L_n$ ) for the pixel sensitivity verification experiment (6 MV, 3 MUs (250 MU/min), 7.2 s/frame) including the results for no pixel sensitivity correction and the results with pixel sensitivity correction. . . . .	p. 49
<i>Table 4.1:</i> Minimum and Maximum lag values ( $L_n$ ) for the three energies of 81 kVp, 125 kVp and 6 MV. The corresponding frame times and irradiation quantity are listed as well. . . . .	p. 80
<i>Table 4.2:</i> Approximate lag values ( $L_n$ ) measured by Polischuk <sup>3</sup> <i>et al.</i> for the a-Se thicknesses of 500 and 1000 $\mu\text{m}$ (10 to 20 V/ $\mu\text{m}$ ; both samples are biased at the same electric field). The corresponding frame number ( $n$ ) and the time after x-ray irradiation are listed as well. Our data is for 125 kVp x-rays, 5.2 s/frame, 96.0 $\mu\text{Gy}$ (11.0 mR, exposure time of 4.0 ms), 5 V/ $\mu\text{m}$ and an a-Se thickness of 200 $\mu\text{m}$ . . . . .	p. 81
<i>Table 4.3:</i> Approximate lag values for frame $n=1$ ( $L_1$ ) measured by Polischuk <sup>3</sup> <i>et al.</i> for different electric fields across the 500 $\mu\text{m}$ a-Se layer (0.03 s after x-ray irradiation, 55 keV mean beam energy, 50 mR (435 $\mu\text{Gy}$ ) delivered over 0.1 s). . . . .	p. 82
<i>Table 4.4:</i> Approximate lag values ( $L_n$ ) for frames $n=1$ to $n=5$ measured by Tsukamoto <sup>4</sup> <i>et al.</i> , for a 500 $\mu\text{m}$ thick a-Se layer with an electric field of 10 V/ $\mu\text{m}$ across the a-Se (80 kVp x-rays, 0.033 s/frame, 4.73 mR (41.3 $\mu\text{Gy}$ ), x-ray pulse width of 4 ms). Our data is for 81 kVp x-rays, 5.2 s/frame, 42.8 $\mu\text{Gy}$ (4.9 mR, exposure time of 3.2 ms), and a 200 $\mu\text{m}$ thick a-Se layer (biased by an applied electric field of 5 V/ $\mu\text{m}$ ). . . . .	p. 83
<i>Table 4.5:</i> Residual contrast ( $C_n$ ) from the ghosting experiments for frames $n=1$ and $n=2$ for three frame times. . . . .	p. 86
<i>Table A.1:</i> Complete lag measurement data for 81 kVp x-rays. . . . .	p. 108
<i>Table A.2:</i> Complete lag measurement data for 125 kVp x-rays. . . . .	p. 108
<i>Table A.3:</i> Complete lag measurement data for a 6 MV x-ray beam. . . . .	p. 109
<i>Table A.4:</i> Complete ghosting measurement data for 125 kVp x-rays. . . . .	p. 109
<i>Table A.5:</i> Complete ghosting measurement data for a 6 MV x-ray beam. . . . .	p. 109

## List of Figures

- Fig. 3.1:* A schematic of a single row of the detection elements in the prototype a-Se AMFPI containing a common scan (or gate) line. . . . . p. 28
- Fig. 3.2:* A schematic of a single pixel in the prototype a-Se AMFPI after Polischuk<sup>5</sup> *et al.*. . . . . p. 30
- Fig. 3.3:* A block diagram of the experimental set-up. . . . . p. 32
- Fig. 3.4:* The density of states (DOS) for the mobility gap of a-Se as adapted from Abkowitz.<sup>14</sup> The valence band mobility edge is located at 0.0 eV and the conduction band mobility edge is located at 2.22 eV. The shallow and deep hole traps are located at 0.26 eV and 0.87 eV from the valence band mobility edge, respectively. The shallow and deep electron traps are located at 0.35 eV and 1.22 eV from the conduction band mobility edge, respectively. . . . . p. 34
- Fig. 3.5:* The experimental set-up used to measure the amount of incident radiation on the detector for kV energies using a pancake ion chamber. . . . . p. 38
- Fig. 3.6:* The dependence of the a-Se AMFPI average pixel signal (background signal subtracted) for 1 to 5 MUs (250 MU/min) of incident radiation for a 6 MV x-ray beam. . . . . p. 41
- Fig. 3.7:* Mean image signal (dark current not subtracted) of central 531 x 531 pixels for one hundred and one (101) consecutive image frames. The frame "0" contains the signal due to an x-ray exposure. . . . . p. 43
- Fig. 3.8:* A zoomed in view of the mean image signal (dark current not subtracted) of central 531 x 531 pixels for a hundred and one (101) consecutive image frames. The frame "0" (whose point is not visible in this figure) contains the signal due to an x-ray exposure. The error for each visible point is within the diamond symbol. . . . . p. 44
- Fig. 3.9:* Lag values as a function of frame number for one experimental run. Lag values for frames  $n=1$  through  $n=15$  are shown. The error for each point is within the diamond symbol. . . . . p. 45
- Fig. 3.10:* A schematic of the lead phantom (top view) where the four shaded areas outside of the hole define the regions from which  $S_{Pb,n}$  was calculated. The shaded area inside of the hole defines the region where  $S_{hole,n}$  was calculated. The area inside of the hole is 81 x 81 pixels; areas 1 and 2 are 531 x 131 pixels; and areas 3 and 4 are 131 x 269 pixels. . . . . p. 52
- Fig. 3.11:* This figure is an example of improper placement of the five areas used to calculate  $S_{hole,n}$  and  $S_{Pb,n}$  shown by the display of: (a) the entire 1024 x 1024 image of the

$n=0$  frame; (b) the central region used to calculate  $S_{\text{hole},n}$  and the surrounding frame-like structure used to calculate  $S_{\text{Pb},n}$  shown to be improperly placed. . . . . p. 53

*Fig. 3.12:* This figure is an example of proper placement of the five areas used to calculate  $S_{\text{hole},n}$  and  $S_{\text{Pb},n}$  shown by the display of: (a) the entire 1024 x 1024 image of the  $n=0$  frame; (b) the central region used to calculate  $S_{\text{hole},n}$  and the surrounding frame-like structure used to calculate  $S_{\text{Pb},n}$  shown to be properly placed. . . . . p. 54

*Fig. 4.1:* Experimental lag values as a function of frame number after exposure for 81 kVp, 42.8  $\mu\text{Gy}$  (exposure time of 3.2 ms), and three frame times. . . . . p. 58

*Fig. 4.2:* Experimental lag values as a function of time after exposure for 81 kVp, 42.8  $\mu\text{Gy}$  (exposure time of 3.2 ms), and three frame times. . . . . p. 59

*Fig. 4.3:* Experimental lag values as a function of time after exposure for 81 kVp, 23.6  $\mu\text{Gy}$  (exposure time of 1.6 ms), and three frame times. . . . . p. 60

*Fig. 4.4:* Experimental lag values as a function of time after exposure for 81 kVp, 77.7  $\mu\text{Gy}$  (exposure time of 6.4 ms), and three frame times. . . . . p. 60

*Fig. 4.5:* Experimental lag values as a function of time after exposure for 81 kVp, 96.0  $\mu\text{Gy}$  (exposure time of 8.0 ms), and three frame times. . . . . p. 61

*Fig. 4.6:* Experimental lag values as a function of time after exposure for 125 kVp, 23.6  $\mu\text{Gy}$  (exposure time of 2.5 ms), and three frame times. . . . . p. 61

*Fig. 4.7:* Experimental lag values as a function of time after exposure for 125 kVp, 42.8  $\mu\text{Gy}$  (exposure time of 2.5 ms), and three frame times. . . . . p. 62

*Fig. 4.8:* Experimental lag values as a function of time after exposure for 125 kVp, 77.7  $\mu\text{Gy}$  (exposure time of 2.5 ms), and three frame times. . . . . p. 62

*Fig. 4.9:* Experimental lag values as a function of time after exposure for 125 kVp, 96.0  $\mu\text{Gy}$  (exposure time of 4.0 ms), and three frame times. . . . . p. 63

*Fig. 4.10:* Experimental lag values as a function of time after exposure for 6 MV, 1MU (250 MU/min), and three frame times. . . . . p. 64

*Fig. 4.11:* Experimental lag values as a function of time after exposure for 6 MV, 2 MU (250 MU/min), and three frame times. . . . . p. 65

*Fig. 4.12:* Experimental lag values as a function of time after exposure for 6 MV, 3 MU (250 MU/min), and three frame times. . . . . p. 65

*Fig. 4.13:* Experimental lag values as a function of time after exposure for 6 MV, 4 MU (250 MU/min), and three frame times. . . . . p. 66

*Fig. 4.14:* Experimental lag values as a function of time after exposure for 125 kVp, 5.2 s/frame, and four air-kerma values (exposure times of 2.5, 2.5, 2.5 and 4.0 ms respectively). . . . . p. 67

*Fig. 4.15:* Experimental lag values as a function of time after exposure for 125 kVp, 7.2 s/frame, and four air-kerma values (exposure times of 2.5, 2.5, 2.5 and 4.0 ms respectively). . . . . p. 68

*Fig. 4.16:* Experimental lag values as a function of time after exposure for 125 kVp, 9.2 s/frame, and four air-kerma values (exposure times of 2.5, 2.5, 2.5 and 4.0 ms respectively). . . . . p. 68

*Fig. 4.17:* Experimental lag values as a function of time after exposure for 81 kVp, 5.2 s/frame, and four air-kerma values (exposure times of 1.6, 3.2, 6.4 and 8.0 ms respectively). . . . . p. 69

*Fig. 4.18:* Experimental lag values as a function of time after exposure for 81 kVp, 7.2 s/frame, and four air-kerma values (exposure times of 1.6, 3.2, 6.4 and 8.0 ms respectively). . . . . p. 69

*Fig. 4.19:* Experimental lag values as a function of time after exposure for 81 kVp, 9.2 s/frame, and four air-kerma values (exposure times of 1.6, 3.2, 6.4 and 8.0 ms respectively). . . . . p. 70

*Fig. 4.20:* Experimental lag values as a function of time after exposure for 6 MV, 5.2 s/frame, and four different amounts of radiation (250 MU/min). . . . . p. 70

*Fig. 4.21:* Experimental lag values as a function of time after exposure for 6 MV, 7.2 s/frame, and four different amounts of radiation (250 MU/min). . . . . p. 71

*Fig. 4.22:* Experimental lag values as a function of time after exposure for 6 MV, 9.2 s/frame, and four different amounts of radiation (250 MU/min). . . . . p. 71

*Fig. 4.23:* Experimental lag values as a function of time after exposure for 9.2 s/frame, 96.0  $\mu$ Gy for 81 (exposure time of 8.0 ms) and 125 kVp (exposure time of 4.0 ms) and irradiation of 4 MU (250 MU/min) for 6 MV photons. . . . . p. 73

*Fig. 4.24:* Experimental lag values as a function of time after exposure for 5.2 s/frame, 96.0  $\mu$ Gy for 81 (exposure time of 8.0 ms) and 125 kVp (exposure time of 4.0 ms) and irradiation of 4 MU (250 MU/min) for 6 MV photons. . . . . p. 73

*Fig. 4.25:* Experimental lag values as a function of time after exposure for 7.2 s/frame, 96.0  $\mu$ Gy for 81 (exposure time of 8.0 ms) and 125 kVp (exposure time of 4.0 ms) and irradiation of 4 MU (250 MU/min) for 6 MV photons. . . . . p. 74

*Fig. 4.26:* Experimental lag values as a function of time after exposure for 5.2 s/frame, 77.7  $\mu\text{Gy}$  for 81 (exposure time of 6.4 ms) and 125 kVp (exposure time of 2.5 ms) and irradiation of 3 MU (250 MU/min) for 6 MV photons. . . . . p. 75

*Fig. 4.27:* Experimental lag values as a function of time after exposure for 7.2 s/frame, 77.7  $\mu\text{Gy}$  for 81 (exposure time of 6.4 ms) and 125 kVp (exposure time of 2.5 ms) and irradiation of 3 MU (250 MU/min) for 6 MV photons. . . . . p. 76

*Fig. 4.28:* Experimental lag values as a function of time after exposure for 9.2 s/frame, 77.7  $\mu\text{Gy}$  for 81 (exposure time of 6.4 ms) and 125 kVp (exposure time of 2.5 ms) and irradiation of 3 MU (250 MU/min) for 6 MV photons. . . . . p. 76

*Fig. 4.29:* Experimental lag values as a function of time after exposure for 5.2 s/frame, 42.8  $\mu\text{Gy}$  for 81 (exposure time of 3.2 ms) and 125 kVp (exposure time of 2.5 ms) and irradiation of 2 MU (250 MU/min) for 6 MV photons. . . . . p. 77

*Fig. 4.30:* Experimental lag values as a function of time after exposure for 7.2 s/frame, 42.8  $\mu\text{Gy}$  for 81 (exposure time of 3.2 ms) and 125 kVp (exposure time of 2.5 ms) and irradiation of 2 MU (250 MU/min) for 6 MV photons. . . . . p. 77

*Fig. 4.31:* Experimental lag values as a function of time after exposure for 9.2 s/frame, 42.8  $\mu\text{Gy}$  for 81 (exposure time of 3.2 ms) and 125 kVp (exposure time of 2.5 ms) and irradiation of 2 MU (250 MU/min) for 6 MV photons. . . . . p. 78

*Fig. 4.32:* Experimental lag values as a function of time after exposure for 5.2 s/frame, 23.6  $\mu\text{Gy}$  for 81 (exposure time of 1.6 ms) and 125 kVp (exposure time of 2.5 ms) and irradiation of 1 MU (250 MU/min) for 6 MV photons. . . . . p. 78

*Fig. 4.33:* Experimental lag values as a function of time after exposure for 7.2 s/frame, 23.6  $\mu\text{Gy}$  for 81 (exposure time of 1.6 ms) and 125 kVp (exposure time of 2.5 ms) and irradiation of 1 MU (250 MU/min) for 6 MV photons. . . . . p. 79

*Fig. 4.34:* Experimental lag values as a function of time after exposure for 9.2 s/frame, 23.6  $\mu\text{Gy}$  for 81 (exposure time of 1.6 ms) and 125 kVp (exposure time of 2.5 ms) and irradiation of 1 MU (250 MU/min) for 6 MV photons. . . . . p. 79

*Fig. 4.35:* Experimental contrast values as a function of frame number after exposure for 6 MV, 3 MU (250 MU/min), and three frame times. . . . . p. 84

*Fig. 4.36:* Experimental contrast values as a function of time after exposure for 6 MV, 3 MU (250 MU/min), and three frame times. . . . . p. 85

*Fig. 4.37:* Experimental contrast values as a function of time after exposure for 125 kVp, an air-kerma of 87  $\mu\text{Gy}$  (exposure time of 3.0 ms), and three frame times. . . . . p. 86

*Fig. 4.38:* Experimental contrast values as a function of time after exposure for 5.2 s/frame, 87  $\mu$ Gy (10 mR, exposure time of 3.0 ms) for 125 kVp and irradiation of 3 MU (250 MU/min) for 6 MV photons. . . . . p. 89

*Fig. 4.39:* Experimental contrast values as a function of time after exposure for 7.2 s/frame, 87  $\mu$ Gy (10 mR, exposure time of 3.0 ms) for 125 kVp and irradiation of 3 MU (250 MU/min) for 6 MV photons. . . . . p. 90

*Fig. 4.40:* Experimental contrast values as a function of time after exposure for 9.2 s/frame, 87  $\mu$ Gy (10 mR, exposure time of 3.0 ms) for 125 kVp and irradiation of 3 MU (250 MU/min) for 6 MV photons. . . . . p. 90

*Fig. 4.41:* Sequence of corrected images of the high contrast phantom ( $I_{norm}$  in Eq. (3.7)) obtained at several time intervals after exposure for 125 kVp, 9.2 s/frame, and 87  $\mu$ Gy (10 mR, exposure time of 3.0 ms). The residual contrast as calculated from Eq. (3.4) is also shown for each image. . . . . p. 92

*Fig. 4.42:* Sequence of corrected images of the high contrast phantom ( $I_{norm}$  in Eq. (3.7)) obtained at several time intervals after exposure for 6 MV, 9.2 s/frame, and 3 MU (250 MU/min). The residual contrast as calculated from Eq. (3.4) is also shown for each image. . . . . p. 93

# **Chapter 1: Introduction**

Imaging is currently a much larger component in radiation therapy for cancer treatment than two decades ago. It plays an important role in treatment planning, verification, modification and execution along with routine quality assurance work. Detectors are the foundation of good imaging. Both the limitations and the potential optimization of imaging detectors must be understood for the continued confident use of imaging in radiation therapy for cancer treatment.

## **1.1 Flat-Panel Detectors**

The most significant recent advance in digital radiography is the development of large area integrated circuits called active-matrix arrays. The modification into flat-panel x-ray imagers was accomplished by coupling phosphors or photo-conductors with the large area active-matrix structure.<sup>1</sup> Each pixel in these active-matrix structures contains either a photo-diode or a charge storage capacitor along with a thin film transistor (TFT) which acts as a switch. Flat-panel imagers have several advantages over the other digital imaging systems. These include: no veiling glare, geometric uniformity, compactness and immunity to stray magnetic fields. The use of digital flat-panel imagers in oncology is a very recent development and numerous aspects of these imagers such as temporal effects, contrast and pixel resolution need yet to be optimized. Digital flat-panel imagers are either indirect or direct conversion detectors.



## 1.2 Indirect and Direct Conversion Active Matrix Flat-Panel Imagers

Currently, there are two types of flat-panel detectors that are being studied for use in digital imaging at kilovoltage (kV) and megavoltage (MV) x-ray photon energies. Specifically the direct conversion flat-panel detectors are only in limited research use. Both types consist of three stages which are: i) the interaction of x-rays with the detector, ii) the storage of information and iii) the readout of information. Flat-panel detectors are x-ray energy fluence detectors, and the received signal is integrated over a finite period of time. Each pixel consists of a switching element and a sensing/storage element.

In the indirect detection approach, a scintillator material (e.g. CsI:Tl, CsI:Na,  $\text{CaWO}_4$  or  $\text{Gd}_2\text{O}_2\text{S:Tb}$ ) is in intimate contact with an active-matrix flat-panel imager (AMFPI) where each pixel of the array contains a photosensitive element (e.g. photodiode) and an analog switch (e.g. a thin film transistor (TFT)). A fraction of the energy deposited by x-rays into the scintillation screen is converted to optical photons. The photosensitive element generates an electrical charge that is proportional to the incident optical energy and is stored until the active-matrix array is read out.<sup>1</sup>

In the direct detection approach, a layer of photoconductor material such as amorphous selenium (a-Se) is in electrical contact with an underlying active-matrix array.<sup>2,3</sup> Other x-ray photoconductors that are currently being researched include  $\text{PbI}_2$ ,<sup>4,5</sup>  $\text{PbO}$ <sup>6</sup> and  $\text{TlBr}$ .<sup>7</sup> X-rays interacting with the photoconductor deposit energy and ionize the photoconductor to produce charges in the form of electron-hole pairs (EHPs). The pixels in an active-matrix contain a conductive electrode with an external electric field to collect the charge. The collected charge is stored in a capacitor and subsequently read by

switching a TFT. Indirect and direct AMFPIs are currently being investigated for use in mammography,<sup>8-12</sup> digital radiography<sup>11,13-19</sup> and portal imaging.<sup>11,20-27</sup>

### **1.3 Thesis Objectives**

The main goal of this thesis is to quantify memory (lag and ghosting due to lag) effects in an amorphous Selenium (a-Se) direct conversion active matrix flat-panel imager (AMFPI). Results are shown as a function of frame time, air-kerma and x-ray photon energy. The presented research plays an important role in the continuing development of image-guided adaptive radiotherapy through the increased understanding of a-Se flat-panel imagers. It is known that lag is a problem in both fluoroscopy<sup>14</sup> and cone-beam CT (CBCT).<sup>11,28</sup> The effect of lag and ghosting artifacts will manifest themselves by the detector appearing to have a “memory”<sup>29</sup> or for real-time applications (30 frames per second) as an effect similar to motion blur.<sup>2,30</sup> It is important to know if these effects increase or decrease with a change in the set-up parameters. This knowledge is potentially useful for better design of a-Se flat-panel detectors and post-processing improvements as the detector is investigated for use in diagnostic radiology, mammography and in electronic portal imaging for radiation therapy. The understanding and quantification of lag and ghosting artifacts is necessary to meet the continually increasing demands of digital projection imaging in oncology and diagnostic radiology.

Chapter 2 reviews the background and progression of digital projection radiography and amorphous Selenium (a-Se) as a photoconductor. Readers who are already familiar with medical imaging and photoconductor technology may wish to go directly to Chapter 3.

Chapter 3 describes the methods and materials that were used for lag measurement and the quantification of ghosting in our laboratory's a-Se active matrix flat-panel imager (AMFPI). Lag and residual contrast (used to quantify the severity of the ghosting due to lag) are defined and the experimental setup is described in detail for the kilovoltage (kV) and megavoltage (MV) experiments. A correction algorithm for variation in pixel sensitivity is also described.

Chapter 4 provides the experimental results and discusses the observed trends and dependencies of lag and ghosting on frame time, amount of incident radiation (air-kerma) and peak x-ray beam energy. Comparison with published results is made for both lag and ghosting.

Chapter 5 closes with final concluding remarks and briefly outlines potential future work. An appendix is included to provide the reader with numerical results and their associated error as most of the results in the body of the thesis are provided in graphical form.

## **1.4 Notes**

[1] J. A. Rowlands and J. Yorkston, "Ch. 4: Flat panel detectors for digital radiography," in *Handbook of Medical Imaging, Volume 1: Physics and Psychophysics*, edited by J. Beutel, H. L. Kundel, and R. L. Van Metter (SPIE Press, Bellingham, 2000), pp. 223-328.

[2] W. Zhao and J. A. Rowlands, "A large area solid-state detector for radiology using amorphous selenium," *Proc. SPIE* **1651**, 134-143 (1992).

- [3] D. L. Lee, L. K. Cheung, and L. S. Jeromin, "A new digital detector for projection radiography," *Proc. SPIE* **2432**, 237-249 (1995).
- [4] K. S. Shah, P. Bennett, M. Klugerman, L. P. Moy, and G. Entine, "Lead iodide films for x-ray imaging," *Proc. SPIE* **3032**, 395-404 (1997).
- [5] K. S. Shah, P. Bennett, L. Cirignano, Y. Dmitriyev, M. Klugerman, K. Mandel, L. P. Moy, and R. A. Street, "Characterization of x-ray imaging properties of PbI<sub>2</sub> films," *Mat. Res. Soc. Symp. Proc.* **487**, 351-360 (1998).
- [6] A. Brauers, N. Conrads, G. Frings, U. Schiebel, M. J. Powell, and C. Glasse, "X-ray sensing properties of a lead oxide photoconductor combined with an amorphous silicon TFT array," *Mat. Res. Soc. Symp. Proc.* **507**, 321-326 (1999).
- [7] D. R. Ouimette, S. Nudelman, and R. Aikens, "A new large area x-ray image sensor," *Proc. SPIE* **3336**, 470-476 (1998).
- [8] B. Polischuk, H. Rougeot, K. Wong, A. Debrie, E. Poliquin, M. Hansroul, J. Martin, T. Truong, M. Choquette, L. Laperrière, and Z. Shukri, "Direct conversion detector for digital mammography," *Proc. SPIE* **3659**, 417-425 (1999).

- [9] M. F. Stone, W. Zhao, B. V. Jacak, P. O'Connor, B. Yu, and P. Rehak, "The x-ray sensitivity of amorphous selenium for mammography," *Med. Phys.* **29** (3), 319-324 (2002).
- [10] W. Zhao, W. G. Ji, A. Debie, and J. A. Rowlands, "Imaging performance of amorphous selenium based flat-panel detectors for digital mammography: Characterization of a small area prototype detector," *Med. Phys.* **30** (2), 254-263 (2003).
- [11] J. H. Siewerdsen and D. A. Jaffray, "A ghost story: Spatio-temporal response characteristics of an indirect-detection flat-panel imager," *Med. Phys.* **26** (8), 1624-1641 (1999).
- [12] S. Vedantham, A. Karellas, S. Suryanarayanan, D. Albagli, S. Han, E. J. Tkaczyk, C. E. Landberg, B. Opsahl-Ong, P. R. Granfors, I. Levis, C. J. D'Orsi, and R. E. Hendrick, "Full breast digital mammography with an amorphous silicon-based flat panel detector: Physical characteristics of a clinical prototype," *Med. Phys.* **27** (3), 558-567 (2000).
- [13] D. L. Lee, L. K. Cheung, B. Rodricks, and G. F. Powell, "Improved imaging performance of a 14 x 17-inch Direct Radiography<sup>TM</sup> System using Se/TFT detector," *Proc. SPIE* **3336**, 14-23 (1998).
- [14] P. R. Granfors, "Performance characteristics of an amorphous silicon flat panel x-ray imaging detector," *Proc. SPIE* **3659**, 480-490 (1999).

- [15] N. Jung, P. L. Alving, F. Busse, N. Conrads, H. M. Meulenbrugge, W. Rütten, U. Schiebel, M. Weibrecht, and H. Wiecezorek, "Dynamic x-ray imaging system based on an amorphous silicon thin-film array," *Proc. SPIE* **3336**, 396-407 (1998).
- [16] T. J. C. Bruijns, P. L. Alving, E. L. Baker, R. Bury, A. R. Cowen, N. Jung, H. A. Luijendijk, H. J. Meulenbrugge, and H. J. Stouten, "Technical and clinical results of an experimental flat dynamic (digital) x-ray image detector (FDXD) system with real-time corrections," *Proc. SPIE* **3336**, 33-44 (1998).
- [17] L. E. Antonuk, Y. El-Mohri, J. H. Siewerdsen, J. Yorkston, W. Huang, V. E. Scarpine, and R. A. Street, "Empirical investigation of the signal performance of a high-resolution, indirect detection, active matrix flat-panel imager (AMFPI) for fluoroscopic and radiographic operation," *Med. Phys.* **24** (1), 51-70 (1997).
- [18] J. H. Siewerdsen, L. E. Antonuk, Y. El-Mohri, J. Yorkston, W. Huang, J. M. Boudry, and I. A. Cunningham, "Empirical and theoretical investigation of the noise performance of indirect detection, active matrix flat-panel imagers (AMFPIs) for diagnostic radiology," *Med. Phys.* **24** (1), 71-89 (1997).
- [19] E. Samei and M. J. Flynn, "An experimental comparison of detector performance for direct and indirect digital radiography systems," *Med. Phys.* **30** (4), 608-622 (2003).

[20] G. Pang, D. L. Lee, and J. A. Rowlands, "Investigation of a direct conversion flat panel imager for portal imaging," *Med. Phys.* **28** (10), 2121-2128 (2001).

[21] M. Lachaine, E. Fourkal, and B. G. Fallone, "Investigation into the physical characteristics of active matrix flat panel imagers for radiotherapy," *Med. Phys.* **28** (8), 1689-1695 (2001).

[22] M. Lachaine, E. Fourkal, and B. G. Fallone, "Detective quantum efficiency of a direct-detection active matrix flat panel imager at megavoltage energies," *Med. Phys.* **28** (7), 1364-1372 (2001).

[23] D. Mah, J. A. Rowlands, and J. A. Rawlinson, "Sensitivity of amorphous selenium to x rays from 40 kVp to 18 MV: Measurements and implications for portal imaging," *Med. Phys.* **25** (4), 444-456 (1998).

[24] M. Lachaine and B. G. Fallone, "Design considerations for direct and indirect active matrix flat-panel portal imagers," *Radiol. Oncol.* **35** (1), 63-71 (2001).

[25] B. M. C. McCurdy, K. Luchka, and S. Pistorius, "Dosimetric investigation and portal dose image prediction using an amorphous silicon electronic portal imaging device," *Med. Phys.* **28** (6), 911-924 (2001).

[26] P. Munro and D. C Bouius, "X-ray quantum limited portal imaging using amorphous silicon flat-panel arrays," *Med. Phys.* **25** (5), 689-702 (1998).

[27] P. B. Greer and C. C. Popescu, "Dosimetric properties of an amorphous silicon electronic portal imaging device for verification of dynamic intensity modulated radiation therapy," *Med. Phys.* **30** (7), 1618-1627 (2003).

[28] J. H. Siewerdsen and D. A. Jaffray, "Cone-beam computed tomography with a flat-panel imager: Effects of image lag," *Med. Phys.* **26** (12), 2635-2647 (1999).

[29] W. Zhao, G. DeCrescenzo, and J. A. Rowlands, "Investigation of lag and ghosting in amorphous selenium flat-panel x-ray detectors," *Proc. SPIE* **4682**, 9-20 (2002).

[30] W. Zhao and J. A. Rowlands, "X-ray imaging using amorphous selenium: Feasibility of a flat panel self-scanned detector for digital radiology," *Med. Phys.* **22** (10), 1595-1604 (1995).



## Chapter 2: Background

Medical imaging plays a central role in North American health care. Procedures such as x-ray radiographic imaging, magnetic resonance imaging (MRI), x-ray computed tomography (CT) imaging, ultrasound (US) imaging, image based bone density measurements and mammograms are performed routinely in the clinics. The information gathered in these diagnostic procedures is subsequently used for disease screening, diagnosis, therapy planing and palliative care.

### 2.1 Digital Projection Radiography

Film/screen x-ray imaging was the dominant form of penetration-based imaging for almost eighty (80) years since the discovery of the x-ray by Röntgen in 1895. In film/screen x-ray imaging, a cone beam of x-rays penetrates through the patient. The 2-D transmitted x-ray intensity distribution is measured by film/screen, therefore, a film image contains the information regarding patient anatomy. It is only since the 1970s that computed tomography (CT), magnetic resonance imaging (MRI), digital subtraction angiography (DSA), Doppler ultrasound (US), positron emission tomography (PET) and single photon emission computed tomography (SPECT) have been developed and implemented into the clinic.<sup>1</sup>

As understanding of basic imaging theory increased during the 1950s, attempts were made to digitize part of the imaging process. "Digital radiography" is currently the generic term that is applied to all projection-based radiographic (i.e. does not include CT, MRI, PET, SPECT, US *et cetera*) imaging systems where the end product is a digitized image. A digital image is sampled in spatial domain (i.e. pixels) and quantized in image

intensity (i.e. gray level). The definitive beginning of digital imaging came in the 1980s with the availability of commercial computed radiography (CR) systems.<sup>2</sup> The development of digital imaging was made feasible by inexpensive computational resources (i.e. increased central processing unit (CPU) speed, random access memory (RAM) and large hard drive storage capacity) and the increasing infrastructure of the computer age (i.e. high-resolution cathode ray tube (CRT) screens, ethernet capabilities, internet accessibility and in-house network systems). Bright, high-resolution CRT screens along with the compression, archiving and transmission of digital images also greatly assisted with the pragmatic, everyday concerns necessary for the realistic implementation of digital imaging within clinical medicine.<sup>2</sup>

It is not true that all processes within a digital imaging system are inherently digital. The initial stages of all digital detectors actually involve analog signals. The process of an x-ray photon being converted into visible light photons or electronic charge results in the production of an analog signal. Even in a pixelated detector, the signal produced within each pixel is still an analog signal. It is only once an analog signal passes through an analog to digital converter (ADC) that the term "digital" can be truly applied. The significant feature of digital radiography is that the end product is a digital image with a predetermined pixel resolution. The advantages of digital radiography come from this end product of a digital image.<sup>3</sup>

Some of the advantages of digital x-ray images as listed by Rowlands and Yorkston<sup>4</sup> include less detector handling than with film, immediate imaging viewing, more convenient storage and computer-aided diagnosis.<sup>5,6</sup> These factors facilitate more convenient patient management. Other advantages include reduced operational costs

compared to film/screen radiography, reduced waste (film is a single-use type of detector) and post-processing options<sup>3</sup> to improve image quality and optimize diagnostic information. Some disadvantages of digital x-ray images include artifacts (due to lag, ghosting, sensitivity reduction and long-term memory effects) and large start-up costs. The large field of view and high pixel resolution required in clinical applications are only available very recently. The large digital images (high-resolution digital chest radiographs range from 4 MB to 32 MB) require a large amount of storage space, high network bandwidth in a picture archiving and communications system (PACS) and costly high-luminance and high-resolution CRT screens for the purpose of displaying the images with sufficient pixel resolution for medical diagnosis.<sup>3</sup> Another disadvantage of digital imaging is the loss of information by the very definition of a digital image. Intensity values and pixels are both discrete resulting in the loss of intermediate intensity information and sub-pixel spatial variations.<sup>7</sup> The significance of this loss of information resolution will depend on the application, the image bit-depth and the size of the pixels.

Numerous digital imaging systems have been developed and implemented into the clinic since the 1950s. Computed radiography (CR) makes use of a photo-stimulable phosphor (PSP) or storage phosphor detector. Most of the absorbed energy from the incident x-rays is trapped in the PSP screen that is subsequently read out by stimulating the emission of the trapped energy using a laser light. The visible light released from the imaging plate is collected by a fiber optic light guide, converted into electrical signal using a photomultiplier tube (PMT) and subsequently digitized and stored.<sup>3</sup>

Image intensifier digital radiography systems are another example of the transition from analog to digital end products. This digital system is a basic image

intensifier based fluoroscopy system. A video camera or a charge-coupled device (CCD) is used to digitize the analog optical image from the image intensifier screen. This digitization of the video signal makes possible instant radiography and ciné imaging for improved diagnostic potential. CCDs use an integrated circuit made of crystalline silicon to form images from visible light. The incident visible light liberates electrons within the photosensitive crystalline silicon which are read out as an electronic signal in a digital form. The two-dimensional (2-D) pixelated CCD chip produces an image by moving the charge packets down the pixel columns to be read out row by row. The charge packets formed correspond to the intensity of the visible light incident on each pixel.<sup>3</sup>

Photoconductors have also been used in medical imaging where x-rays interact within the photoconductive material and produce a latent charge image.<sup>4</sup> Many different methods have been developed to read the latent charge image. For mammography, Boag<sup>8</sup> successfully used fine toner particles to produce an image for diagnostic purposes. The latent image has also been read out using a layer of liquid crystal in close proximity with the photoconductor,<sup>9</sup> a scanning electron beam,<sup>10</sup> and scanned luminescent toner radiography.<sup>11</sup> An electrostatic probe (multi-probe based systems have also been developed) placed close enough to the amorphous selenium (a-Se) photoconductive layer will couple to the latent charge image capacitively and the image can subsequently be scanned and digitized.<sup>12,13</sup>

The most significant recent advance in digital radiography is the development of large area integrated circuits called active-matrix arrays. The realization of this important technology allows for the deposition of semiconductors (specifically hydrogenated amorphous silicon (a-Si:H)) on large areas in a well-controlled fashion. The resulting

structure's physical and electrical properties can be modified and adapted for specific applications. This technology was originally developed for laptop-computer displays and was termed as active-matrix liquid-crystal flat-panel display (AMLCD). The modification into flat-panel x-ray imagers was accomplished by coupling phosphors or photo-conductors with the large area active-matrix structure.<sup>4</sup> Each pixel in these active-matrix structures contains either a photo-diode or a charge storage capacitor along with a thin film transistor (TFT) which provides the switching mechanism in the readout stage of the flat-panel image. These flat-panel systems are generally self-scanned. They have several advantages over the other digital imaging systems. These include: no veiling glare, geometric uniformity, compactness and immunity to stray magnetic fields. Some of these properties allow flat-panels to be used in MRI suits.<sup>7</sup>

Digital imaging in oncology is currently used for the purposes of screening programs, disease diagnosis, qualification and quantification of the spread of disease, initial setup of radiation therapy treatment plans, the delivery, monitoring and modifying of radiation therapy treatment, and the analysis and observation of disease remission and recurrence. Digital flat-panel imagers used in oncology are either indirect or direct conversion detectors. The use of digital flat-panel imagers in oncology is a very recent development and numerous aspects of these imagers such as temporal effects, contrast and pixel resolution need yet to be optimized. Direct conversion detectors often use amorphous Selenium (a-Se) as the photoconductor which directly converts incident x-ray photons into electric charge (electron-hole pairs (EHPs)). Section 2.2 discusses the particulars of the photoconductor a-Se.

## 2.2 Amorphous Selenium as a Photoconductor

### 2.2.1 The Element Selenium

Selenium was discovered by Jöns Berzelius in the year 1817 in Stockholm, Sweden. Selenium exhibits both photovoltaic (converts light to electricity) and photoconductive (electrical resistance decreases with increased illumination) properties. It can also convert alternating current (ac) electricity to direct current (dc) electricity.<sup>14</sup>

"Historically it [photoconductivity] was first reported by Willoughby Smith, an electrician for a telegraph company. By one of those curious coincidences, his observation was made in the element selenium which would prove so important in the development of xerography. Smith using rods of selenium as resistors in the testing of submarine cables, found that their resistance changed depending on whether they were enclosed in a light-tight box or exposed to a light source."<sup>15</sup>

Selenium (Se) has an atomic number of 34, an atomic mass of 78.96, a melting point of 490 K, a boiling point of 958.1 K and its density is  $4.79 \text{ gcm}^{-3}$  at 293 K.<sup>14</sup> A-Se has a density of  $4.27 \text{ gcm}^{-3}$ .<sup>16</sup> One of the advantages of using *amorphous* Se is it is entirely free of granularity resulting in very uniform imaging properties to a very fine scale.<sup>4</sup> It should be thought about more as a molecular solid than a crystal.<sup>8</sup>

### 2.2.2 Properties of Amorphous Selenium

In the diagnostic photon energy range, both photoelectric and Compton interactions in the a-Se layer contribute to the absorbed energy. Via the photoelectric effect, an absorbed x-ray photon in the a-Se will produce a photoelectron with kinetic

energy equal to the difference between the incident photon energy and the binding energy of the electron. The atom is left in an excited state and emits characteristic radiation (fluorescent x-rays) and Auger electrons as it returns to the ground state. Depending on the thickness of the a-Se layer, the photoelectron will either deposit its energy within the a-Se creating EHPs or escape the a-Se. The generally accepted view is that an optical photon will create one EHP and an x-ray photon will create thousands of EHPs through electron cascade.<sup>17</sup>

Energy is also deposited within the a-Se bulk via the Compton effect. An incident photon collides with an electron such that the photon is scattered and the recoil electron acquires kinetic energy and momentum. The scattering angle between the recoil electron and the scattered photon depends on the energy of the incident photon. The recoil electron will subsequently either deposit its energy within the a-Se creating EHPs or escape the a-Se.<sup>18</sup>

Photoconductors contain a conduction band, a valence band and the band gap region between these two bands which determines the minimum energy required to excite an electron from the valence band into the conduction band. A-Se has a band gap energy ( $E_g$ ) of about 2.3 eV.<sup>19</sup> Obviously, only photons with energy greater than 2.3 eV will have the potential to produce EHPs in the a-Se photoconductor. A certain amount of energy is needed to create an EHP in the a-Se layer denoted by  $W_0$  (the average energy) which is always larger than  $E_g$ . A minimum of three formulas have been proposed to describe the creation energy of EHPs in semiconductors. Klein's<sup>20</sup> semi-empirical formula is given by

$$W_0 = 2.8E_g + E_{phonon} \quad (2.1)$$

where the second term is a phonon energy term which ranges between 0.5 and 1 eV. The second formula is specific for amorphous semiconductors where the momentum of the interacting particles does not need to be conserved and is given by

$$W_0 = 2.2E_g + E_{phonon} \quad (2.2)$$

where the second term is again a phonon energy term which ranges between 0.5 and 1 eV.<sup>17</sup> The third formula is from Montrimas<sup>21</sup> *et al.* and is shown in Eq. (2.3).

$$W_0 = 2.67E_g + 0.86 \quad (2.3)$$

Using a value of 0.75 eV for the phonon energy term, the three formulas give values for  $W_0$  of 7.19, 5.81 and 7.001 eV respectively. The reason that  $W_0 > E_g$  is because  $W_0$  takes into account the effective masses of the particles (incident electron, excited electron and resulting hole) and the conservation of momentum (Eq. (2.2) being the exception) and kinetic energy. It is desirable for the photoconductor to have a low  $W_0$  in order for many EHPs to be created with few incident photons. What is actually measured is the average energy required to collect a detectable pair ( $W_{\pm}$ ), related to  $W_0$  by

$$W_{\pm} = \frac{W_0}{\eta} \quad (2.4)$$

where  $\eta$  is the escape efficiency (i.e. the fraction of EHPs which escape recombination).

Lachaine and Fallon<sup>22</sup> have demonstrated that  $W_{\pm}$  decreases with increasing x-ray energy. This stems from reduced recombination at higher energy. They illustrate that recombination occurs between geminate pairs (both the electron and the hole come from the same original pair), columnar pairs (both the electron and the hole come from the same ionization track but not from the same original pair) and also between other pairs



created within the photoconductive material. Thus recombination is both an intra-track and an inter-track process. It has also been shown that a larger percentage of charges escape recombination with an increase in incident photon energy.<sup>23</sup> The reason is that the distance between created EHPs increases with increasing x-ray energy resulting in less chance of recombination which is seen as a lower value of  $W_{\pm}$  since  $\eta$ , the escape efficiency would increase.<sup>22</sup>

Recombination must also be addressed when looking at the trapping and detection of electrons and holes. The effect of an applied electric field is to increase the fraction of escaping charges to the respective electrodes. Onsager states that this fraction is increased

“by a factor which in the incipient stage of the effect is proportional to the field intensity and independent of the initial distance, although it depends on the orientation of an ion pair.”<sup>24</sup>

He also claims that the increase of the ionization current is approximately 1 % for every 100 Vcm<sup>-1</sup>. Another positive effect of increasing the electric potential across the a-Se is that the lateral spread of the electric charges is decreased resulting in a sharper final image. The electric charges traverse the a-Se layer more quickly and have less time to diffuse due to Coulombic effects.<sup>4</sup> Lateral spread of the electric charges within the a-Se must also be guarded against at the a-Se surface. This is accomplished by the introduction of a high density of traps near the surface of the a-Se.<sup>4</sup>

Conducting electrodes are placed on both surfaces of the photoconductive layer to collect the charge created within the a-Se. The electrodes must collect this charge as well as prevent charges from within themselves traversing into the a-Se layer. This is called a

blocking contact.<sup>4</sup> Pure a-Se is alloyed with about 0.5 % arsenic (As). This prevents the crystallization of the a-Se which takes place over a time period of a few months to a few years with pure a-Se. The As alloy, however, introduces a substantial number of hole traps which is reduced by the additional doping of 10 to 20 parts per million (ppm) of chlorine (Cl). The resulting material is referred to as stabilized a-Se which has favorable hole and electron transport properties.<sup>4</sup>

In an imaging experiment, the EHPs contain the information about the incident energy fluence. Therefore, the electric charges must traverse the photoconductor without being trapped. The Schubweg ( $S_h$  for holes and  $S_e$  for electrons) is the mean distance traversed by a charge carrier before it is trapped and is defined in Eq. (2.5) where  $\mu$  is the drift mobility,  $\tau$  is the carrier lifetime and  $E$  is the applied field.

$$S = \mu\tau E \quad (2.5)$$

Electron mobility in a-Se is variable ( $\mu_e=0.003-0.006 \text{ cm}^2\text{V}^{-1}\text{s}^{-1}$ ) and hole drift mobility is quite reproducible ( $\mu_h=0.13 \text{ cm}^2\text{V}^{-1}\text{s}^{-1}$ ). To achieve good imaging, it is critical that the Schubwegs ( $S_h$  and  $S_e$ ) are much longer than the thickness of the a-Se layer.<sup>4</sup>

### 2.2.3 A Brief Historical Review

The first use of photoconductors or photo-emissive materials (defined by Carlson<sup>25</sup> as materials which emit electrons when exposed to radiation such as light, ultra-violet x-rays, x-rays or the like) was contemplated and an invention designed intending to improve the photographic process. In 1938, Carlson described electron photography based on this invention.<sup>25</sup> In the same patent, he also suggested that a powder, influenced by the charge pattern, can be used to render the latent electrostatic

image visible. The use of selenium as a photoconductive insulating material is first mentioned in Carlson's 1939 U. S. Patent entitled "Electrophotography" where a melted mixture of predominately sulfur and selenium is listed as a suitable material.<sup>26</sup> Schaffert *et al.* also mention the use of selenium, and mixtures of selenium and sulfur as satisfactory semi-conductive coating materials to be used in the development of the plates for electroradiography.<sup>27</sup> Amorphous or vitreous selenium was first mentioned for use as a photoconductive insulating layer in Carlson's 1955 U. S. Patent.<sup>28</sup>

Xeroradiography or electroradiography as it was initially termed was disclosed by Schaffert *et al.* and defined as,

“an electrical method for preparing radiographic images produced by penetrating radiation.”<sup>27</sup>

"Xeroradiography derives its name from *xeros* (Greek for dry), *radius* (Latin for ray), and *graphein* (Greek for writing)."<sup>29</sup>

This method of x-ray imaging is in contrast to the “wet chemistry” of the film/screen method. The first step in xeroradiography, assuming that a photoconductive plate is available (e.g. an a-Se layer evaporated onto a metal substrate), is to place a uniform surface charge onto the a-Se plate. This is accomplished by corona charging. When the charged plate is inside a light tight box or cassette, penetrating radiation incident on an object and subsequently on the plate produces a latent electrostatic image of the object. This latent image is formed as a result of incident x-rays on the plate producing electric charges within the photoconductive layer which would partly dissipate the initial uniform surface charge.<sup>8</sup>

This latent image can be rendered visible by a number of methods including the powder development and the surface electrostatic probe methods. The powder development method was discovered and developed first. This was used initially by Carlson<sup>25,26,28</sup> and Schaffert<sup>27</sup> *et al.* and further developed by Jeromin.<sup>30</sup> As the technology surrounding xeroradiography progressed, it was realized that the limiting factor was the inefficiency of this toner readout method. The size of the toner particles limited the spatial resolution of the final rendered image to less than the inherent resolution of the latent image on the surface of the a-Se plate.<sup>31</sup>

The surface electrostatic probe method uses a non-contact probe along with an electrostatic voltmeter (ESVM).<sup>32</sup> The probe utilizes an oscillating piezoelectric crystal which is connected to an internal vibrating capacitor. This vibrating crystal produces an alternating current (ac) signal where the amplitude is dependent on the strength of the electric field it is subject to. The ESVM detects the peak amplitude and the resulting signal is subsequently digitized by an analog to digital converter (ADC).<sup>32</sup>

Presently, a-Se detectors are almost exclusively based on flat-panel technology. The flat-panel detector used by our laboratory to perform our research is described in detail in Section 3.1.

## 2.3 Notes

[1] J. Beutel, J. M. Fitzpatrick, S. C. Horii, Y. Kim, H. L. Kundel, M. Sonka, and R. L. Van Metter, "Preface," in *Handbook of Medical Imaging, Volume 1: Physics and Psychophysics*, edited by J. Beutel, H. L. Kundel, and R. L. Van Metter (SPIE Press, Bellingham, 2000), pp. xi-xii.

[2] J. Beutel and R. L. Van Metter, "Introduction to Part I," in *Handbook of Medical Imaging, Volume 1: Physics and Psychophysics*, edited by J. Beutel, H. L. Kundel, and R. L. Van Metter (SPIE Press, Bellingham, 2000), pp. xv-xvi.

[3] J. T. Bushberg, J. A. Seibert, E. M. Leidholdt, Jr., and J. M. Boone, *The Essential Physics of Medical Imaging*, Second ed. (Lippincott Williams & Wilkins, Philadelphia, 2002).

[4] J. A. Rowlands and J. Yorkston, "Ch. 4: Flat panel detectors for digital radiography," in *Handbook of Medical Imaging, Volume 1: Physics and Psychophysics*, edited by J. Beutel, H. L. Kundel, and R. L. Van Metter (SPIE Press, Bellingham, 2000), pp. 223-328.

[5] H. P. Chan, K. Doi, S. Galhotra, C. J. Vyborny, H. MacMahon, and P. M. Jokich, "Image feature analysis and computer-aided diagnosis in digital radiography. I. Automated detection of microcalcifications in mammography," *Med Phys* **14** (4), 538-548 (1987).

[6] M. L. Giger, N. Ahn, K. Doi, H. MacMahon, and C. E. Metz, "Computerized detection of pulmonary nodules in digital chest images: Use of morphological filters in reducing false-positive detections," *Med Phys* **17** (5), 861-865 (1990).

- [7] M. J. Yaffe and J. A. Rowlands, "X-ray detectors for digital radiography," *Phys. Med. Biol.* **42** (1), 1-39 (1997).
- [8] J. W. Boag, "Xeroradiography," *Phys. Med. Biol.* **18** (1), 3-37 (1973).
- [9] P. K. Rieppo and J. A. Rowlands, "X-ray imaging with amorphous selenium: Theoretical feasibility of the liquid crystal light valve for radiography," *Med Phys* **24** (8), 1279-1291 (1997).
- [10] R. Luhta and J. A. Rowlands, "Feasibility of a large area x-ray sensitive vidicon for medical fluoroscopy: Resolution and lag factors," *Med Phys* **24** (5), 621-631 (1997).
- [11] J. W. May and A. R. Lubinsky, "High-resolution computed radiography by scanned luminescent toner xeroradiography," *Proc. SPIE* **1896**, 296-312 (1993).
- [12] L. S. Jeromin and L. M. Klynn, "Electronic recording of x-ray images," *J. Appl. Photo. Engin.* **5**, 183-189 (1979).
- [13] U. Neitzel, I. Maack, and S. Gunther-Kohfahl, "Image quality of a digital chest radiography system based on a selenium detector," *Med Phys* **21** (4), 509-516 (1994).
- [14] [http://www.chemsoc.org/viselements/pages/data/selenium\\_data.html](http://www.chemsoc.org/viselements/pages/data/selenium_data.html).

- [15] J. Mort, *The Anatomy of Xerography* (McFarland & Company, Jefferson, 1989).
- [16] R. M. Schaffert, *Electrophotography*, Second ed. (Focal Press Limited, London, 1975).
- [17] W. Que and J. A. Rowlands, "X-ray photogeneration in amorphous selenium: Geminate versus columnar recombination," *Phys. Rev. B* **51** (16), 10500-10507 (1995).
- [18] H. E. Johns and J. R. Cunningham, *The Physics of Radiology*, Fourth ed. (Charles C Thomas, Springfield, 1983).
- [19] M. Lachaine and B. G. Fallone, "Calculation of inelastic cross-sections for the interaction of electrons with amorphous selenium," *J. Phys. D: Appl. Phys.* **33**, 551-555 (2000).
- [20] C. A. Klein, "Band gap dependence and related features of radiation ionization energies in semiconductors," *J. Appl. Phys.* **39**, 2029-2038 (1968).
- [21] E. A. Montrimas, B. K. Rakauskene, and J. Rakauskas, "Investigation of quantum efficiency of selenium electroradiographic layers," *Lietuv. Fiz. Rink.* **10**, 941 (1970).
- [22] M. Lachaine and B. G. Fallone, "Monte Carlo simulations of x-ray induced recombination in amorphous selenium," *J. Phys. D: Appl. Phys.* **33**, 1417-1423 (2000).

- [23] D. Mah, J. A. Rowlands, and J. A. Rawlinson, "Sensitivity of amorphous selenium to x rays from 40 kVp to 18 MV: Measurements and implications for portal imaging," *Med. Phys.* **25** (4), 444-456 (1998).
- [24] L. Onsager, "Initial recombination of ions," *Phys. Rev.* **54**, 554-557 (1938).
- [25] C. F. Carlson, "Electron photography," U.S. Patent 2221776 (1938).
- [26] C. F. Carlson, "Electrophotography," U.S. Patent 2297691 (1939).
- [27] R. M. Schaffert, R. C. McMaster, and W. E. Bixby, "Electroradiography," U.S. Patent 2666144 (1950).
- [28] C. F. Carlson, "Process for developing an electrostatic image," U.S. Patent 2842456 (1955).
- [29] P. P. Fatouros and G. U. V. Rao, "Ch. 19: Xeroradiography and electron radiography," in *The Physical Basis of Medical Imaging*, edited by C. M. Coulam, J. J. Erickson, F. D. Rollo, and A. E. James, Jr. (Appleton-Century-Crofts, New York, 1981), pp. 265-277.
- [30] L. S. Jeromin and H. L. Hoyt, III, "Development apparatus for latent electrostatic images," U.S. Patent 3640246 (1969).



[31] W. Que and J. A. Rowlands, "X-ray imaging using amorphous selenium: Inherent spatial resolution," *Med Phys* **22** (4), 365-374 (1995).

[32] T. Falco, H. Wang, and B. G. Fallone, "Preliminary study of a metal/a-Se-based portal detector," *Med Phys* **25** (6), 814-823 (1998).

## **Chapter 3: Methods and Materials**

This chapter describes the methods used to quantify lag and ghosting due to lag for the purpose of better understanding the temporal response of stabilized a-Se to kilovoltage (kV) and megavoltage (MV) x-rays. The direct detection detector used for all of our experiments is explained for both operational and descriptive qualities in Section 3.1. The strict definitions of lag and contrast (used to quantify ghosting) are given in Sections 3.2.1 and 3.2.2, respectively. The experimental procedures and processes are described for lag and ghosting due to lag in Sections 3.3 and 3.4, respectively. Post processing corrections for pixel to pixel sensitivity variation are explained in Section 3.5.

### **3.1 Amorphous Selenium Active Matrix Flat-Panel Imager**

The a-Se detector is an AMFPI (IMAM Detector, ANRAD Corporation, Pointe Claire, Quebec, Canada) where 200  $\mu\text{m}$  (Fig. 3.1) of a-Se is vacuum deposited directly onto a 2-D hydrogenated amorphous silicon (a-Si:H) array in which each element contains a storage capacitor and a TFT. A potential of 1000 volts is typically applied across the a-Se giving an electric field of 5  $\text{V}/\mu\text{m}$ . A 450 nm thick coplanar bias electrode has been evaporated on top of the a-Se layer which allows an electric field of up to 15  $\text{V}/\mu\text{m}$ . A 40  $\mu\text{m}$  thick polymer has been placed above the bias electrode for electrical insulation.

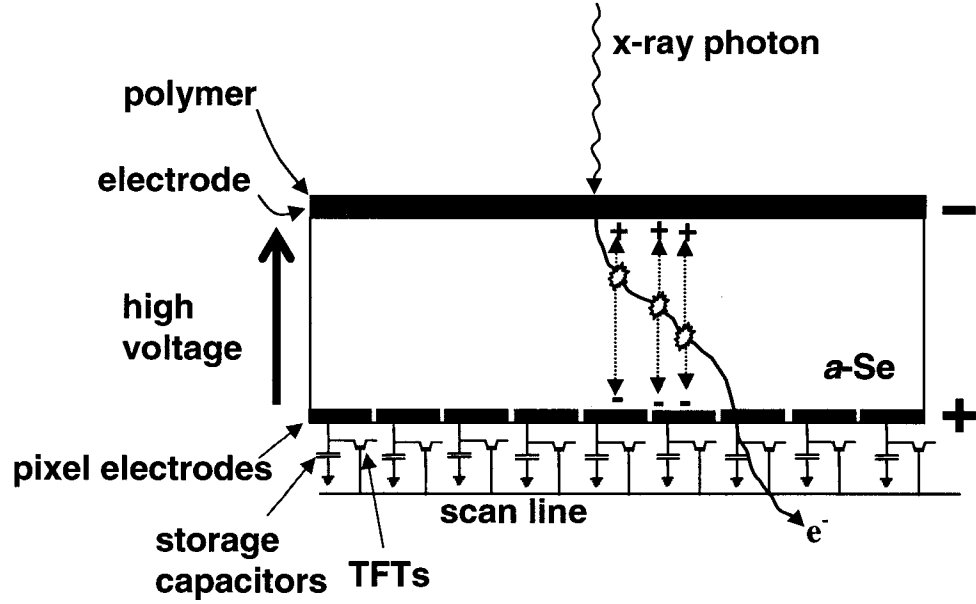


Fig. 3.1: A schematic of a single row of the detection elements in the prototype a-Se AMFPI containing a common scan (or gate) line.

The active-matrix array has an active area of  $8.7 \times 8.7 \text{ cm}^2$  with an  $85 \times 85 \mu\text{m}^2$  pixel pitch ( $T_x$ ,  $8.7 \text{ cm} \div 1024$ ). It has a  $75 \times 75 \mu\text{m}^2$  pixel size<sup>1</sup> ( $\tau_x$ ) resulting in a 78 % geometric fill factor ( $f_g$ ). Its effective pixel size ( $\epsilon_x$ ) has been estimated to be  $79 \times 79 \mu\text{m}^2$  (for an absorption fraction of 1) resulting in an effective fill factor ( $f_e$ ) of 87 %.<sup>2</sup> The geometric fill factor  $f_g$ , is defined in Eq. (3.1) as the fraction of the pixel pitch area covered by the pixel electrode ( $\tau_x \tau_y$ ).<sup>3</sup> The physical area of a pixel (the dimension of which is referred to as the pixel pitch for square pixels) is represented by  $T_x T_y$ .

$$f_g = \left( \frac{\tau_x \tau_y}{T_x T_y} \right) \cdot 100 \quad (3.1)$$

The effective fill factor  $f_e$ , is defined as the percentage of the charges reaching the active matrix that are collected by pixel electrodes.<sup>3</sup> For direct conversion systems,  $f_e$  is the

quotient of the zero frequency detective quantum efficiency (DQE(0)) divided by the absorption fraction.<sup>2</sup> The DQE(0) is a measure of the percentage of incoming x-ray photons that are detected.<sup>2</sup> The effective fill factor  $f_e$ , is mathematically described in Eq. (3.2),

$$f_e = \left( \frac{\epsilon_x \epsilon_y}{T_x T_y} \right) \cdot 100 \quad (3.2)$$

where  $(\epsilon_x \epsilon_y)$  and  $(T_x T_y)$  are the effective pixel area and the physical pixel area, respectively. As explained below,  $f_e$  is greater than  $f_g$  because of the electrostatic nature of this detector. The electrical charge which falls in the gaps (passivation layers) between the pixel electrodes redirects (because similar charges repel each other) subsequent similar image charge back towards the collection electrode of the pixel.<sup>2</sup> As a result, image charge is collected from an area that effectively appears and acts larger than the physical area of the pixel electrode resulting in  $f_e > f_g$ .

Each pixel is made up of a common (top) bias electrode, a pixel (collector) electrode, a 0.68 pF storage capacitor and a TFT that is switched to read the charge off the capacitor. A schematic of a single row of the detector pixels that share a common gate signal is shown in Fig. 3.1. The 2-D TFT array contains 1024 x 1024 elements. A Cu plate is used in the megavoltage (MV) experiments for build-up, as well as, reducing the amount of low energy scattered radiation reaching the detector.<sup>4</sup> Figure 3.2 illustrates the equivalent electronic schematic of a single pixel in the active-matrix, modified from Polischuk<sup>5</sup> *et al.* The a-Se layer is represented by “C<sub>se</sub>” where the top electrode is negatively biased (illustrated by the “-“ and “+” symbols). The current through the a-Se bulk is symbolized by “I<sub>se</sub>”, it flows in the direction of the arrow shown in the figure.

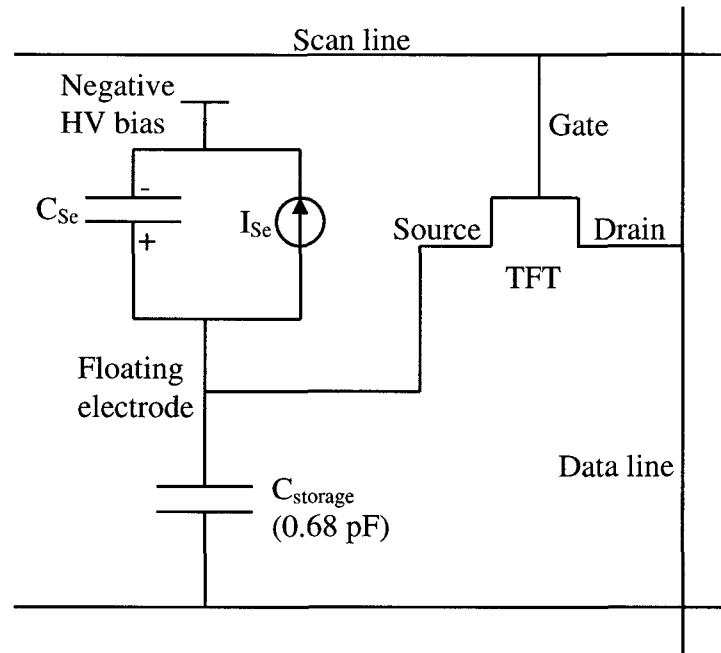


Fig. 3.2: A schematic of a single pixel in the prototype a-Se AMFPI after Polischuk<sup>5</sup> *et al.*

The top electrode of the detector is negatively biased resulting in the collection of the electrons at the pixel electrodes as opposed to the holes.<sup>5</sup> The storage capacitor ( $C_{\text{storage}}$ ) thus becomes increasingly negative during irradiation. When the detector is not being irradiated by x-rays, the scan lines are negatively biased so that the TFTs are in their non-conducting state. When the detector is irradiated with a large x-ray dose the storage capacitor becomes increasingly negative. This negative charge collected on the capacitor will cause the source electrode of the TFT to float negative as well. When a sufficiently large dose of x-rays is incident on the detector, the electrical potential between the gate and the source will become positive (i.e. the negative charge on the source will become larger than the negative bias of the gate) resulting in leakage current across the TFT. This leakage current is drained out by the data lines.

When the TFTs are actually switched on to read the charge on the capacitors (positive potential to the gate of the TFT), the storage capacitor is automatically discharged as the stored charges flow through the data lines to the inverted input of the preamplifiers. The collecting electrode of each pixel in the scanned row is also brought to ground potential. This sequence is repeated for each gate line to read the 2-D image. Multi-channel amplifiers and scan driver circuits are used to read out the collected charge. There is an electronic noise floor of nearly 1600 electrons with a load capacitance of 100 pF.<sup>2</sup> The amplifier gains can be set to various values for variable incident energy fluence. For diagnostic and MV energies, the gains were set at  $10.4 \times 10^{-4}$  and  $2.08 \times 10^{-4}$  counts/electron, respectively. The lower gain for the MV energy was selected to avoid exceeding the ADC's dynamic range.

We summarize the data flow in the a-Se direct-conversion system (Fig. 3.3). Incident x-ray irradiation produces electron-hole pairs (EHPs) in the a-Se bulk. The electrons are collected by pixel electrodes and integrated onto storage capacitors (0.68 pF each). The image is read out one scan line at a time by applying a positive potential to the scan line which is to be read out. This switches the TFTs to a conducting state and the charge accumulated on the storage capacitors is transferred onto the data lines (this occurs for all 1024 pixels located on the one scan line being read) where pre-amplifiers located at the end of the data lines are charged. Multi-channel amplifiers and scan driver circuits are used in the process of reading out the collected charge which is then digitized by a 13-bit ADC. The digitized raw image data is then transferred from the a-Se detector cassette to an interface module and subsequently to a processor board (Matrox Genesis, Matrox Electronic Systems Ltd.) via a high-speed serial link (Fig. 3.3). The image data

can then be saved onto the computer hard drive from the twenty-three (23) image buffers of the processor board.<sup>4</sup>

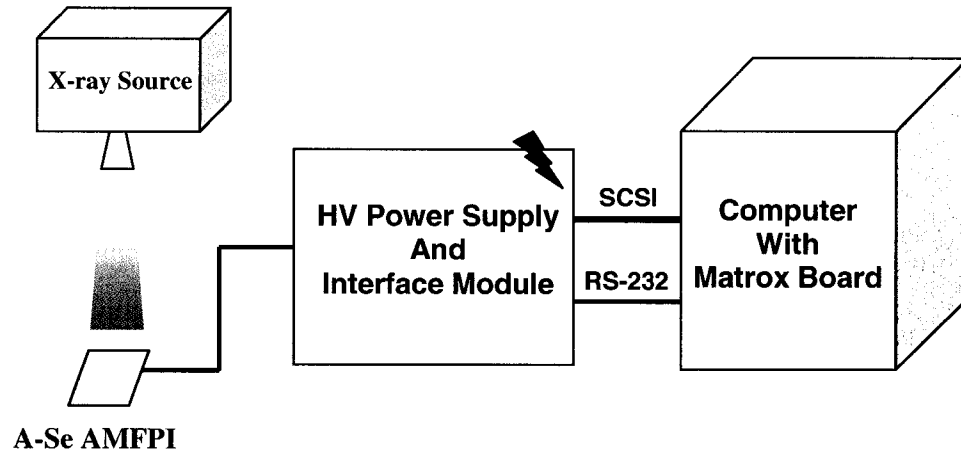


*Fig. 3.3:* A block diagram of the experimental set-up.

The AMFPI is operated by command files (or command line) on the computer. These commands are transferred from the computer to the interface module (IM) via a RS-232 communication control link. The IM communicates with the AMFPI cassette through four cable connections. Inside the IM there is also located the high voltage (HV) power supply. The HV is connected to the cassette by a shielded cable capable of handling up to 3000 V. Any data transferred between the cassette and the IM is through a shielded 50 wire (30 AWG) cable with thirty-four stranded conductors. The remaining two connections are high-speed coaxial cables which are connected to the transmitter in the cassette. Data is transferred from the IM to the computer via a SCSI (RS-422) parallel data link cable connection.

### 3.2 Lag and Ghosting in Diagnostic and Megavoltage Imaging

Both indirect and direct AMFPIs suffer from "memory effects" which refer to any signal remaining from previous x-ray exposures.<sup>6-13</sup> The fundamental cause for these "memory effects" in direct AMFPIs is the trapping of electrons and holes in shallow and deep traps and their subsequent release. It is the density of states (DOS) for the mobility gap that opens the door to a better understanding of these shallow and deep traps. Figure 3.4 is a diagram of the DOS for a-Se, modified from Abkowitz.<sup>14</sup> The valence band mobility edge is located at 0.0 eV and the conduction band mobility edge is located at 2.22 eV. The shallow and deep hole traps are located at 0.26 eV and 0.87 eV from the valence band mobility edge, respectively. The shallow and deep electron traps are located at 0.35 eV and 1.22 eV from the conduction band mobility edge, respectively. The shallow traps reduce the drift mobility of the electrons and holes, whereas the deep traps prevent the electrons and holes from crossing the a-Se layer.<sup>15</sup> Thus it is the subsequent collection of these deeply trapped electrons or holes that forms the signal that we will define (see Section 3.2.1) as the image lag.



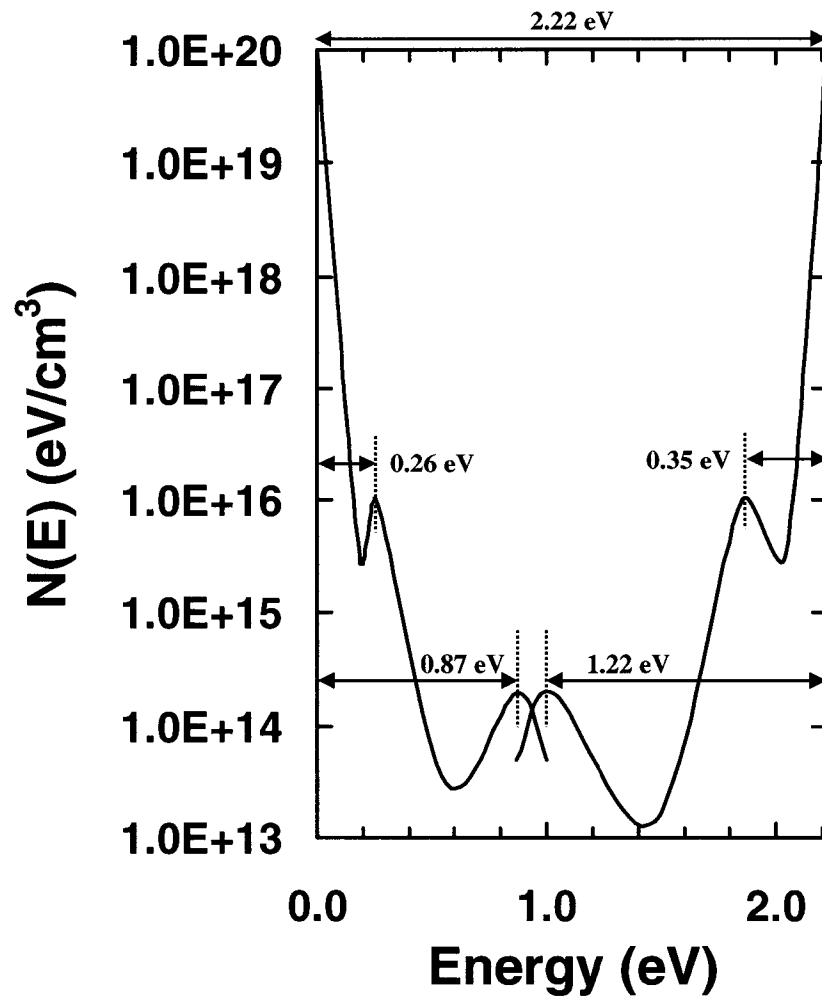


*Fig. 3.4:* The density of states (DOS) for the mobility gap of a-Se as adapted from Abkowitz.<sup>14</sup> The valence band mobility edge is located at 0.0 eV and the conduction band mobility edge is located at 2.22 eV. The shallow and deep hole traps are located at 0.26 eV and 0.87 eV from the valence band mobility edge, respectively. The shallow and deep electron traps are located at 0.35 eV and 1.22 eV from the conduction band mobility edge, respectively.

When x-rays are incident on biased a-Se, EHPs are created, separated by an externally applied electric field, and either the electrons or the holes are collected by the electronics. In our detector, the a-Se has added arsenic (As) impurities to prevent crystallization of the a-Se, as well as, chlorine (Cl) impurities to reduce the trapping sites

caused by the arsenic doping.<sup>15</sup> These trapping sites are not completely eliminated by the chlorine doping, and both shallow and deep traps remain. A fraction of these traps is filled depending upon the amount of radiation incident on the a-Se, resulting in the release of the trapped charges into subsequent frames. The trapped electrons and holes reduce the effective electric field across the a-Se layer, thereby reducing the detector's sensitivity to radiation for subsequent images. Our laboratory has recently reported on the sensitivity reduction on biased a-Se plates.<sup>16</sup> Moreover, the charge trapped due to a single x-ray exposure may be released slowly, producing a signal, and provide the appearance of an object in the images even in the absence of subsequent x-ray exposure.<sup>12,16-18</sup> Lag and ghosting due to lag are defined in Sections 3.2.1 and 3.2.2, respectively.

### 3.2.1 Lag

“Image lag” in a-Se AMFPIs can be defined as the carry-over of trapped charge generated by a single x-ray exposure into subsequent image frames acquired with no x-ray exposure.<sup>12</sup> Normally, lag in the  $n^{th}$  frame ( $L_n$ ) can be described as:

$$L_n = \left( \frac{S_n - B}{S_0 - B} \right) \cdot 100 \quad (3.3)$$

where,  $S_n$  and  $S_0$  are the open-beam mean detector signals in the  $n^{th}$  and the  $0^{th}$  frames respectively, where the  $0^{th}$  frame is acquired immediately following the x-ray exposure. The term “ $B$ ” is the background image obtained without any radiation.

### 3.2.2 Ghosting due to Lag

Ghosting in an image is the appearance of an object that is not present in the beam path. Ghosting due to lag is defined as the residual image of an object after the termination of the x-ray exposure. In this thesis, we have used a high contrast phantom that contains a hole in the center of a 10 x 10 cm<sup>2</sup> lead (Pb) plate. We define residual contrast in the  $n^{\text{th}}$  frame ( $C_n$ ) as follows.

$$C_n = \left( \frac{S_{hole,n} - S_{Pb,n}}{S_{hole,0} - S_{Pb,0}} \right) \cdot 100 \quad (3.4)$$

The residual contrast is used to quantify the severity of the ghosting due to lag for this high contrast phantom. In this equation,  $S_{hole,n}$  and  $S_{hole,0}$  are the mean image signals within the hole in frame number  $n$  and 0, respectively; and  $S_{Pb,n}$  and  $S_{Pb,0}$  are the mean image signals beneath the lead in frame number  $n$  and 0, respectively.

Siewerdsen and Jaffray provide a summary of the recent research and quantification of image lag and long-term image persistence (ghosting due to lag) for indirect and direct AMFPIs.<sup>6</sup> This summary indicates that there is a lag (as defined in Eq. (3.3)) of 2 to 10 % and 0.4 to 1.5 % for indirect and direct AMFPIs, respectively, in the first frame after exposure. The effect of lag on the images of a dynamic imaging application must be differentiated from those due to patient, x-ray tube and/or detector motion.

### 3.3 Lag Measurement

Lag measurement experiments were performed at diagnostic (i.e. 81 kVp and 125 kVp) and at a therapy energy (i.e. 6 MV). The applied electric field across the a-Se layer was 5 V/ $\mu\text{m}$  for all of the lag measurement experiments. The x-ray source from a fluoroscopic simulator (Super 80 CP, Philips Medical Systems, N.A., Bothell, Washington, USA) was used for irradiation at diagnostic energies. The source to detector distance (SDD) for the diagnostic energy experiments was varied for the purpose of attaining specific amounts of radiation (air kerma) incident on the detector, where the x-ray field size was fitted to the sensitive a-Se area. All measurements were performed in the radiographic mode of the simulator.

A Keithley dosimeter (Keithley Instruments, 35055 Digital Dosimeter, Ser. 11808) and a Keithley ion chamber (Keithley Instruments, 96035 15 cc Pancake Ion Chamber, Ser. 13343) were used to measure the amount of incident radiation on the detector. The pancake probe was secured in a stand so that its surface was perpendicular to the beam axis, and placed in the x-ray field at the same SDD as the a-Se AMFPI detector (detector absent during dosimetry measurement). The field size was unchanged from that used for the respective experiment to account for the same amount of scattered radiation. The probe was elevated above the base of the stand which was placed on top of blue styrofoam sheets to minimize backscatter radiation. The styrofoam sheets were used since they backscatter a very small amount of incident radiation. The experimental set-up is shown in Fig. 3.5.

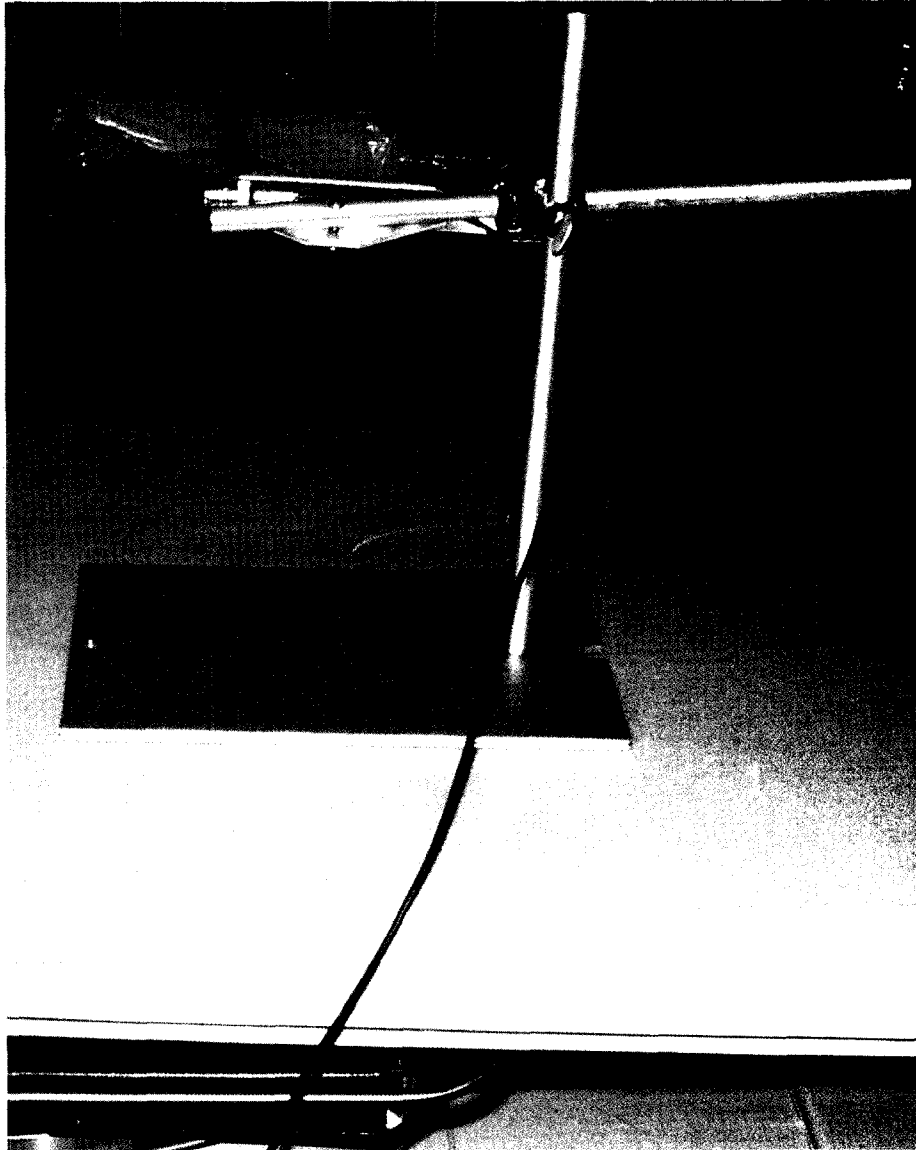


*Fig. 3.5:* The experimental set-up used to measure the amount of incident radiation on the detector for kV energies using a pancake ion chamber.

The Keithley dosimetry system provided exposure measurements in units of mR which was subsequently converted to air kerma using the relation that 1 R is equivalent to 0.00873 Gy (or 1 mR  $\equiv$  8.73  $\mu$ Gy).<sup>19</sup> The Keithley dosimetry system (digital dosimeter and pancake ion chamber) was originally calibrated on June 28, 1982 by the Radiation Measurements Division of Keithley Instruments, Inc. (traceable to the National Institute

of Standards and Technology (NIST)). In our laboratory, this Keithley dosimetry system was measured against an Inovision Radiation Measurements dosimetry system consisting of a dosimeter (Inovision Radiation Measurements, 35050A Dosimeter, Ser. 107038) and an ion chamber (Inovision Radiation Measurements, 96035B 15 cc Pancake Ion Chamber, Ser. 106603) for energies of 40, 60, 81, 102, 121 and 141 kVp on November 27, 2002. For the energy range including the energies used in the research described in this thesis, the two systems were within 2 % discrepancy. The Inovision Radiation Measurements dosimetry system was calibrated by Global Calibration Laboratory (traceable to NIST) on April 30, 2002. The uncertainty of the ion chamber calibration was believed to be  $\pm 3 \%$  and the uncertainty of the dosimeter calibration was 2.8 %, of which 2.0 % was assigned to the uncertainty of the beam. Because calibration factors are normalized to a temperature of 22.0 °C and a pressure of 760 mm Hg, a temperature-pressure correction must also be made. The exposure reading is multiplied by  $C_{T,P}$ , the temperature-pressure correction coefficient given in Eq. (3.5),

$$C_{T,P} = \left[ \frac{273.15 + T}{295.15} \right] \cdot \left[ \frac{760}{P} \right] \quad (3.5)$$

where T is the room temperature in °C and P is the pressure in mm Hg. The incident radiation amounts (corrected for temperature and pressure dependence) used for lag and ghosting measurements for 81 and 125 kVp x-rays are shown in Table 3.1.

Table 3.1: Exposure and air kerma equivalence (corrected for temperature and pressure dependence).

Exposure (mR)	Air Kerma ( $\mu\text{Gy}$ )
2.7	23.6
4.9	42.8
8.9	77.7
10	87
11.0	96.0

A linear accelerator (600C, Varian Medical Systems, Palo Alto, CA, USA) was used for measurements at the therapy energy (6 MV photon beam). Lag measurement experiments utilized a 1.2 mm Cu buildup, a  $7.4 \times 7.4 \text{ cm}^2$  field at the source to axis distance (SAD) of 100 cm, and a SDD of 125 cm for 1 to 4 monitor units (MU) at the dose rate of 250 MU/min. Varian 600C is calibrated to give 1 cGy per MU at a depth of 1.5 cm in water for a  $10 \times 10 \text{ cm}^2$  field size at 100 cm SAD using the TG-51 protocol.<sup>20</sup>

The linear dependence of the AMFPI on the amount of incident radiation was verified for the experimental set-up described in the preceding paragraph and for a frame time of 7.2 s/frame. The frame time is defined as the time interval between the successive read out of a given row of pixels.<sup>6</sup> Three trials were performed each consisting of a hundred and one (101) frames with a ten minute interlude between trials when the high-voltage power supply and detector were shut-down. Five irradiations (6 MV photon beam, 250 MU per minute dose rate) were incident on the detector during each trial: 1 MU of irradiation for frame  $n=40$ , 2 MUs for frame  $n=55$ , 3 MUs for frame  $n=70$ , 4 MUs for frame  $n=85$  and 5 MUs for frame  $n=100$ . The mean image signal of the central  $531 \times 531$  pixels was calculated for all one hundred and one (101) frames in each trial. The background (or dark current) was subtracted from each frame

containing an x-ray irradiation. The background used was the mean image signal of the frame previous to the frame in which the x-ray irradiation was measured (i.e. frames  $n=39, 54, 69, 84$  and  $99$ ). After the background was subtracted, the results from the three trials were averaged for each radiation amount (1 to 5 MUs) and plotted in Fig. 3.6. The slope is 668.68 pixel value counts/MU and the  $R^2$  value is 0.9987. This  $R^2$  value confirms the essential linearity of the flat-panel detector with amount of incident radiation (for a 6 MV x-ray beam).

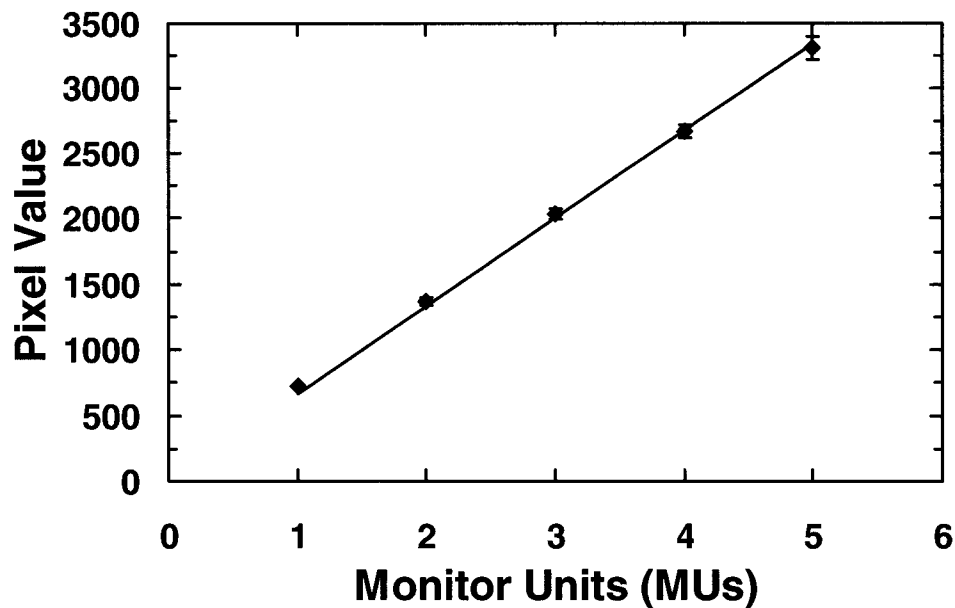


*Fig. 3.6:* The dependence of the a-Se AMFPI average pixel signal (background signal subtracted) for 1 to 5 MUs (250 MU/min) of incident radiation for a 6 MV x-ray beam.

For all three energies, experiments were performed for the three frame times of 5.2, 7.2 and 9.2 s/frame. The frame time is changed by inserting different values of "wait" times in the timing sequence, however, the collection window is always longer than the irradiation time and remains the same for all frame times (approximately 3 seconds). The frame time includes the collection window which corresponds to the



integration period, and is significantly extended to allow enough time for the rotating anode to come up to speed followed by the completed x-ray irradiation. The collection window is also sufficiently long to give 4 MUs of radiation on the Varian 600C linear accelerator with a dose rate of 250 MUs per minute. The beginning of the collection window is signaled by a single audio beep which when heard prompts the operator to turn-on the x-ray beam during the appropriate frame (frame  $n=0$ ). For the sake of consistency, the beep sounds during the background and lag frames as well as the frame in which the x-ray beam is turned-on. The image frame is scanned after the termination of this collection window.

The raw data for each image is composed of a 1024 x 1024 array of 13-bit (-4096 to 4095) counts. In order to avoid the edges of the x-ray field and the penumbra region, the central 531 x 531 pixels ( $\approx 4.5 \times 4.5 \text{ cm}^2$ ) are used to determine the mean signal for each image (this applies to the background images as well). This analysis is performed using MatLab (MathWorks Inc., Natick, MA). Each experimental run consists of the acquisition of a hundred and one (101) images. Fifty images are acquired prior to the x-ray exposure (frame  $n=0$ ) and fifty images are acquired following the x-ray exposure. The fifty images prior to irradiation allow for dark current stability to be established. A graphical example of the image acquisition sequence for lag measurement is illustrated in Fig. 3.7.

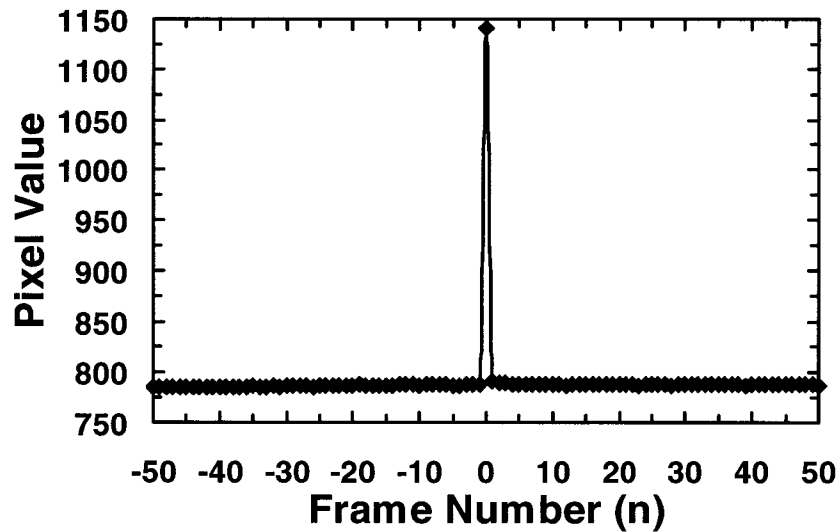


*Fig. 3.7:* Mean image signal (dark current not subtracted) of central 531 x 531 pixels for one hundred and one (101) consecutive image frames. The frame "0" contains the signal due to an x-ray exposure.

The mean dark signal is determined by averaging the mean image signal from the ten dark current images immediately prior to the x-ray exposure. The image lag was calculated from Eq. (3.3) for five image frames immediately following the x-ray exposure (frames  $n=1$  through  $n=5$ ). Each experiment, for a given photon energy, air-kerma and frame time, is repeated eight times at twenty minute intervals with power to the AMFPI, as well as, the high voltage (HV) supply turned off between the trials. The twenty minute interval was chosen based on preliminary data which indicated a reduction in detector sensitivity due to trapped charges in the previous experiment when using a time interval of ten minutes, and satisfied the requirements of reproducible lag values for various imaging parameters. For a given set of experimental parameters, the standard deviation (SD) of  $L_n$  was calculated from these eight measurements.

Any value of  $L_n$  that was outside of  $\pm 1.5$  SD was excluded, and the mean and SD of  $L_n$  were re-calculated from the remaining number of data points ( $\leq 8$ ). It was assumed that the disregarded data points were contaminated by power line interference. Figure 3.8 shows the raw data points of the mean image signal of central 531 x 531 pixels for one experimental run. From this zoomed in view (as compared to Fig. 3.7) the interference of some form of frequency dependent noise can be seen. For example, the data point for frame  $n=5$  is significantly lower than expected.

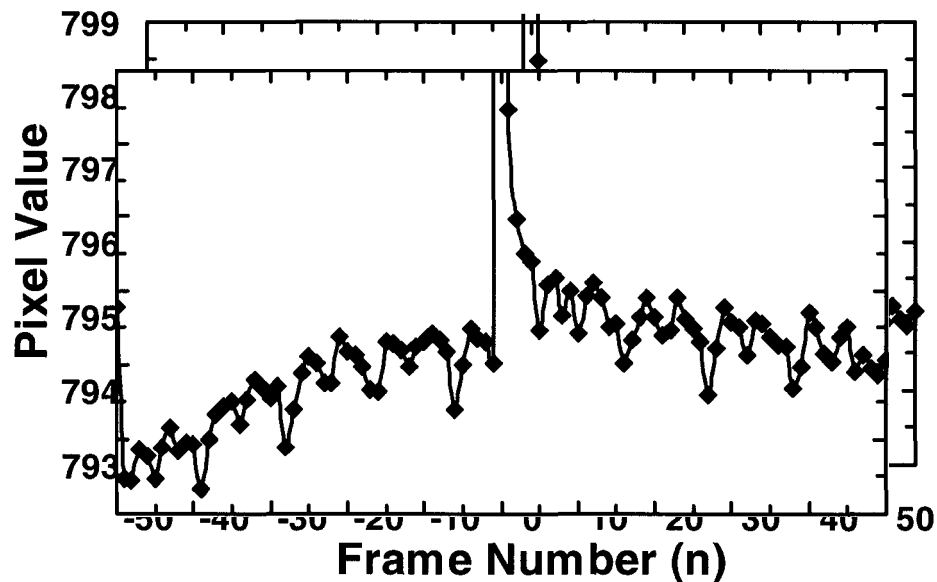


*Fig. 3.8:* A zoomed in view of the mean image signal (dark current not subtracted) of central 531 x 531 pixels for a hundred and one (101) consecutive image frames. The frame "0" (whose point is not visible in this figure) contains the signal due to an x-ray exposure. The error for each visible point is within the diamond symbol.

Please note that the peak at frame  $n=-50$  is random and is due to the previous use of the a-Se detector (there was no x-ray exposure in frame  $n=-50$ ) and is not of interest for our research purposes. Figure 3.9 demonstrates the effect of this frequency dependent

interference on the calculation of lag values using Eq. (3.3). The lag values ( $L_n$ ) are shown for frames  $n=1$  through  $n=15$ . It can be clearly seen that frames  $n=5$ , 8 and 10 in particular, are well below the trend.

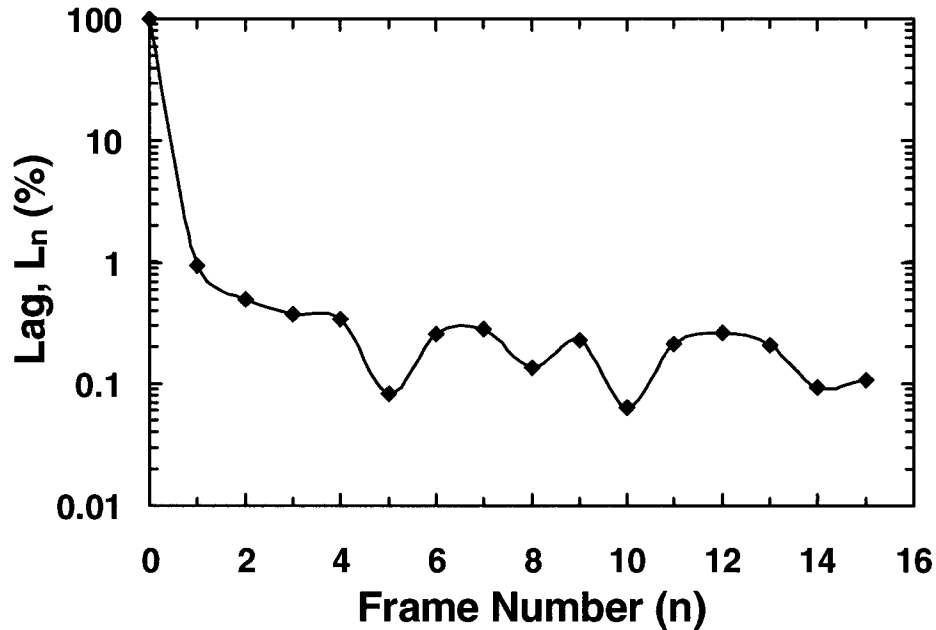


*Fig. 3.9:* Lag values as a function of frame number for one experimental run. Lag values for frames  $n=1$  through  $n=15$  are shown. The error for each point is within the diamond symbol.

Using a trial and error process, the boundary of  $\pm 1.5$  SD was chosen. This boundary was found to exclude lag values that were clearly a result of external factors that detrimentally affected the overall average lag value for a given set of experimental parameters without excluding valuable and even questionable data points. It should be clear that only single lag values were excluded as a result of the  $\pm 1.5$  SD boundary and not entire experimental trials.

It should also be noted at this point that no correction was made for pixel-to-pixel sensitivity variations before averaging the pixels in the central 531 x 531 area. The

results of a verification experiment were analyzed both with correction for pixel-to-pixel sensitivity variations and without any correction. It was determined that analysis with and without the pixel sensitivity correction made no significant difference on the final calculated lag values. Further details on this analysis is given in Section 3.5.1.

### **3.4 Quantification of Ghosting due to Lag**

For the purpose of quantifying the ghosting in a-Se due to lag, a high contrast lead (Pb) phantom, described below, was used. Experiments were performed at the diagnostic energy of 125 kVp as well as the therapy energy of 6 MV. The applied electric field across the a-Se layer was  $5 \text{ V}/\mu\text{m}$  for all ghosting quantification experiments. The source to detector distance (SDD) for the diagnostic energy experiments was set at 120 cm where the x-ray field was fitted to the sensitive a-Se area. The  $10 \times 10 \text{ cm}^2$  lead phantom was 3.2 mm thick with a 1.9 cm diameter hole in the centre. All measurements were performed in the radiographic mode of the simulator using an air-kerma of  $87 \mu\text{Gy}$  (exposure time of 3.0 ms). A similar second square lead phantom of thickness 13.2 mm was used for the MV experiments. For these high energy experiments, a 1.2 mm Cu build-up was placed directly on top of the AMFPI carbon cover, and the 13.2 mm thick high contrast phantom was placed just above the Cu plate with about a 6.5 mm air-gap in between. These experiments used a  $7.4 \times 7.4 \text{ cm}^2$  field at 100 cm SAD. Each irradiation was of 3 MU (250 MU/min), and a SDD of 125 cm was used. For both energies, the experiments to measure ghosting contrast were performed for the three frame times of 5.2, 7.2 and 9.2 s/frame. The frame time was changed by using the same method as in the lag measurement experiments (see Section 3.3).

The experiments to quantify the effects of ghosting were begun by acquiring the flood-field images for the purpose of pixel sensitivity corrections (Eq. (3.7)). Following a twenty minute intermission (AMFPI and HV turned off), the eight sets, each containing a hundred and one (101) images, were acquired with the system power turned off for twenty minutes in between each set. The dark current images used for the pixel sensitivity corrections are the ten dark current images immediately prior to the x-ray exposure. The contrast was determined using Eq. (3.4) for five image frames immediately following the x-ray exposure (frames  $n=1$  through  $n=5$ ). For a given set of experimental parameters, the standard deviation (SD) of  $C_n$  was calculated from these eight measurements. Any value of  $C_n$  that was outside of  $\pm 1.5$  SD was excluded, and the mean and SD of  $C_n$  were re-calculated from the remaining number of data points ( $\leq 8$ ), again to disregard data points that were contaminated by power line interference.

### **3.5 Post Processing Correction for Variations in Pixel Sensitivity**

#### **3.5.1 Lag**

As mentioned above in Section 3.3, no correction was made for pixel-to-pixel sensitivity variations for the quantification of image lag. It was determined that analysis with and without pixel sensitivity correction made no significant difference on the final calculated lag values. The details of this comparison, verification and justification are described below.

We performed an experiment containing three experimental runs (a hundred and one frames (101) in each run), subject to the same experimental conditions as the lag experiments described in Section 3.3 for a 6 MV x-ray beam: 1.2 mm Cu buildup, 7.4 x

7.4 cm<sup>2</sup> field (at SAD = 100 cm), SDD = 125 cm and 5 V/μm applied electric field across the a-Se layer. The experimental parameters chosen were a 6 MV x-ray beam, delivery of 3 MUs (250 MU/min) of radiation and a frame time of 7.2 s/frame. A flood-field acquisition sequence was initially run followed by the three experimental lag runs. The flood-field acquisition sequence consisted of forty-one image frames, thirty dark current frames at 7.2 s/frame followed by eleven flood-field frames at 21.2 s/frame (chosen such that x-ray irradiations were far enough apart that lag from previous frames could be considered negligible). The first flood-field frame (frame  $n=31$ ) was discarded (due to inconsistent signal results dependent on the previous irradiation of the detector) and the 2-D image arrays (1024 x 1024) of the remaining ten flood-field frames (frames  $n=32$  to  $n=41$ ) were averaged and used in Eq. (3.6), symbolized by  $I_{flood}$ . Twenty minute intervals with power to the AMFPI, and the high voltage (HV) supply turned off were inserted between all four sequences.

The first step in the analysis was to calculate the lag values (mean and SD) without any pixel sensitivity corrections performed. All the  $L_n$  data were within the  $\pm 1.5$  SD criteria thus not requiring any exclusion of data. The results are displayed in Table 3.2.

Table 3.2: Lag values ( $L_n$ ) for the pixel sensitivity verification experiment (6 MV, 3 MUs (250 MU/min), 7.2 s/frame) including the results for no pixel sensitivity correction and the results with pixel sensitivity correction.

$L_n$	No Pixel Sensitivity Correction	With Pixel Sensitivity Correction
$L_1$ (%)	0.60 +/- 0.01	0.60 +/- 0.01
$L_2$ (%)	0.328 +/- 0.005	0.327 +/- 0.005
$L_3$ (%)	0.232 +/- 0.004	0.231 +/- 0.004
$L_4$ (%)	0.187 +/- 0.001	0.187 +/- 0.002
$L_5$ (%)	0.151 +/- 0.006	0.151 +/- 0.006

The method used to correct for the variations in pixel sensitivity is described below. The pixel values for each image (background and signal images) were corrected for pixel-to-pixel sensitivity variations by using dark current and flood-field images in the following manner:

$$I_{norm} = \left[ \frac{I_{image} - I_{dark}}{I_{flood} - I_{dark}} \right] \cdot 100 \quad (3.6)$$

where,  $I_{norm}$ ,  $I_{image}$ ,  $I_{flood}$ , and  $I_{dark}$  are the 2-D arrays (1024 x 1024) corresponding to the corrected image, the raw image, the average image of ten flood-field (open beam) images, and the average image of ten dark current images, respectively.

The dead and saturated pixels were identified as follows. An array mask corresponding to dead or saturated pixels was generated from the  $(I_{flood} - I_{dark})$  image using the fixed criteria described next. The mean pixel value was calculated from the  $(I_{flood} - I_{dark})$  image. The mask contained a value of "1" if the particular pixel value was either less than one half or more than twice this mean pixel value. The remaining values were set to "0". The pixels in the  $(I_{flood} - I_{dark})$  image that corresponded to a mask



value of “1” were replaced by the mean pixel value and the pixels corresponding to a mask value of “0” were left unchanged. The pixels in the  $(I_{image} - I_{dark})$  image, corresponding to the mask of "1", were replaced by the median in a 3 x 3 pixel neighbourhood; whereas the pixels corresponding to the mask of “0”, were left unchanged.

This correction algorithm was applied to sixteen images for each experimental run including the ten background images prior to the x-ray exposure (frames  $n=-10$  through  $n=-1$ ), the image containing the signal resulting from the x-ray exposure (frame  $n=0$ ) and the five images following the x-ray exposure (frames  $n=1$  through  $n=5$ ). The corrected images were then used to determine the image lag for frames  $n=1$  through  $n=5$  using Eq. (3.3). The results are also displayed in Table 3.2.

It has been demonstrated with confidence (Table 3.2) that analysis with or without correction for variations in pixel sensitivity has negligible effect on the quantification of image lag. Justification has thus been provided for the accurate and precise quantification of lag for our specific detector and experimental procedures without including in our analysis the above described correction algorithm for variations in pixel sensitivity.

### **3.5.2 Ghosting due to Lag**

Similar correction was used to analyze ghosting within the phantom image. The pixel values in the phantom images were corrected using dark current and flood-field images in order to correct for pixel-to-pixel sensitivity variations in the AMFPI:

$$I_{norm} = \left[ \frac{I_{phantom} - I_{dark}}{I_{flood} - I_{dark}} \right] \cdot 100 \quad (3.7)$$

where,  $I_{norm}$ ,  $I_{phantom}$ ,  $I_{flood}$ , and  $I_{dark}$  are the 2-D arrays (1024 x 1024) corresponding to the corrected phantom image, the raw phantom image, the average image of ten flood-field (open beam) images, and the average image of ten dark current images, respectively. The flood-field images were acquired using the same sequence described in Section 3.5.1 where the frame time during the thirty dark current frames was chosen to be the same as the frame time used in the ghosting-quantification experiment. The dead and saturated pixels were identified as follows. An array mask corresponding to dead or saturated pixels was generated from the  $(I_{flood} - I_{dark})$  image. The mean was calculated from the  $(I_{flood} - I_{dark})$  image. The array mask was used in the identical manner as described above in Section 3.5.1, the only difference being the nomenclature of one of the symbols in the numerator of Eq. (3.6) and Eq. (3.7).

The residual contrast as defined by Eq. (3.4) was calculated from the  $I_{norm}$  images.  $S_{hole,n}$  was determined by finding the mean within a square area (81 x 81 pixels) located entirely within the image of the hole in the lead (Pb) phantom. This area is represented by the shaded region inside of the hole in Fig. 3.10.  $S_{pb,n}$  was determined by finding the mean pixel value from four rectangular areas creating a frame-like structure around the image of the hole. The total number of pixels within these four rectangular areas is two hundred and nine thousand, six hundred (209 600) pixels and is illustrated by the four shaded regions outside of the hole in Fig. 3.10. All five areas avoid the penumbra region located around the perimeter of the image of the hole.

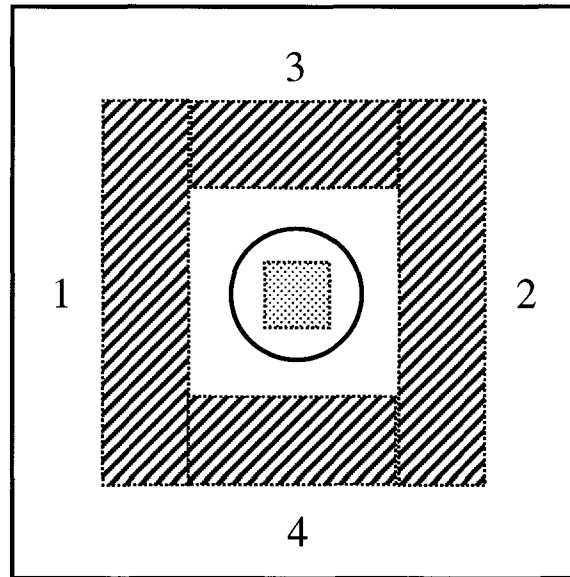


*Fig. 3.10:* A schematic of the lead phantom (top view) where the four shaded areas outside of the hole define the regions from which  $S_{Pb,n}$  was calculated. The shaded area inside of the hole defines the region where  $S_{hole,n}$  was calculated. The area inside of the hole is 81 x 81 pixels; areas 1 and 2 are 531 x 131 pixels; and areas 3 and 4 are 131 x 269 pixels.

For each ghosting experiment the avoidance of the penumbra region was confirmed by “zooming-in” on the display of the relevant areas (analysis performed using MatLab). It was important to perform this quality assurance check for each experiment as there were slight shifts in the placement of the lead phantom between experiments. Figure 3.11 (b) illustrates the situation where a portion of the penumbra region would be used in the calculation of the contrast values. This can be seen by the obvious misplacement of the central region and the surrounding frame-like structure. It is expected for the central region to be completely gray indicating that it is located completely within the hole of the lead phantom, away from the perimeter. The accurate

placement of this central region is shown in Fig. 3.12 (b) shown to be completely gray with no darker areas or fringes.

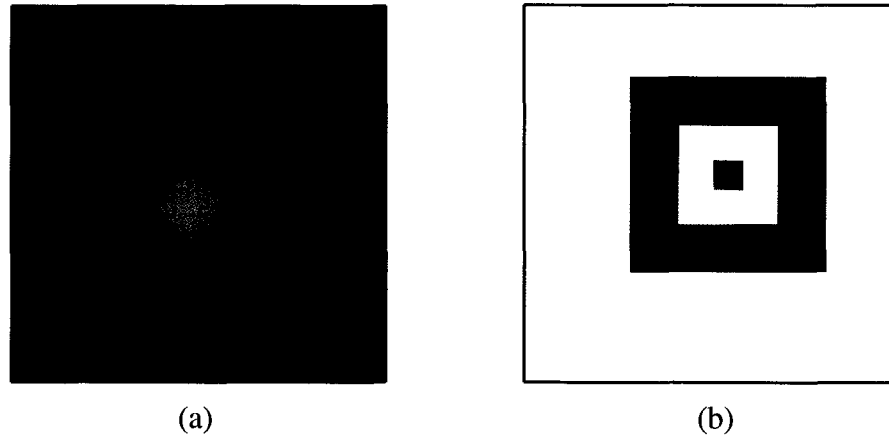


*Fig. 3.11:* This figure is an example of improper placement of the five areas used to calculate  $S_{hole,n}$  and  $S_{pb,n}$  shown by the display of: (a) the entire 1024 x 1024 image of the  $n=0$  frame; (b) the central region used to calculate  $S_{hole,n}$  and the surrounding frame-like structure used to calculate  $S_{pb,n}$  shown to be improperly placed.

Figure 3.12 (b) illustrates the proper location of the five regions for the accurate calculation of  $S_{hole,n}$  and  $S_{pb,n}$ . There is no evidence of any grayish fringes around the perimeter of the surrounding frame-like structure in Fig. 3.12 (b) indicating proper placement for the accurate calculation of  $S_{pb,n}$ . Due to the relative size of the five regions compared to the actual physical size of the hole in the lead phantom and the surrounding lead phantom area, this qualitative approach is sufficient for quality assurance purposes.

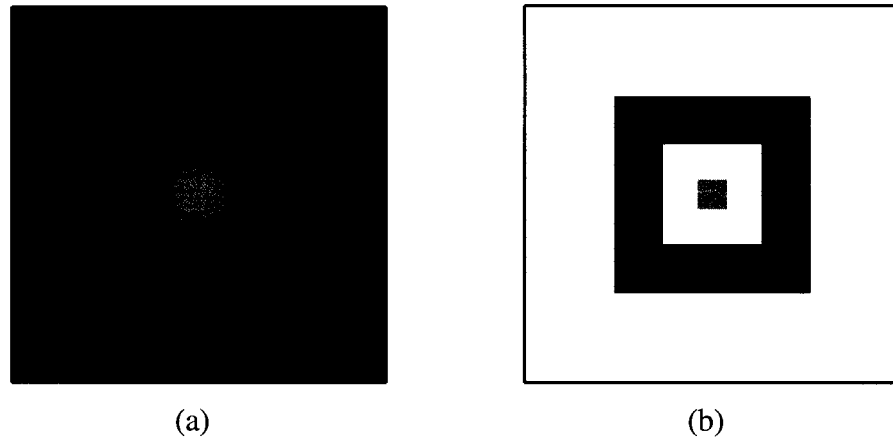


*Fig. 3.12:* This figure is an example of proper placement of the five areas used to calculate  $S_{\text{hole},n}$  and  $S_{\text{Pb},n}$  shown by the display of: (a) the entire 1024 x 1024 image of the  $n=0$  frame; (b) the central region used to calculate  $S_{\text{hole},n}$  and the surrounding frame-like structure used to calculate  $S_{\text{Pb},n}$  shown to be properly placed.

### 3.6 Notes

[1] M. Lachaine, E. Fourkal, and B. G. Fallone, “Detective quantum efficiency of a direct-detection active matrix flat panel imager at megavoltage energies,” *Med. Phys.* **28** (7), 1364-1372 (2001).

[2] A. Debie, B. Polischuk, H. Rougeot, M. Hansroul, E. Poliquin, M. Caron, K. Wong, Z. Shukri, and J. Martin, “Quantitative analysis of performance of selenium flat-panel detector for interventional mammography,” *Proc. SPIE* **3977**, 176-184 (2000).

[3] G. Pang, W. Zhao, and J. A. Rowlands, “Digital radiology using active matrix readout of amorphous selenium: Geometrical and effective fill factors,” *Med Phys* **25** (9), 1636-1646 (1998).

- [4] M. Lachaine, E. Fourkal, and B. G. Fallone, "Investigation into the physical characteristics of active matrix flat panel imagers for radiotherapy," *Med. Phys.* **28** (8), 1689-1695 (2001).
- [5] B. Polischuk, H. Rougeot, K. Wong, A. Debrie, E. Poliquin, M. Hansroul, J. Martin, T. Truong, M. Choquette, L. Laperrière, and Z. Shukri, "Direct conversion detector for digital mammography," *Proc. SPIE* **3659**, 417-425 (1999).
- [6] J. H. Siewerdsen and D. A. Jaffray, "A ghost story: Spatio-temporal response characteristics of an indirect-detection flat-panel imager," *Med. Phys.* **26** (8), 1624-1641 (1999).
- [7] P. R. Granfors, "Performance characteristics of an amorphous silicon flat panel x-ray imaging detector," *Proc. SPIE* **3659**, 480-490 (1999).
- [8] N. Jung, P. L. Alving, F. Busse, N. Conrads, H. M. Meulenbrugge, W. Rütten, U. Schiebel, M. Weibrecht, and H. Wiczorek, "Dynamic x-ray imaging system based on an amorphous silicon thin-film array," *Proc. SPIE* **3336**, 396-407 (1998).
- [9] T. J. C. Bruijns, P. L. Alving, E. L. Baker, R. Bury, A. R. Cowen, N. Jung, H. A. Luijendijk, H. J. Meulenbrugge, and H. J. Stouten, "Technical and clinical results of an experimental flat dynamic (digital) x-ray image detector (FDXD) system with real-time corrections," *Proc. SPIE* **3336**, 33-44 (1998).

- [10] B. Polischuk, Z. Shukri, A. Legros, and H. Rougeot, "Selenium direct converter structure for static and dynamic x-ray detection in medical imaging applications," Proc. SPIE **3336**, 494-504 (1998).
- [11] A. Tsukamoto, S. Yamada, T. Tomisaki, M. Tanaka, T. Sakaguchi, H. Asahina, and M. Nishiki, "Development of a selenium-based flat-panel detector for real-time radiography and fluoroscopy," Proc. SPIE **3336**, 388-395 (1998).
- [12] W. Zhao, G. DeCrescenzo, and J. A. Rowlands, "Investigation of lag and ghosting in amorphous selenium flat-panel x-ray detectors," Proc. SPIE **4682**, 9-20 (2002).
- [13] R. L. Weisfield, M. Hartney, R. Schneider, K. Aflatooni, and R. Lujan, "High performance amorphous silicon image sensor for x-ray diagnostic medical imaging applications," Proc. SPIE **3659**, 307-317 (1999).
- [14] M. Abkowitz, "Density of states in a-Se from combined analysis of xerographic potentials and transient transport data," Philos. Mag. Lett. **58** (1), 53-57 (1988).
- [15] J. A. Rowlands and S. O. Kasap, "Amorphous semiconductors usher in digital x-ray imaging," Phys. Today **50** (11), 24-30 (1997).
- [16] S. Steciw, T. Stanescu, S. Rathee, and B. G. Fallone, "Sensitivity reduction in biased amorphous selenium photoconductors," J. Phys. D **35**, 2716-2722 (2002).

- [17] U. Schiebel, T. Buchkremer, G. Frings, and P. Quadflieg, "Deep trapping and recombination in a-Se:As x-ray sensitive photoreceptors," *J. Non-Cryst. Solids* **115**, 216-218 (1989).
- [18] J. Kalade, E. Montrimas, and J. Rakauskas, "The mechanism of sensitivity reduction in selenium layers irradiated by x-rays," *Phys. Stat. Sol. A* **25**, 629-636 (1974).
- [19] H. E. Johns and J. R. Cunningham, *The Physics of Radiology*, Fourth ed. (Charles C Thomas, Springfield, 1983).
- [20] P. R. Almond, P. J. Biggs, B. M. Coursey, W. F. Hanson, M. S. Huq, R. Nath, and D. W. O. Rogers, "AAPM's TG-51 protocol for clinical reference dosimetry of high-energy photon and electron beams," *Med. Phys.* **26** (9), 1847-1870 (1999).

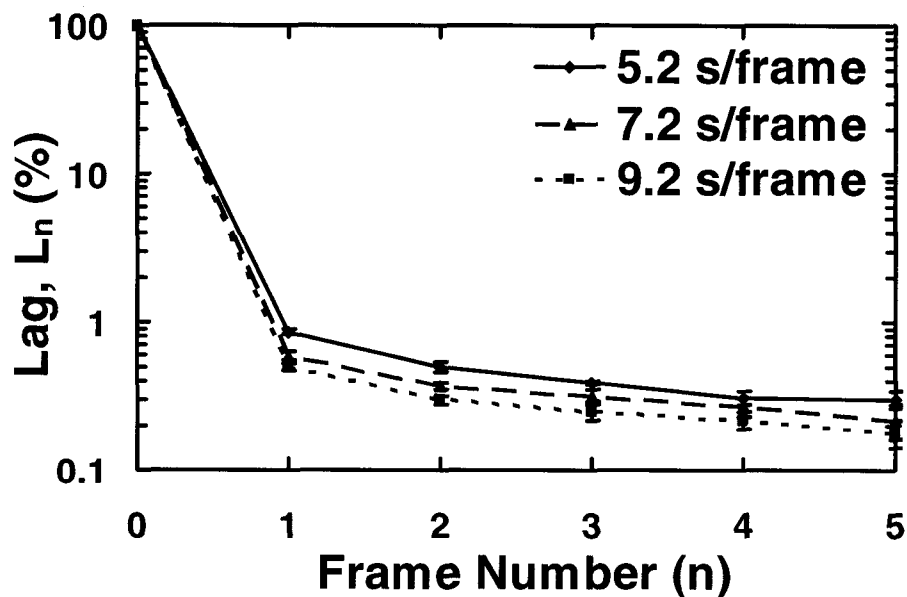


## Chapter 4: Results and Discussion

The "lag" and "residual contrast" (defined in Eqs. (3.3) and (3.4), respectively) are presented as a function of time after exposure for various sets of photon energy, frame time and air-kerma. The data points in all the graphs are the mean values of  $\leq 8$  experiments and error bars represent the plus or minus standard deviation ( $\pm$  SD).

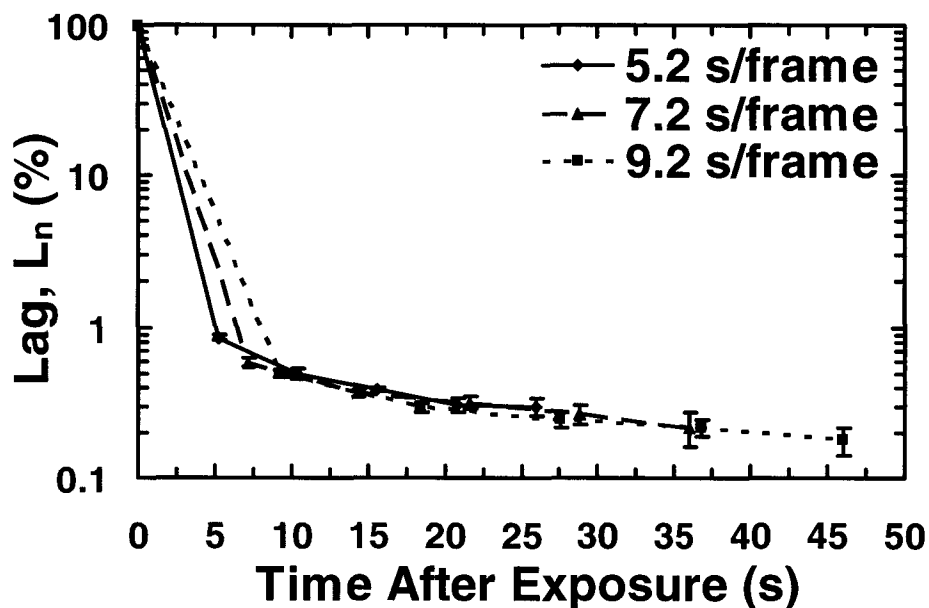
### 4.1 Lag

Figure 4.1 shows " $L_n$ " for frames  $n=1$  through  $n=5$  measured with an 81 kVp beam using an air-kerma of  $42.8 \mu\text{Gy}$  (exposure time of 3.2 ms), and three frame times (5.2, 7.2 and 9.2 s per frame). This figure shows that " $L_n$ " decreases as a function of frame number and, for a given frame number, " $L_n$ " decreases for a higher frame time.



*Fig. 4.1:* Experimental lag values as a function of frame number after exposure for 81 kVp,  $42.8 \mu\text{Gy}$  (exposure time of 3.2 ms), and three frame times.

The same data is displayed in Fig. 4.2 as a function of time after exposure (frame number multiplied by frame time). The difference between frame times in Fig. 4.1 disappears in Fig. 4.2 where the three series of curves lie on top of each other when plotted as a function of the time after the x-ray exposure. Thus lag decreases with the time after the x-ray exposure irrespective of the frame time. Because the lag is a measure of the amount of charge released from the traps, lag would decrease as a function of time after exposure since the concentration of trapped charges is decreasing as a function of time.



*Fig. 4.2:* Experimental lag values as a function of time after exposure for 81 kVp, 42.8  $\mu$ Gy (exposure time of 3.2 ms), and three frame times.

The plots in Figs. 4.3 – 4.5 (81 kVp: 23.6, 77.7 and 96.0  $\mu$ Gy respectively) also confirm these results. Figures 4.6 – 4.9 (125 kVp: 23.6, 42.8, 77.7 and 96.0  $\mu$ Gy respectively) provide further evidence that, within experimental error, lag decreases with the time after the x-ray exposure irrespective of the frame time.

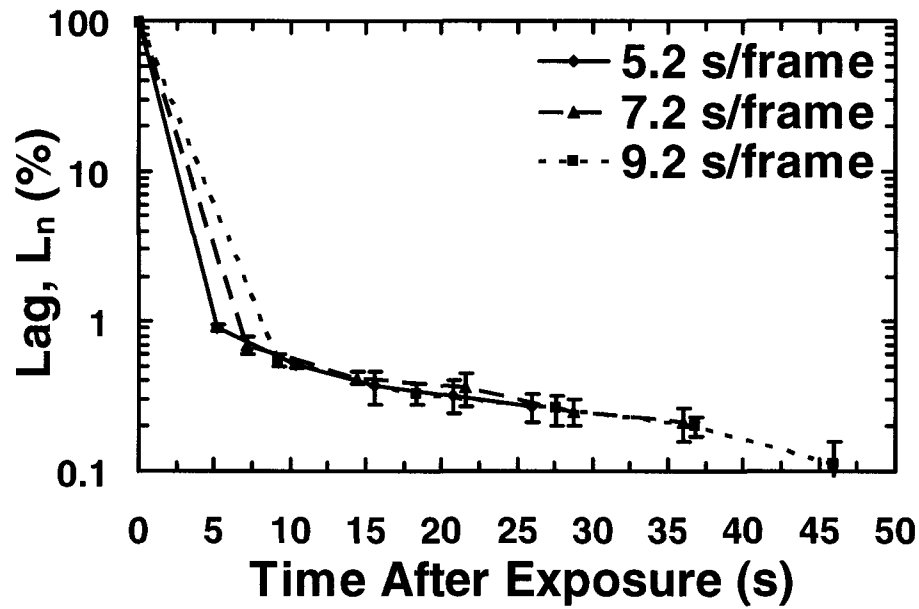


Fig. 4.3: Experimental lag values as a function of time after exposure for 81 kVp, 23.6  $\mu$ Gy (exposure time of 1.6 ms), and three frame times.

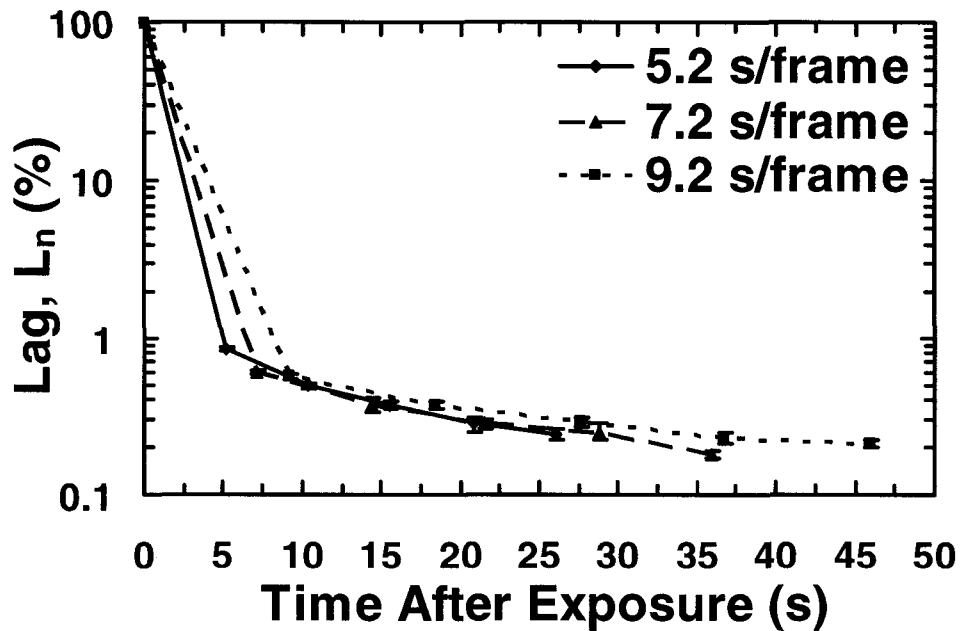


Fig. 4.4: Experimental lag values as a function of time after exposure for 81 kVp, 77.7  $\mu$ Gy (exposure time of 6.4 ms), and three frame times.

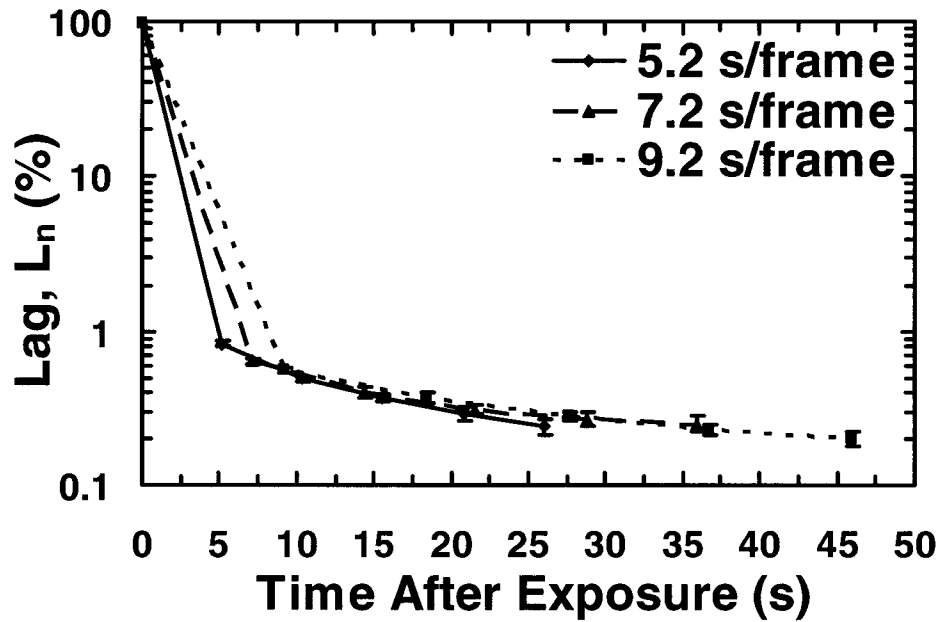


Fig. 4.5: Experimental lag values as a function of time after exposure for 81 kVp, 96.0  $\mu$ Gy (exposure time of 8.0 ms), and three frame times.

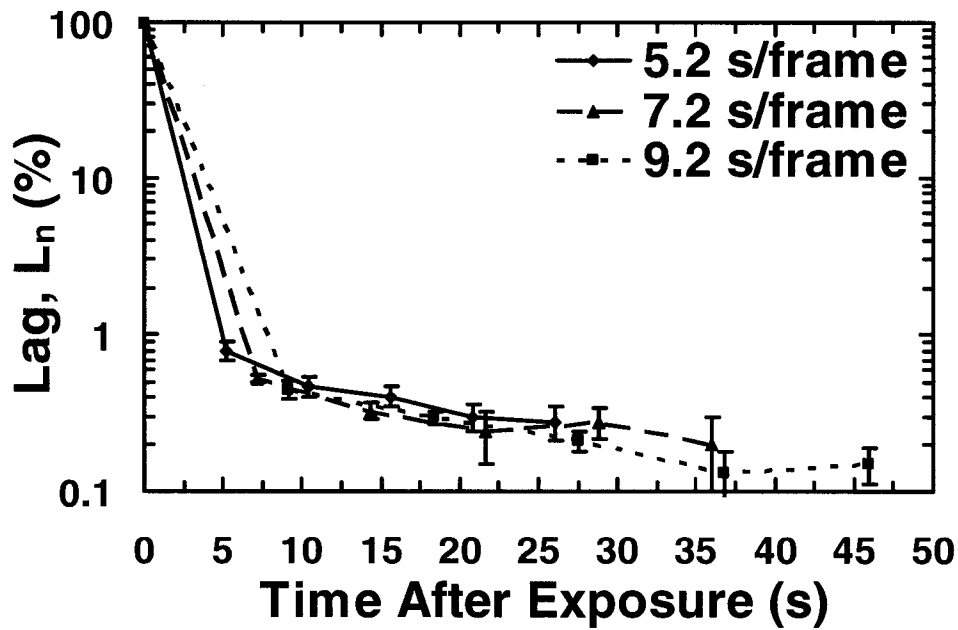


Fig. 4.6: Experimental lag values as a function of time after exposure for 125 kVp, 23.6  $\mu$ Gy (exposure time of 2.5 ms), and three frame times.

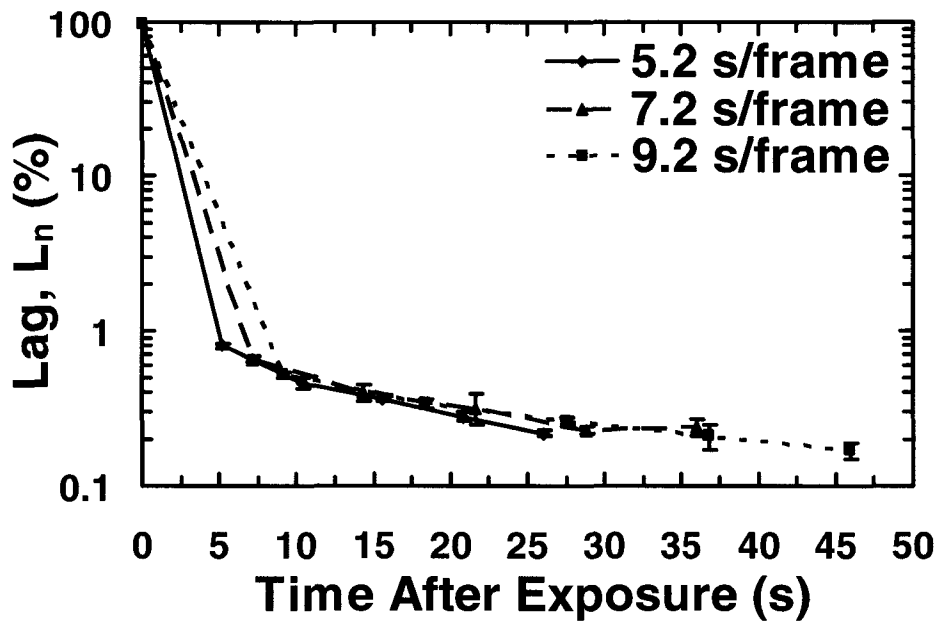


Fig. 4.7: Experimental lag values as a function of time after exposure for 125 kVp, 42.8  $\mu$ Gy (exposure time of 2.5 ms), and three frame times.

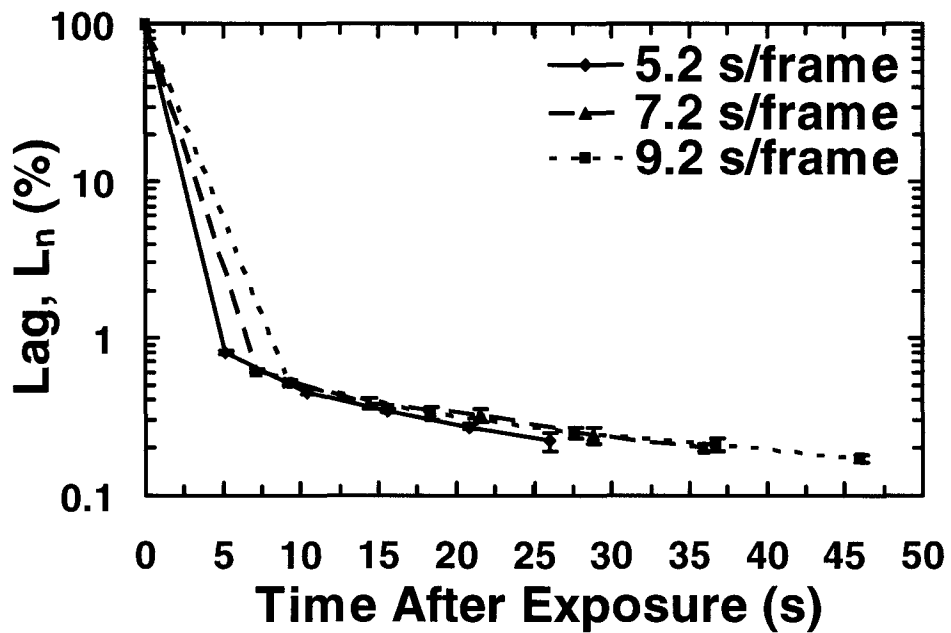


Fig. 4.8: Experimental lag values as a function of time after exposure for 125 kVp, 77.7  $\mu$ Gy (exposure time of 2.5 ms), and three frame times.

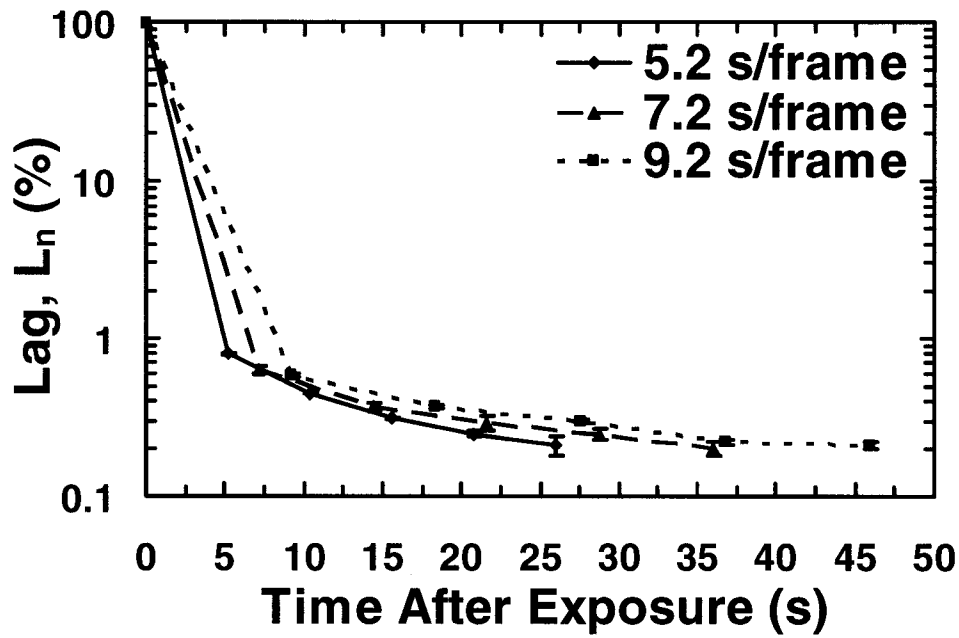


Fig. 4.9: Experimental lag values as a function of time after exposure for 125 kVp, 96.0  $\mu$ Gy (exposure time of 4.0 ms), and three frame times.

The similar dependence of " $L_n$ " on the time after exposure is shown in Fig. 4.10 for a 6 MV photon beam. This is in general agreement with the results summarized in Siewerdsen and Jaffray, specifically that lag decreases in subsequent image frames.<sup>1</sup>

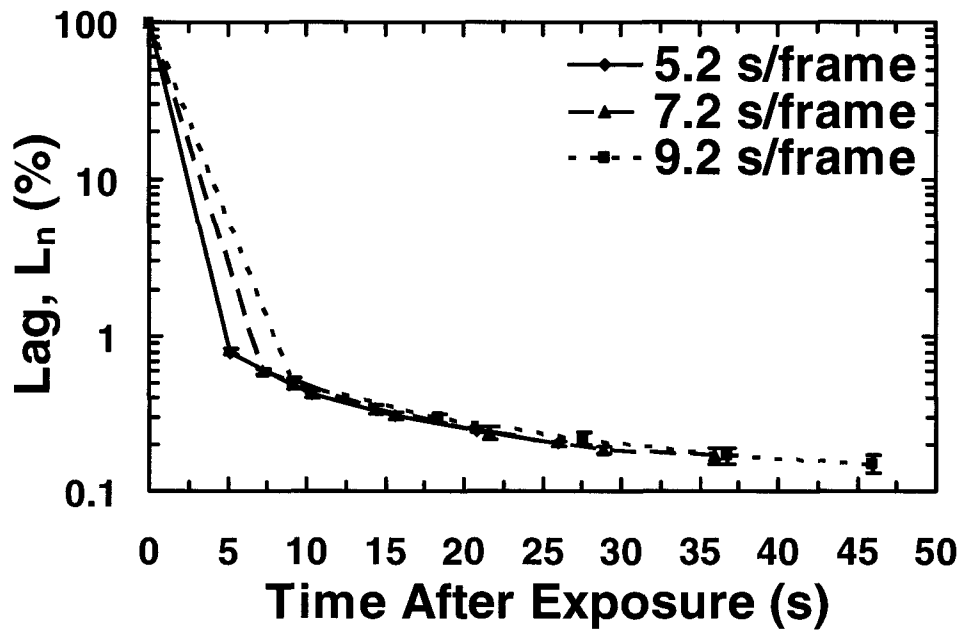


Fig. 4.10: Experimental lag values as a function of time after exposure for 6 MV, 1MU (250 MU/min), and three frame times.

Figures 4.11 – 4.13 also display the dependence of " $L_n$ " on the time after exposure for a 6 MV photon beam for 2, 3 and 4 MUs respectively. Figure 4.12 appears to demonstrate a trend that is dependent on the frame time. The reason for this is unknown as no trend should appear according to the majority of the other results. Therefore it is concluded that Fig. 4.12 may contain experimental errors and does not reflect what is actually taking place.

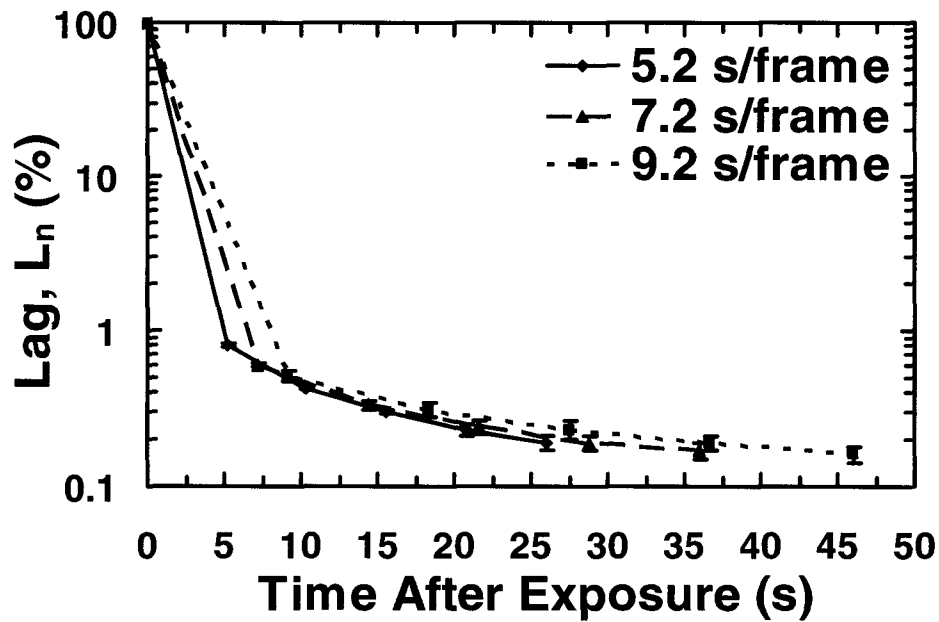


Fig. 4.11: Experimental lag values as a function of time after exposure for 6 MV, 2 MU (250 MU/min), and three frame times.

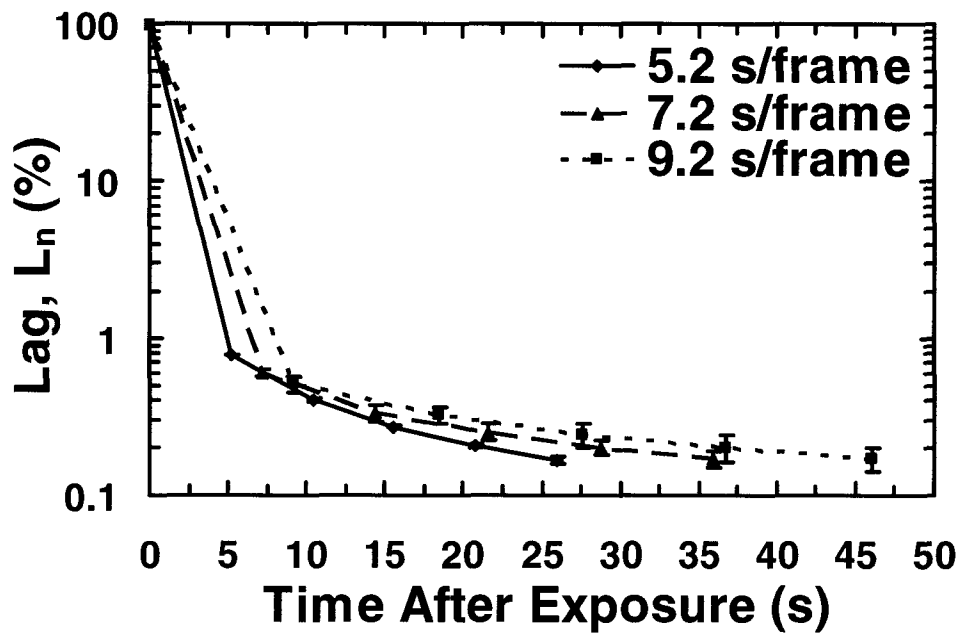


Fig. 4.12: Experimental lag values as a function of time after exposure for 6 MV, 3 MU (250 MU/min), and three frame times.



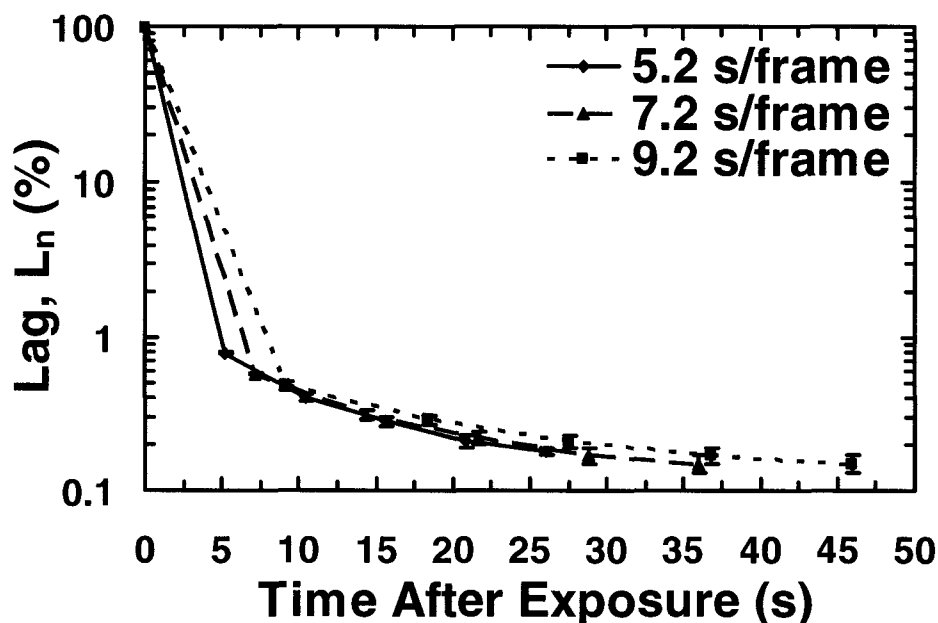
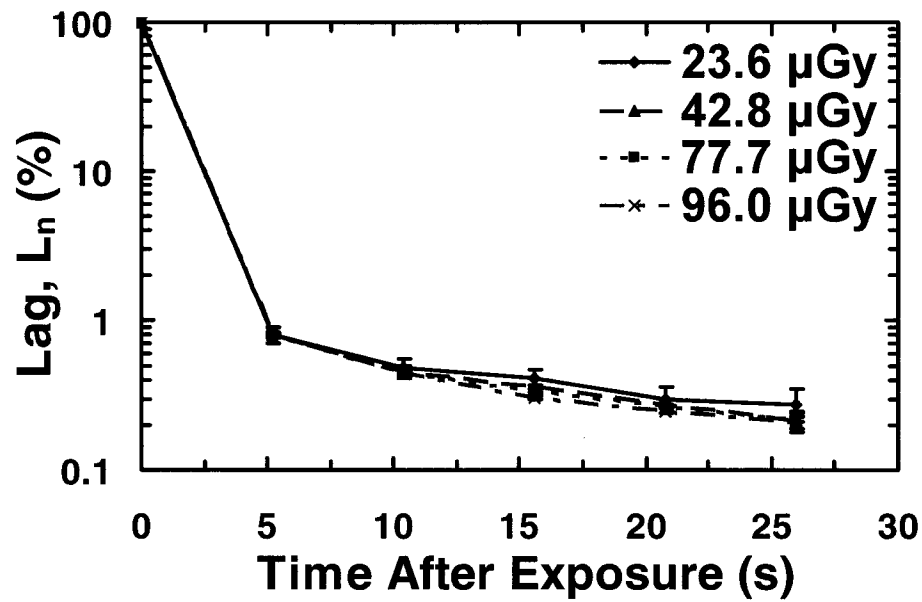


Fig. 4.13: Experimental lag values as a function of time after exposure for 6 MV, 4 MU (250 MU/min), and three frame times.

Figure 4.14 shows " $L_n$ " for air-kerma values of 23.6, 42.8, 77.7 and 96.0  $\mu\text{Gy}$  at 125 kVp and a frame time of 5.2 s/frame. It can be inferred from Fig. 4.14 that the amount of charge trapped and subsequently released increases linearly with the incident energy fluence (or air-kerma). Since " $L_n$ " values are normalized to the pixel count in frame  $n=0$ , the variations in released charge for various air-kerma are removed due to the normalization. Thus, " $L_n$ " values displayed in Fig. 4.14 show no dependence on air-kerma. A possible physical reason for this lack of dependence on air-kerma is the decoupling of the charge producer (a-Se bulk) and the charge storage devices (storage capacitors) in our direct detection ANRAD a-Se IMAM detector.



*Fig. 4.14:* Experimental lag values as a function of time after exposure for 125 kVp, 5.2 s/frame, and four air-kerma values (exposure times of 2.5, 2.5, 2.5 and 4.0 ms respectively).

The same result is demonstrated in Figs. 4.15 – 4.16 (125 kVp: 7.2 and 9.2 s/frame respectively), Figs. 4.17 – 4.19 (81 kVp: 5.2, 7.2 and 9.2 s/frame respectively) and Figs. 4.20 – 4.22 (6 MV: 5.2, 7.2 and 9.2 s/frame respectively).

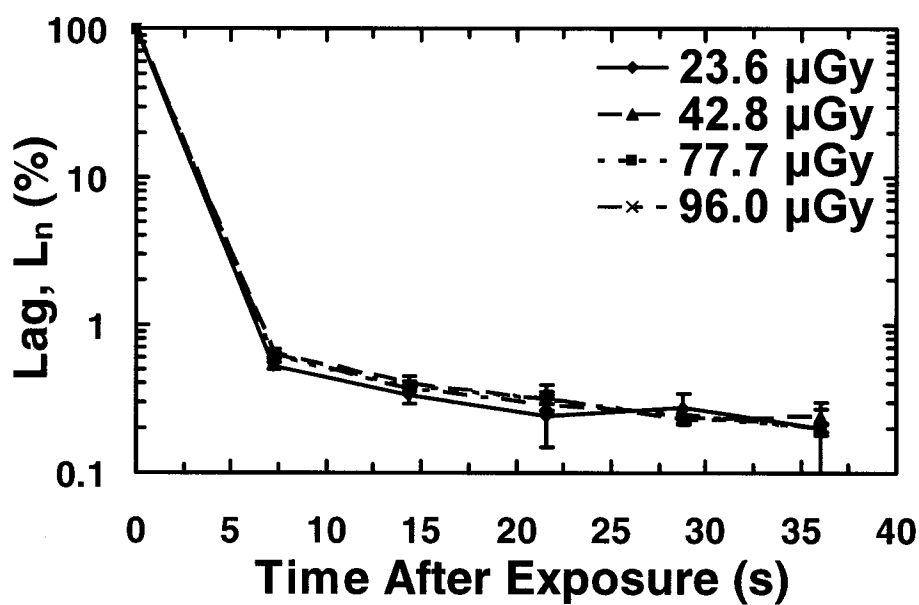


Fig. 4.15: Experimental lag values as a function of time after exposure for 125 kVp, 7.2 s/frame, and four air-kerma values (exposure times of 2.5, 2.5, 2.5 and 4.0 ms respectively).

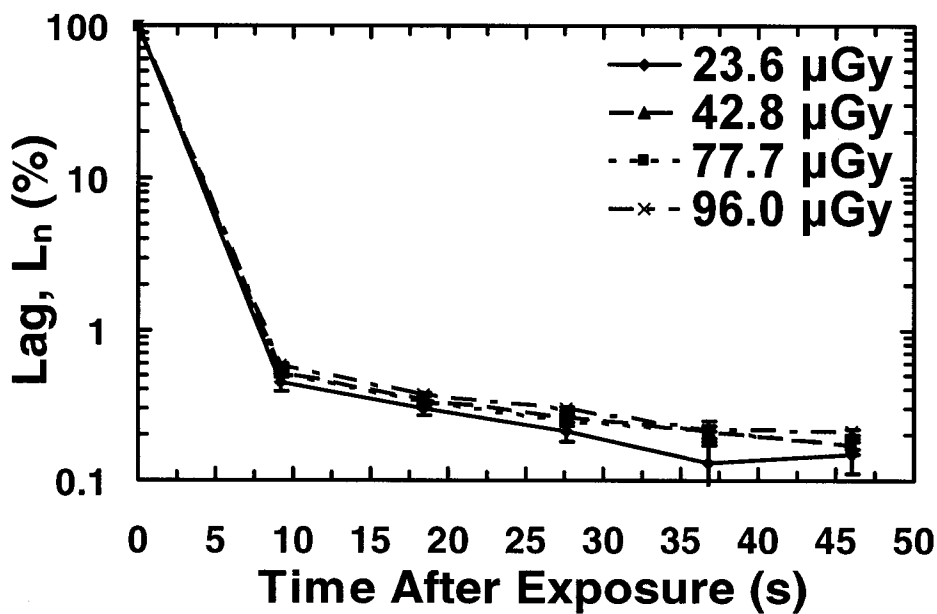


Fig. 4.16: Experimental lag values as a function of time after exposure for 125 kVp, 9.2 s/frame, and four air-kerma values (exposure times of 2.5, 2.5, 2.5 and 4.0 ms respectively).

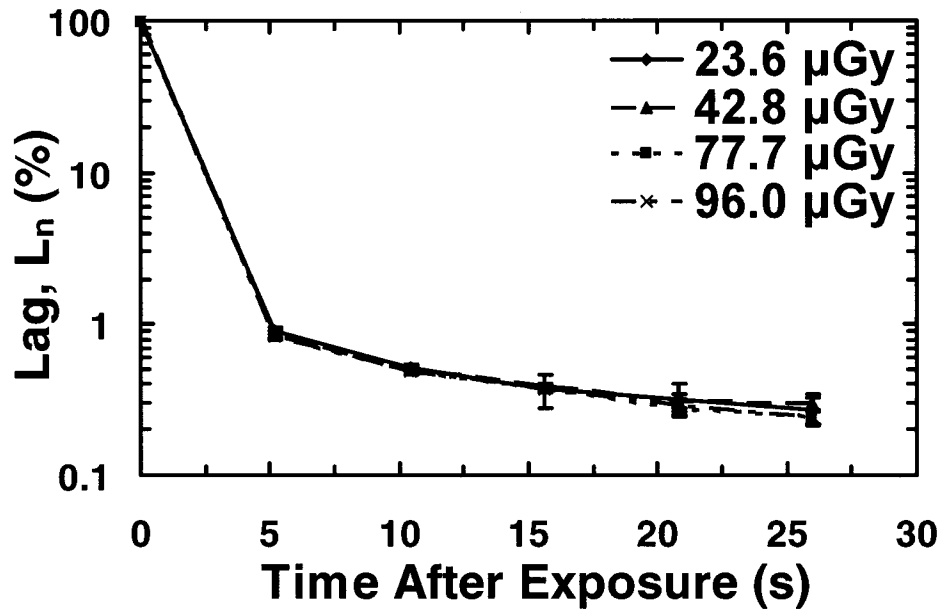


Fig. 4.17: Experimental lag values as a function of time after exposure for 81 kVp, 5.2 s/frame, and four air-kerma values (exposure times of 1.6, 3.2, 6.4 and 8.0 ms respectively).

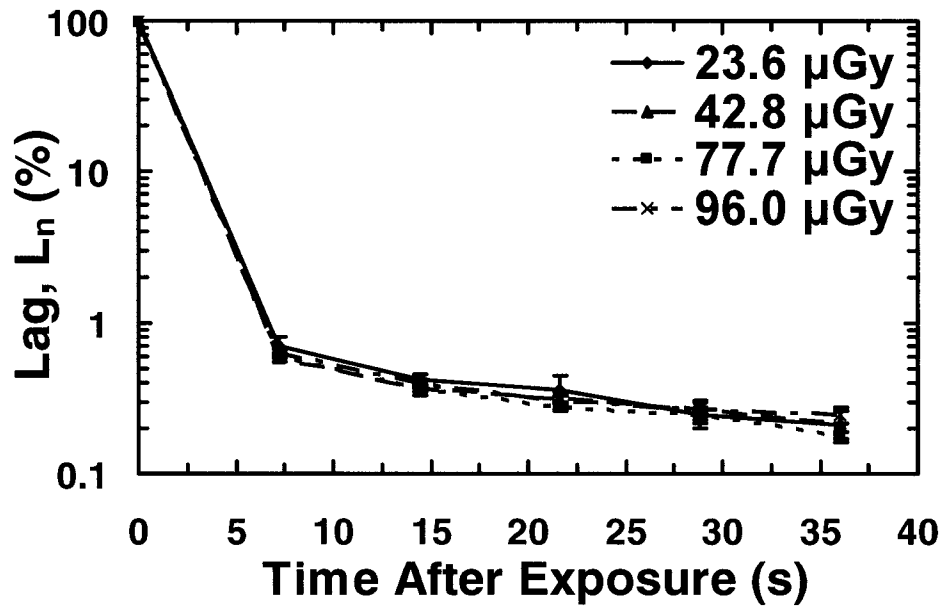


Fig. 4.18: Experimental lag values as a function of time after exposure for 81 kVp, 7.2 s/frame, and four air-kerma values (exposure times of 1.6, 3.2, 6.4 and 8.0 ms respectively).

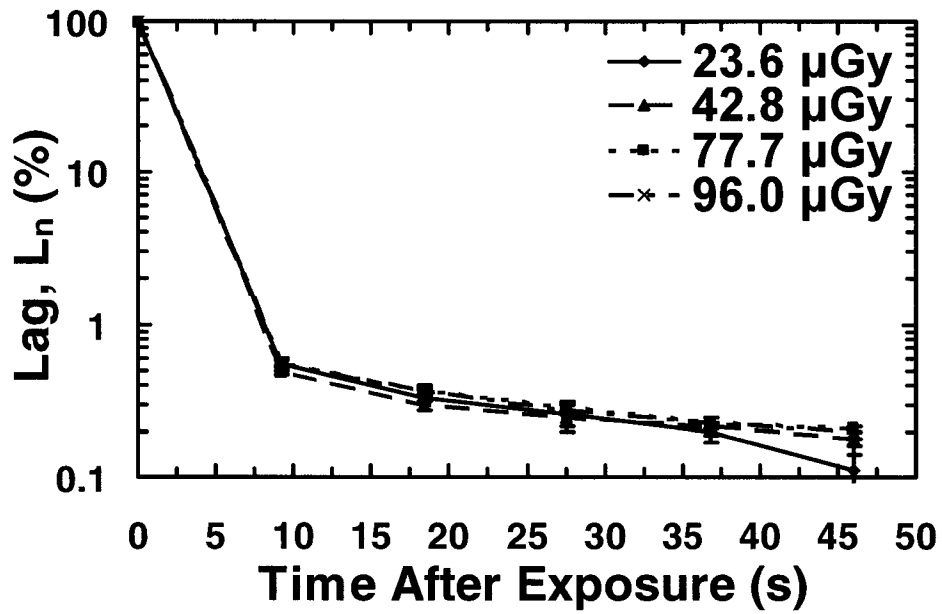


Fig. 4.19: Experimental lag values as a function of time after exposure for 81 kVp, 9.2 s/frame, and four air-kerma values (exposure times of 1.6, 3.2, 6.4 and 8.0 ms respectively).

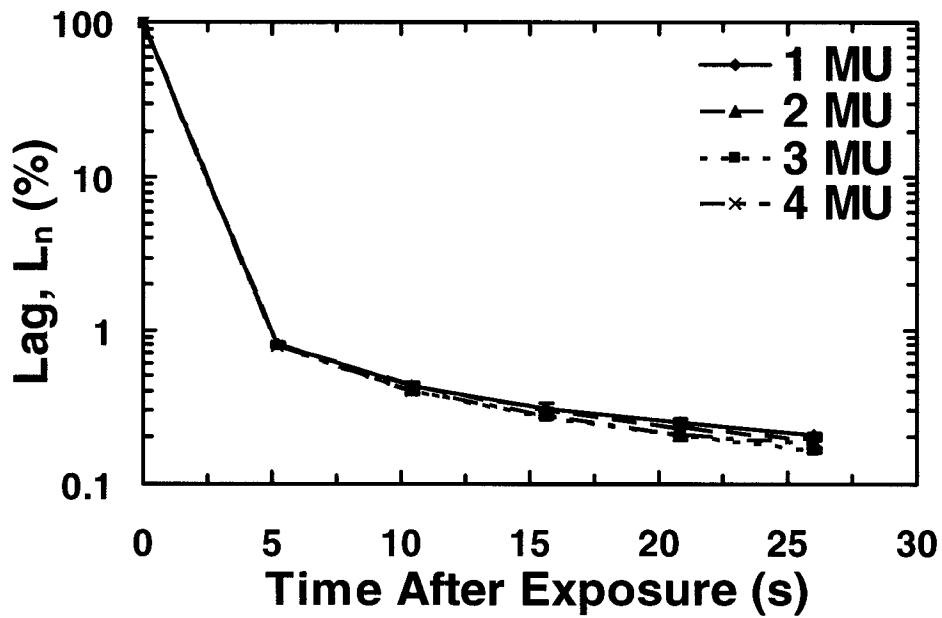


Fig. 4.20: Experimental lag values as a function of time after exposure for 6 MV, 5.2 s/frame, and four different amounts of radiation (250 MU/min).

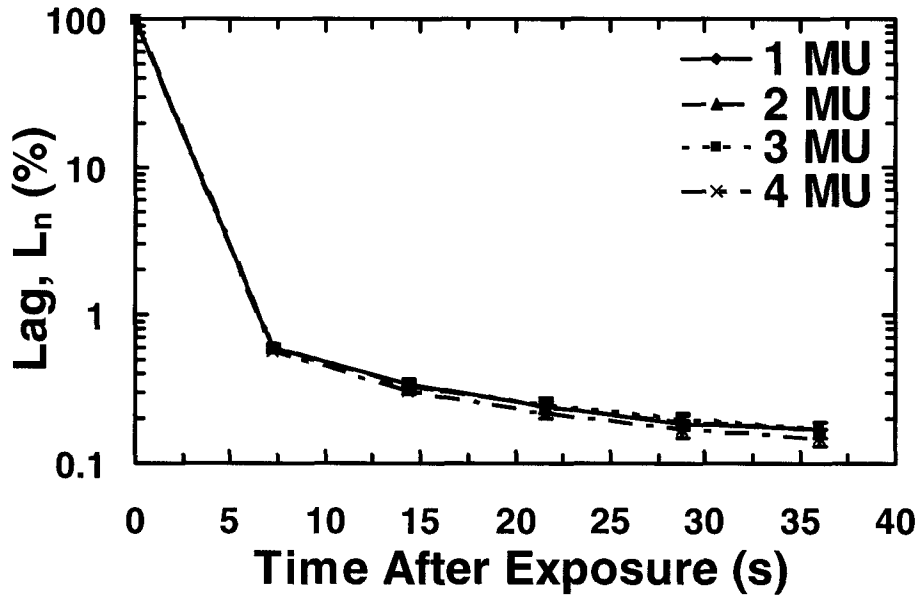


Fig. 4.21: Experimental lag values as a function of time after exposure for 6 MV, 7.2 s/frame, and four different amounts of radiation (250 MU/min).

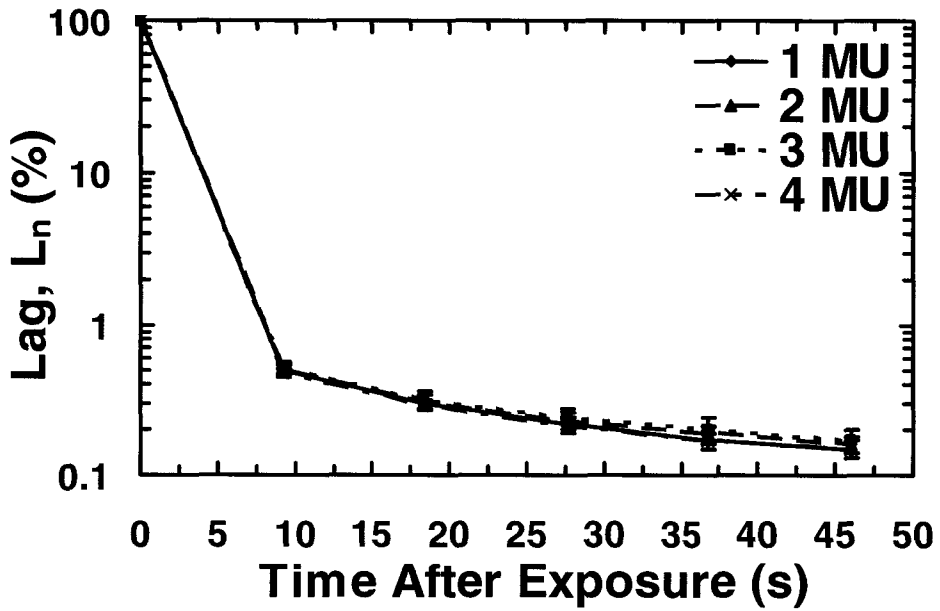


Fig. 4.22: Experimental lag values as a function of time after exposure for 6 MV, 9.2 s/frame, and four different amounts of radiation (250 MU/min).

Figure 4.23 shows " $L_n$ " values as a function of time after exposure for three x-ray beam energies (81 kVp, 125 kVp and 6 MV). An air-kerma exposure of 96.0  $\mu$ Gy was used for the two low energies and 4 MU irradiation was used for the 6 MV photon beam. The results for the frame times of 5.2 s/frame (see Fig. 4.24) and 7.2 s/frame (see Fig. 4.25) are similar. The lag is slightly lower for the MV photon beam. This dependence can be explained as follows. The lower energy photons deposit more energy in the upper layers of a-Se than the lower layers. As mentioned before, this particular detector is biased such that the pixel electrode collects electrons. The larger number of electrons that are generated in the upper layers of a-Se, must travel a larger distance to the pixel electrode and, thus, have a higher probability of being trapped. For 6 MV photons, the energy is deposited more or less uniformly in the a-Se layer. Therefore, in a relative sense, the concentration gradient of created electrons along the depth of the a-Se layer does not exist and relatively lower numbers of electrons are trapped. These results and the above explanation agree with the sensitivity reduction data and explanation thereof from Steciw<sup>2</sup> *et al.* They explain that the farther the electrons have to travel within the a-Se bulk the more likely they are to be trapped. This results in a higher rate of bulk space charging that reduces the detector's sensitivity to a greater degree. Because the system that Steciw *et al.* used collects the electrons at the top electrode, they see a reduction in sensitivity with an increase in photon beam energy.

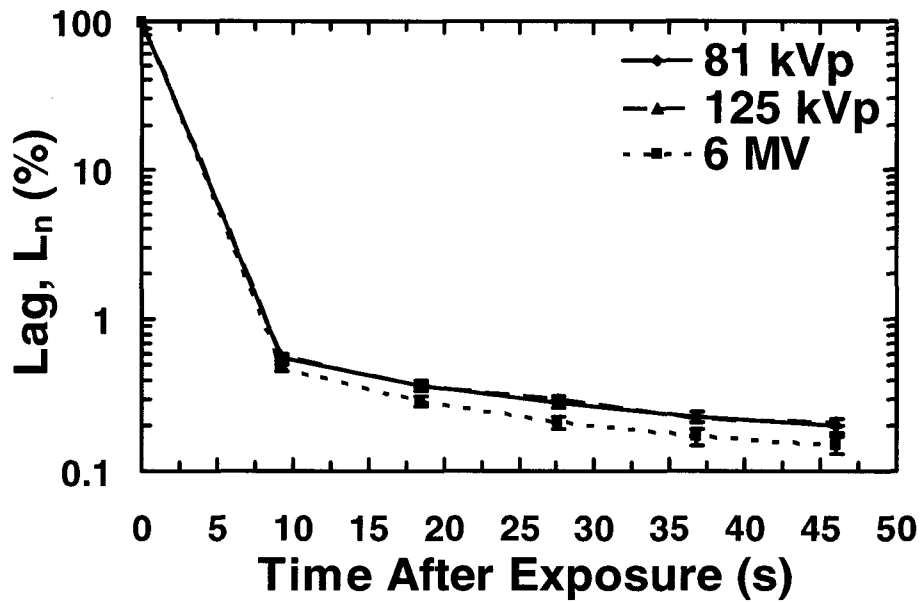


Fig. 4.23: Experimental lag values as a function of time after exposure for 9.2 s/frame, 96.0  $\mu\text{Gy}$  for 81 (exposure time of 8.0 ms) and 125 kVp (exposure time of 4.0 ms) and irradiation of 4 MU (250 MU/min) for 6 MV photons.

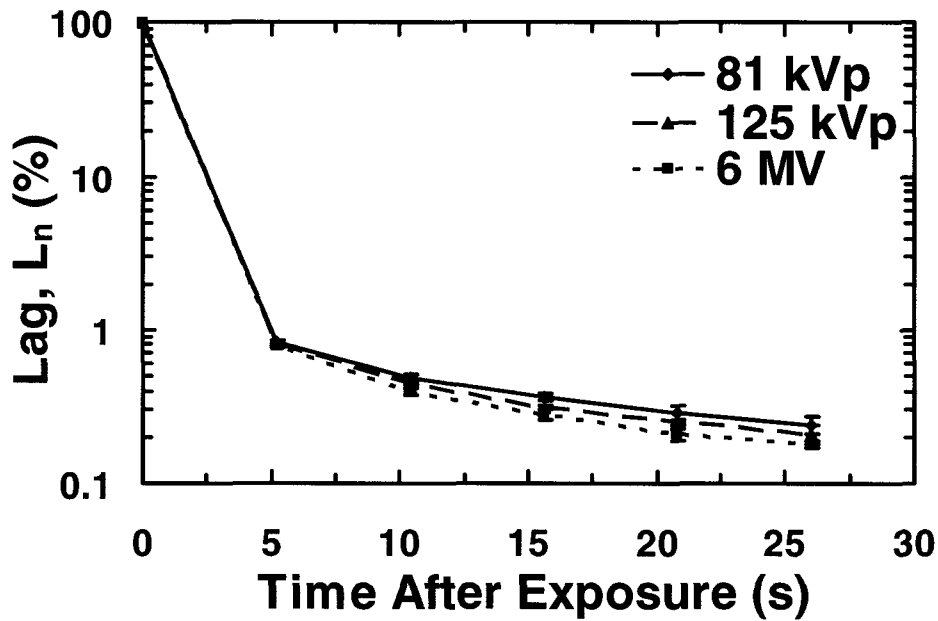


Fig. 4.24: Experimental lag values as a function of time after exposure for 5.2 s/frame, 96.0  $\mu\text{Gy}$  for 81 (exposure time of 8.0 ms) and 125 kVp (exposure time of 4.0 ms) and irradiation of 4 MU (250 MU/min) for 6 MV photons.



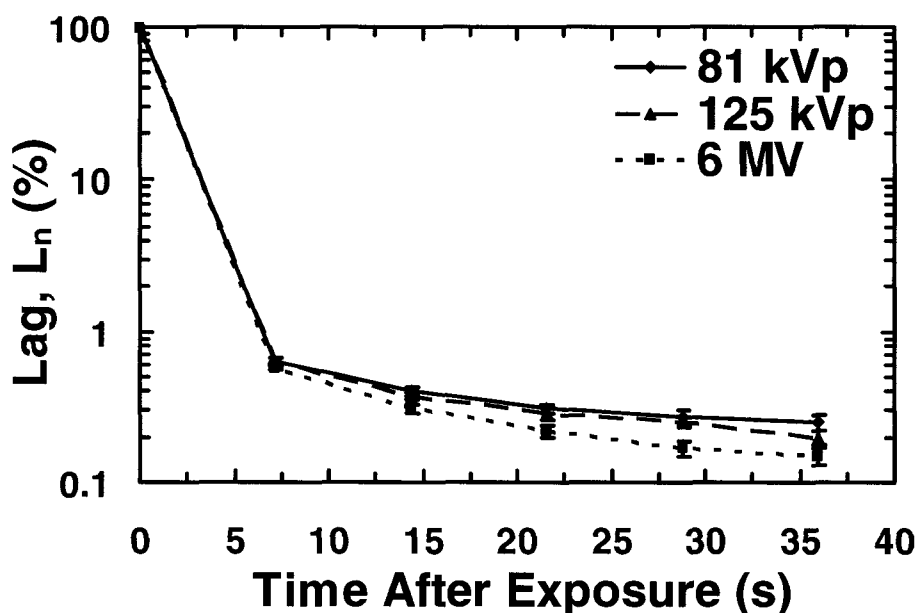
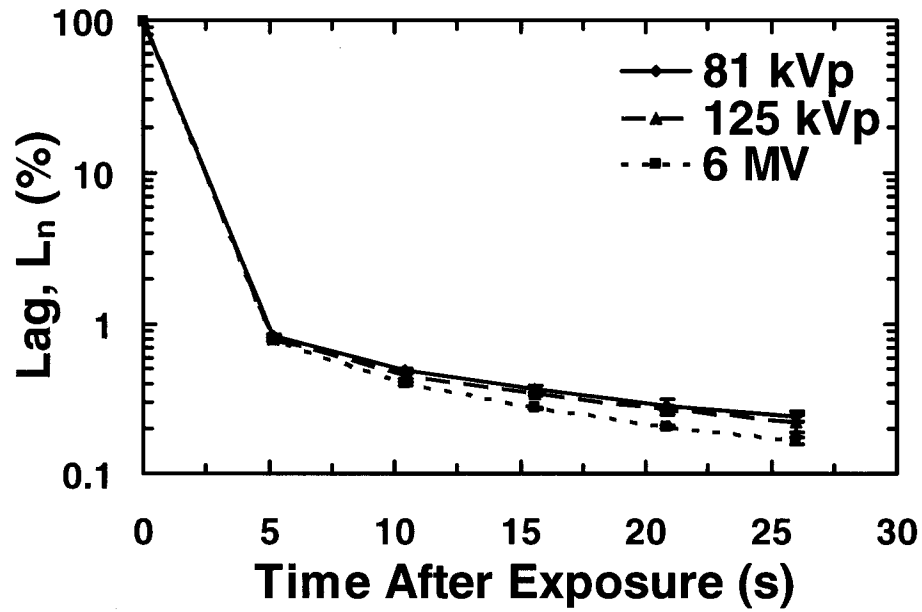


Fig. 4.25: Experimental lag values as a function of time after exposure for 7.2 s/frame, 96.0  $\mu\text{Gy}$  for 81 (exposure time of 8.0 ms) and 125 kVp (exposure time of 4.0 ms) and irradiation of 4 MU (250 MU/min) for 6 MV photons.

Figures 4.26 – 4.28 illustrate the results of energy dependence on the " $L_n$ " values for the three x-ray beam energies (81 kVp, 125 kVp and 6 MV) where an air-kerma exposure of 77.7  $\mu\text{Gy}$  was used for the two low energies and 3 MU irradiation was used for the 6 MV photon beam. Similar results are shown in Figs. 4.29 – 4.31 (where an air-kerma exposure of 42.8  $\mu\text{Gy}$  was used for the two low energies and 2 MU irradiation was used for the 6 MV photon beam) and in Figs. 4.32 – 4.34 (where an air-kerma exposure of 23.6  $\mu\text{Gy}$  was used for the two low energies and 1 MU irradiation was used for the 6 MV photon beam). Some of the above mentioned figures have the 6 MV data points closer to the two sets of diagnostic energy data points, often with an overlap of error bars (see Fig. 4.31). In other figures the different energy curves cross over each other (see

Figs. 4.33 and 4.34) or lie on top of another curve (see Fig. 4.28). These discrepancies are due to experimental uncertainties.



*Fig. 4.26:* Experimental lag values as a function of time after exposure for 5.2 s/frame, 77.7  $\mu\text{Gy}$  for 81 (exposure time of 6.4 ms) and 125 kVp (exposure time of 2.5 ms) and irradiation of 3 MU (250 MU/min) for 6 MV photons.

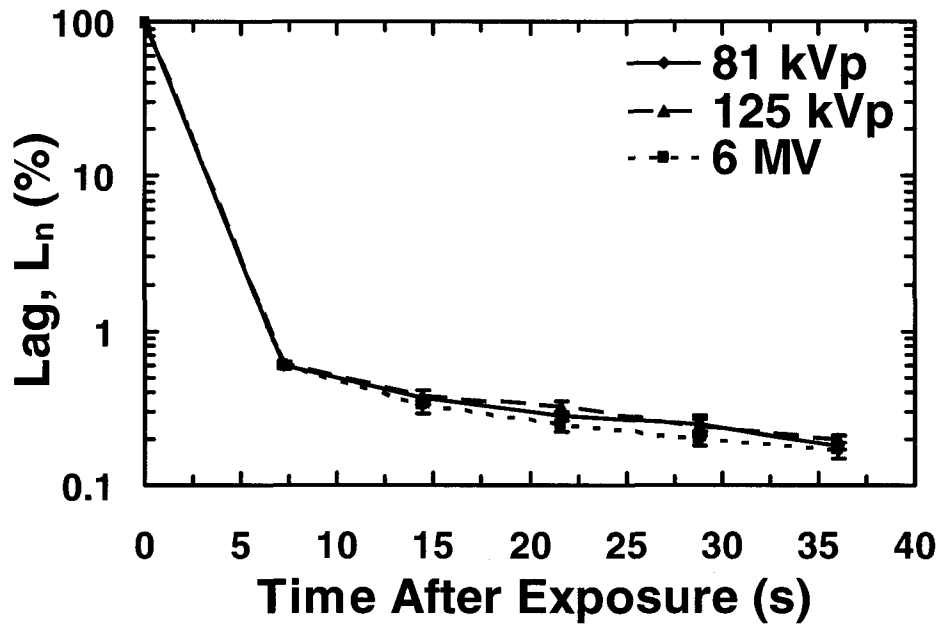


Fig. 4.27: Experimental lag values as a function of time after exposure for 7.2 s/frame, 77.7  $\mu$ Gy for 81 (exposure time of 6.4 ms) and 125 kVp (exposure time of 2.5 ms) and irradiation of 3 MU (250 MU/min) for 6 MV photons.

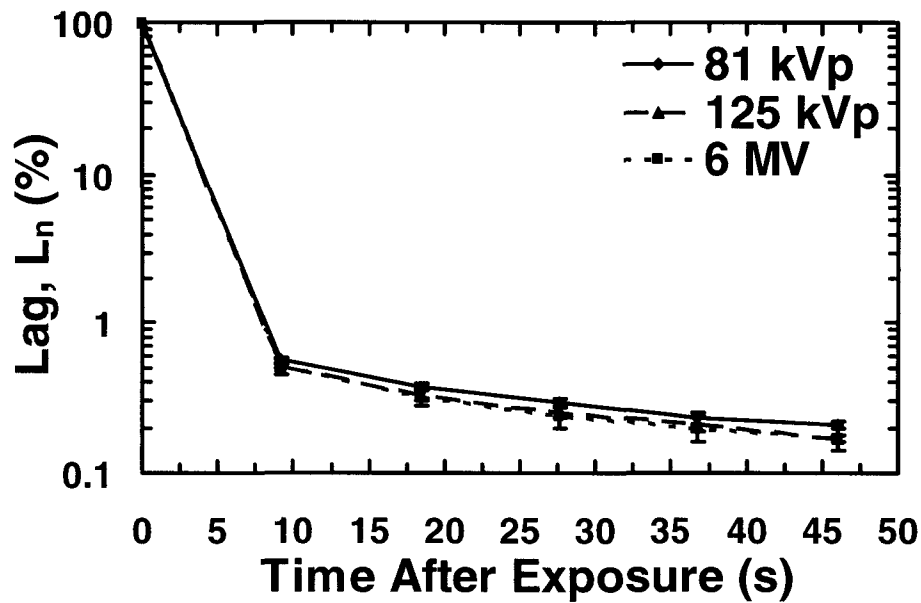


Fig. 4.28: Experimental lag values as a function of time after exposure for 9.2 s/frame, 77.7  $\mu$ Gy for 81 (exposure time of 6.4 ms) and 125 kVp (exposure time of 2.5 ms) and irradiation of 3 MU (250 MU/min) for 6 MV photons.

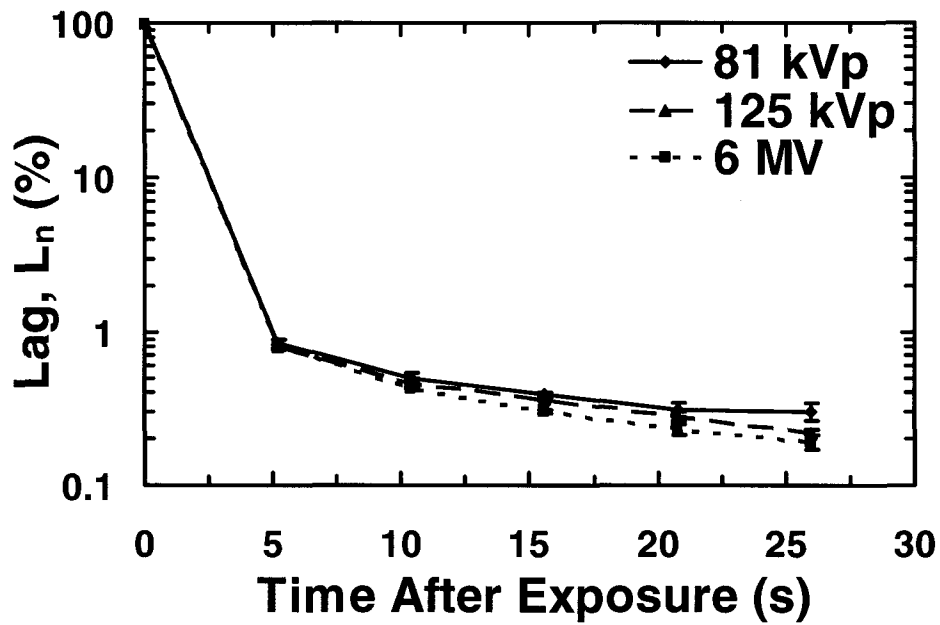


Fig. 4.29: Experimental lag values as a function of time after exposure for 5.2 s/frame, 42.8  $\mu$ Gy for 81 (exposure time of 3.2 ms) and 125 kVp (exposure time of 2.5 ms) and irradiation of 2 MU (250 MU/min) for 6 MV photons.

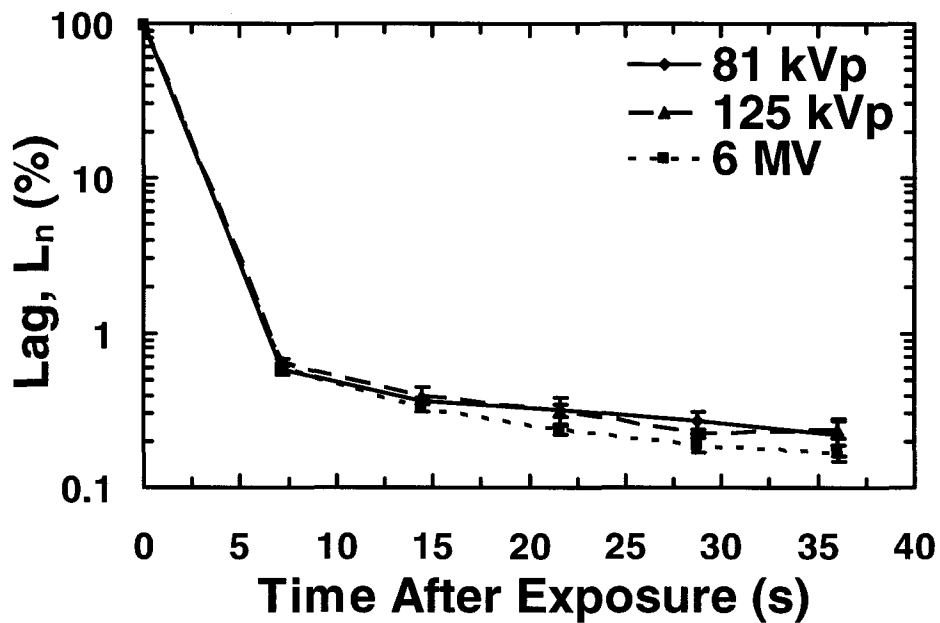


Fig. 4.30: Experimental lag values as a function of time after exposure for 7.2 s/frame, 42.8  $\mu$ Gy for 81 (exposure time of 3.2 ms) and 125 kVp (exposure time of 2.5 ms) and irradiation of 2 MU (250 MU/min) for 6 MV photons.

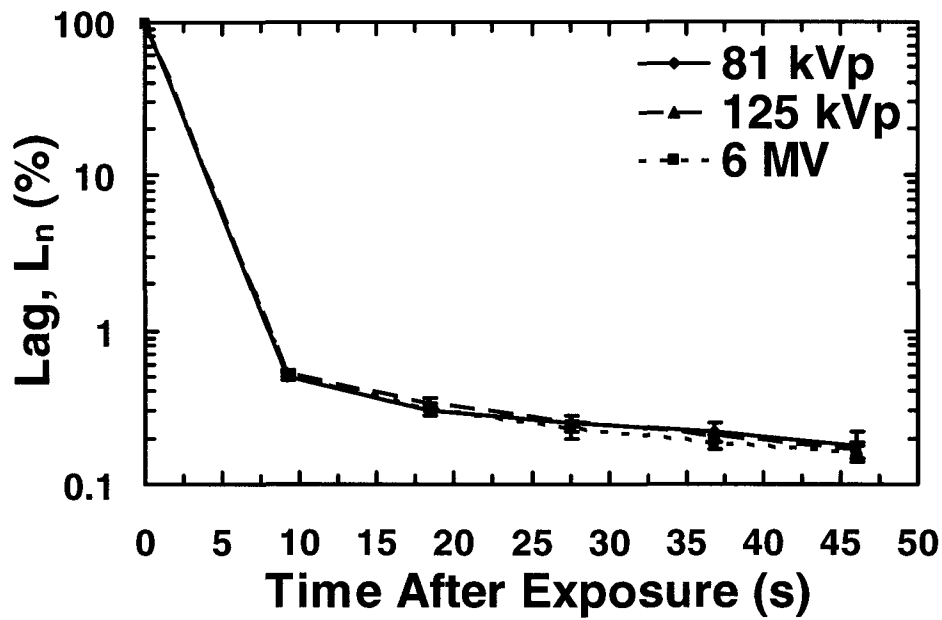


Fig. 4.31: Experimental lag values as a function of time after exposure for 9.2 s/frame, 42.8  $\mu\text{Gy}$  for 81 (exposure time of 3.2 ms) and 125 kVp (exposure time of 2.5 ms) and irradiation of 2 MU (250 MU/min) for 6 MV photons.

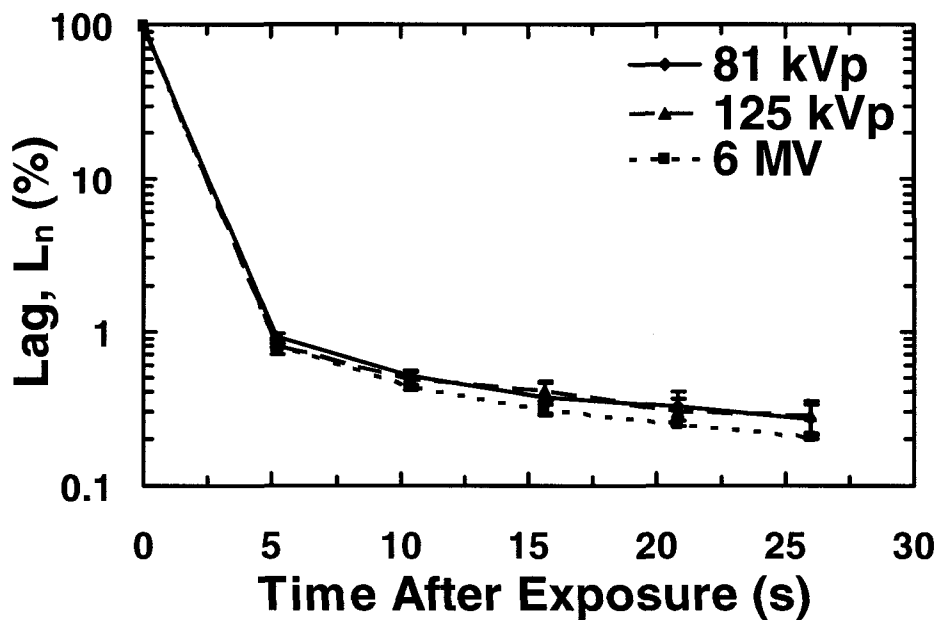


Fig. 4.32: Experimental lag values as a function of time after exposure for 5.2 s/frame, 23.6  $\mu\text{Gy}$  for 81 (exposure time of 1.6 ms) and 125 kVp (exposure time of 2.5 ms) and irradiation of 1 MU (250 MU/min) for 6 MV photons.

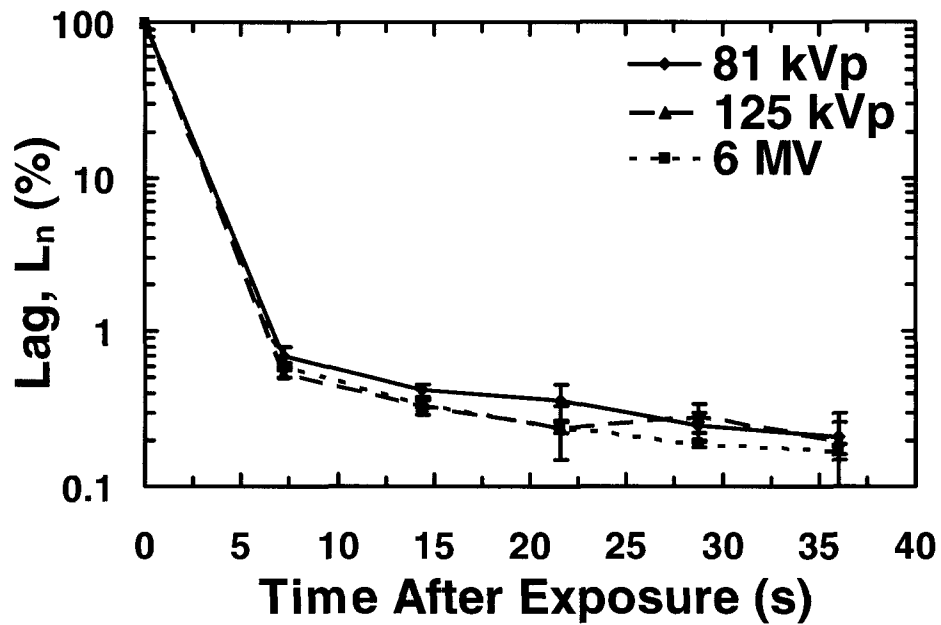


Fig. 4.33: Experimental lag values as a function of time after exposure for 7.2 s/frame, 23.6  $\mu\text{Gy}$  for 81 (exposure time of 1.6 ms) and 125 kVp (exposure time of 2.5 ms) and irradiation of 1 MU (250 MU/min) for 6 MV photons.

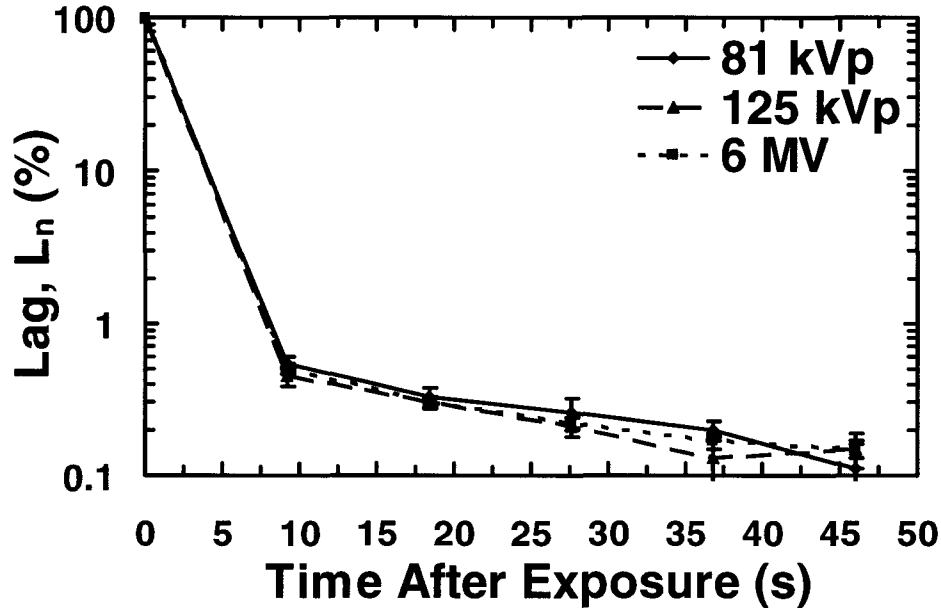


Fig. 4.34: Experimental lag values as a function of time after exposure for 9.2 s/frame, 23.6  $\mu\text{Gy}$  for 81 (exposure time of 1.6 ms) and 125 kVp (exposure time of 2.5 ms) and irradiation of 1 MU (250 MU/min) for 6 MV photons.

Table 4.1: Minimum and Maximum lag values ( $L_n$ ) for the three energies of 81 kVp, 125 kVp and 6 MV. The corresponding frame times and irradiation quantity are listed as well.

Peak X-ray Beam Energy	$L_1$ Minimum 9.2 s/frame (%)	$L_1$ Maximum 5.2 s/frame (%)	$L_2$ Minimum 9.2 s/frame (%)	$L_2$ Maximum 5.2 s/frame (%)
<b>81 kVp</b>	0.50 +/- 0.03 (42.8 $\mu$ Gy)	0.91 +/- 0.05 (23.6 $\mu$ Gy)	0.30 +/- 0.02 (42.8 $\mu$ Gy)	0.51 +/- 0.02 (23.6 $\mu$ Gy)
<b>125 kVp</b>	0.45 +/- 0.06 (23.6 $\mu$ Gy)	0.8 +/- 0.1 (23.6 $\mu$ Gy)	0.30 +/- 0.03 (23.6 $\mu$ Gy)	0.48 +/- 0.07 (23.6 $\mu$ Gy)
<b>6 MV</b>	0.48 +/- 0.03 (4 MU)	0.81 +/- 0.02 (2 MU)	0.29 +/- 0.02 (4 MU)	0.43 +/- 0.02 (1 MU)

All of our measured lag values (see Table 4.1) are below 1.0 %, which is significantly lower than the values ranging from 2 to 10 % reported for indirect AMFPIs.<sup>1</sup> For an explicit comparison with an hydrogenated amorphous silicon (a-Si:H) indirect conversion AMFPI, Siewerdsen<sup>1</sup> *et al.* report a lag value for frame  $n=1$  of (3.78 +/- 0.28) % for a x-ray beam energy of 120 kVp, a frame time of 6.4 s/frame and approximately 2 mR (17.5  $\mu$ Gy) of incident radiation. This is to be compared with our result of  $L_1 = (0.53 +/- 0.03)$  % for similar experimental parameters (125 kVp, 7.2 s/frame, 2.7 mR (23.6  $\mu$ Gy)). This decrease in lag of direct detectors is possibly due to the fact that the photons are converted directly to electronic charge without the necessity of a phosphor layer that converts x-rays to light before the electronic charge is created. The trapping within the a-Si:H photodiode in the indirect AMFPI may be significantly larger than the trapping in the a-Se layer used in the direct AMFPI. This may explain the larger lag values reported.

Our lag measurement results are compared with the lag measurement results of Polischuk<sup>3</sup> *et al.* and Tsukamoto<sup>4</sup> *et al.* Both of these laboratories use a-Se flat-panel

detectors. However, due to incomplete information, direct comparison between these two imaging systems and our system is very difficult. Polischuk<sup>3</sup> *et al.* report lag measurements for a-Se thicknesses of 500 and 1000  $\mu\text{m}$  (Table 4.2). These particular a-Se layers were suitably alloyed such that the electronic transport properties were optimized. The mean beam energy of 55 keV was used with a total irradiation of 50 mR (435  $\mu\text{Gy}$ ). Although not specified, we speculate that the electric field across the a-Se for their data in Table 4.2 is between 10 and 20 V/ $\mu\text{m}$ . It is, however, clearly stated that both samples are biased at the same electric field.

*Table 4.2:* Approximate lag values ( $L_n$ ) measured by Polischuk<sup>3</sup> *et al.* for the a-Se thicknesses of 500 and 1000  $\mu\text{m}$  (10 to 20 V/ $\mu\text{m}$ ; both samples are biased at the same electric field). The corresponding frame number ( $n$ ) and the time after x-ray irradiation are listed as well. Our data is for 125 kVp x-rays, 5.2 s/frame, 96.0  $\mu\text{Gy}$  (11.0 mR, exposure time of 4.0 ms), 5 V/ $\mu\text{m}$  and an a-Se thickness of 200  $\mu\text{m}$ .

	Polischuk <sup>3</sup> <i>et al.</i> 's data			Our data
$L_n$	Time after X-ray Irradiation (s)	Lag, $L_n$ (%) for 500 $\mu\text{m}$ a-Se Thickness	Lag, $L_n$ (%) for 1000 $\mu\text{m}$ a-Se Thickness	Lag, $L_n$ (%) for 200 $\mu\text{m}$ a-Se Thickness
$L_1$	0.03	0.4	0.3	0.80 +/- 0.01
$L_2$	0.1	0.18	0.13	0.45 +/- 0.01
$L_3$	1	0.03	0.02	0.311 +/- 0.008
$L_4$	10	0.004	0.003	0.25 +/- 0.01

They also provide lag values for different electric field strengths across a 500  $\mu\text{m}$  thick a-Se layer. These are summarized in Table 4.3 where all measurements were taken 0.03 s after the x-ray irradiation for the mean beam energy of 55 keV and a total dose of 50 mR (435  $\mu\text{Gy}$ ) delivered over an exposure time of 0.1 s. The detectors used for these experiments could operate at 30 frames per second (fps).



Table 4.3: Approximate lag values for frame  $n=1$  ( $L_1$ ) measured by Polischuk<sup>3</sup> *et al.* for different electric fields across the 500  $\mu\text{m}$  a-Se layer (0.03 s after x-ray irradiation, 55 keV mean beam energy, 50 mR (435  $\mu\text{Gy}$ ) delivered over 0.1 s).

Electric Field across the A-Se layer ( $\text{V}/\mu\text{m}$ )	Lag, $L_1$ (%)
2	1.32
4	0.75
6	0.60
8	0.55
10	0.43
12	0.41
14	0.38
16	0.40
18	0.38
20	0.40

For comparison purposes, the trends in the data of Polischuk *et al.* are used to match the parameters in our experiments. From Table 4.3, a lag value for 5  $\text{V}/\mu\text{m}$  (a-Se thickness of 500  $\mu\text{m}$ ) was determined to be 0.675 % by linear interpolation. From Table 4.2 the lag for frame  $n=1$  and an a-Se thickness of 1000  $\mu\text{m}$  is 0.3 %. Decreasing the a-Se thickness by half to 500  $\mu\text{m}$  results in an increase in lag by 133 % to a value of 0.4 %. Therefore, assuming linearity, if the a-Se thickness is decreased by half again to 250  $\mu\text{m}$  (which is close to the 200  $\mu\text{m}$  thickness used in our measurements), one would expect the lag to increase by 133 % to a value of 0.9 % for an electric field of 5  $\text{V}/\mu\text{m}$ . This is compared to our reported result of  $L_1 = (0.80 \pm 0.01)$  % for a 200  $\mu\text{m}$  a-Se layer at 5  $\text{V}/\mu\text{m}$ , measured 5.2 s after x-ray exposure. It must be stated that the lag measurement values for frame  $n=1$  of Polischuk *et al.* are measured 0.03 s after the x-ray exposure while ours are measured after 5.2 s because of the frame time available with our system.

Tsukamoto<sup>4</sup> *et al.* have also performed lag measurements in an a-Se flat-panel detector using the same definition of lag as ours (Eq. (3.3)). Their detector comprised a

180 x 180 pixel array with a pixel size of  $224 \times 224 \mu\text{m}^2$ . Each pixel contains a 1.0 pF storage capacitor and a thin film transistor (TFT) switch. The geometric fill factor is 86 %. The holes are collected as the bottom electrodes are negatively biased. The output signal is read out row by row by the TFT gate controllers to charge amplifiers and subsequently digitized using a 14-bit ADC. The results are summarized in Table 4.4 for 80 kVp x-rays, an x-ray tube current of 50 mA, an x-ray pulse width of 4 ms, a frame rate of 30 fps (frame time of 0.033 s/frame) and an x-ray exposure of 1220.34 nC/kg (equivalent to 4.73 mR or 41.3  $\mu\text{Gy}$ ).

*Table 4.4:* Approximate lag values ( $L_n$ ) for frames  $n=1$  to  $n=5$  measured by Tsukamoto<sup>4</sup> *et al.*, for a 500  $\mu\text{m}$  thick a-Se layer with an electric field of 10 V/ $\mu\text{m}$  across the a-Se (80 kVp x-rays, 0.033 s/frame, 4.73 mR (41.3  $\mu\text{Gy}$ ), x-ray pulse width of 4 ms). Our data is for 81 kVp x-rays, 5.2 s/frame, 42.8  $\mu\text{Gy}$  (4.9 mR, exposure time of 3.2 ms), and a 200  $\mu\text{m}$  thick a-Se layer (biased by an applied electric field of 5 V/ $\mu\text{m}$ ).

	<b>Tsukamoto<sup>4</sup> <i>et al.</i>'s data</b>	<b>Our data</b>
$L_n$	<b>Lag, <math>L_n</math> (%)</b>	<b>Lag, <math>L_n</math> (%)</b>
$L_1$	1.45	0.86 +/- 0.04
$L_2$	0.72	0.50 +/- 0.04
$L_3$	0.45	0.39 +/- 0.01
$L_4$	0.31	0.31 +/- 0.03
$L_5$	0.27	0.30 +/- 0.04

It can be seen from Table 4.4 that our lag values are significantly lower than those of Tsukamoto *et al* (without considering the frame time). As with the above comparison to Polischuk *et al.*'s data, when the thickness of the a-Se layer and the applied electric field across the a-Se are taken into consideration, it is expected that our results would be even lower creating more of a discrepancy. Our data is lower than that of Tsukamoto *et al.*'s because of the huge discrepancy between frame times. Differences in the design of

the switching and in the alloys used within the a-Se layer is also a factor in the difference of results. There is insufficient information to make direct comparison of the results between the two a-Se systems.

## 4.2 Ghosting due to Lag

Figure 4.35 shows the contrast index " $C_n$ " for frames  $n=1$  through  $n=5$  with a 6 MV beam at 3 MUs (250 MU/min) of radiation, and three frame times (5.2, 7.2 and 9.2 s per frame). This figure shows that " $C_n$ " decreases as a function of frame number and, for a given frame number, " $C_n$ " decreases for a higher frame time.

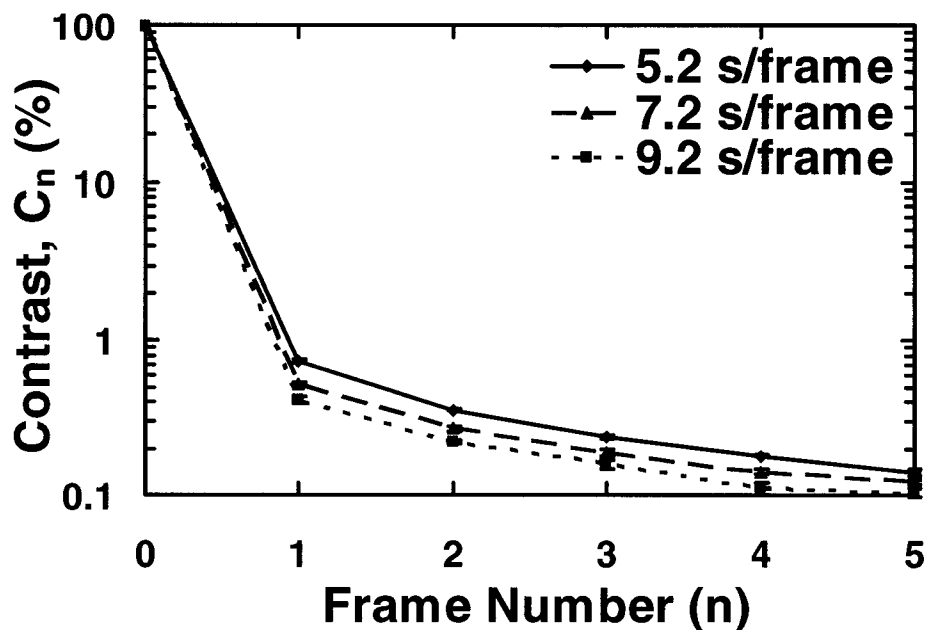


*Fig. 4.35:* Experimental contrast values as a function of frame number after exposure for 6 MV, 3 MU (250 MU/min), and three frame times.

The same data is displayed in Fig. 4.36 as a function of time after exposure (frame number multiplied by frame time). The appearance of the trend in Fig. 4.35 disappears in

Fig. 4.36 where the three series of curves lie on top of each other when plotted as a function of the time after the x-ray exposure. Thus the quantification of ghosting due to lag described by a contrast percentage ( $C_n$ ) decreases with the time after the x-ray exposure irrespective of the frame time. Because contrast in this context is a relative measure of the amount of charge released from the traps, it decreases as a function of time after exposure since the concentration of trapped charges decreases as a function of time. This is similar to our explanation for lag ( $L_n$ ) when plotted as a function of frame number ( $n$ ) and time after x-ray exposure in Figs. 4.1 and 4.2, respectively.

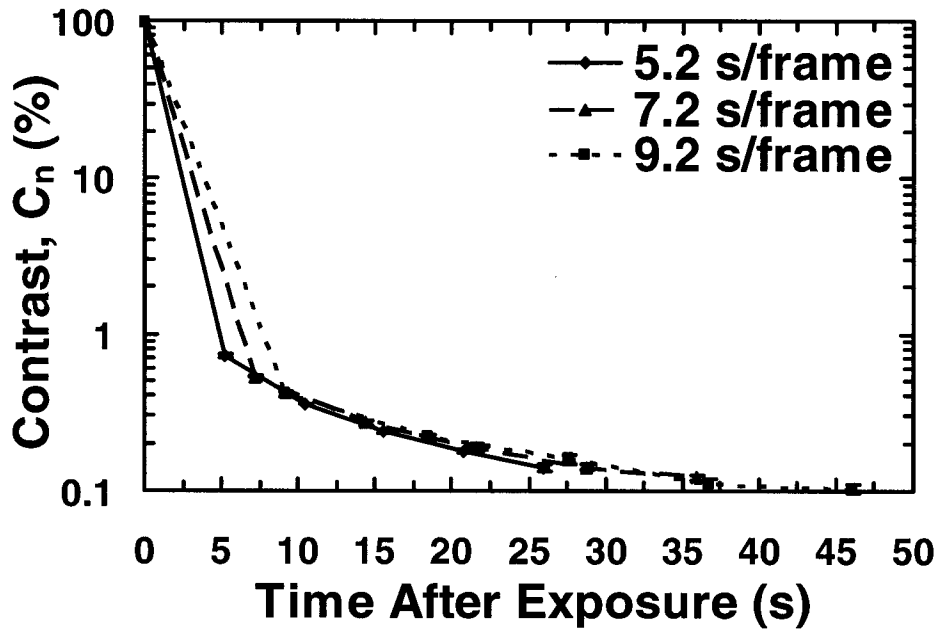


*Fig. 4.36:* Experimental contrast values as a function of time after exposure for 6 MV, 3 MU (250 MU/min), and three frame times.

Similar results are presented in Fig. 4.37 for " $C_n$ " as a function of time after x-ray exposure measured with, now a 125 kVp beam using an air-kerma of 87  $\mu$ Gy (exposure time of 3.0 ms), and the same three frame times (5.2, 7.2 and 9.2 s per frame).

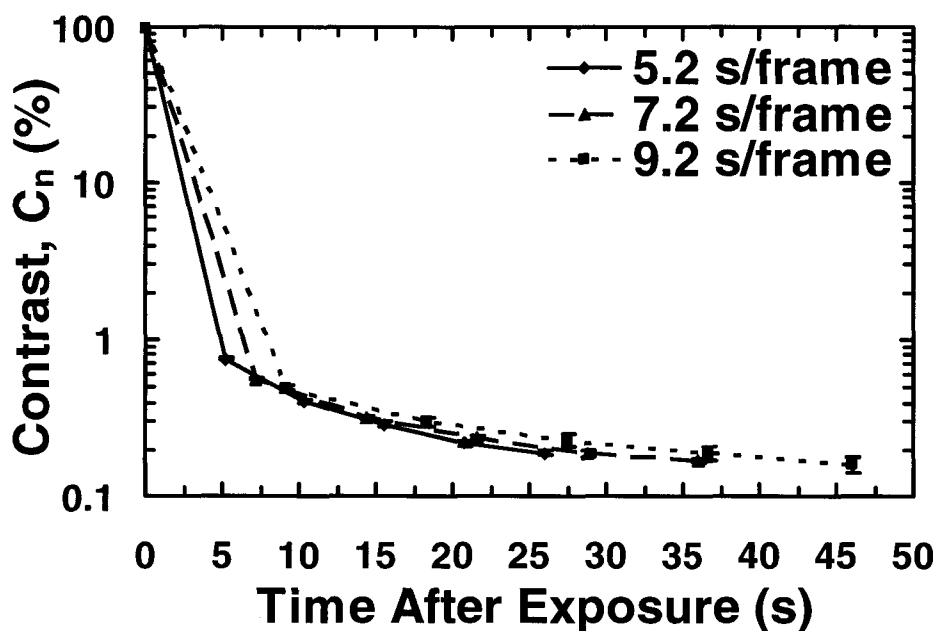


Fig. 4.37: Experimental contrast values as a function of time after exposure for 125 kVp, an air-kerma of 87  $\mu\text{Gy}$  (exposure time of 3.0 ms), and three frame times.

The image contrast, as defined by Eq. (3.4), measured from the images of the high contrast lead phantoms is given in Table 4.5 for 125 kVp and 6 MV photons and for frames  $n=1$  to  $n=2$ .

Table 4.5: Residual contrast ( $C_n$ ) from the ghosting experiments for frames  $n=1$  and  $n=2$  for three frame times.

Peak X-ray Beam Energy	Frame Time (s/frame)	Irradiation Quantity	$C_1$ (%)	$C_2$ (%)
125 kVp	5.2	87 $\mu\text{Gy}$	0.75 +/- 0.01	0.41 +/- 0.01
125 kVp	7.2	87 $\mu\text{Gy}$	0.565 +/- 0.007	0.32 +/- 0.01
125 kVp	9.2	87 $\mu\text{Gy}$	0.49 +/- 0.02	0.30 +/- 0.02
6 MV	5.2	3 MU	0.73 +/- 0.02	0.355 +/- 0.004
6 MV	7.2	3 MU	0.53 +/- 0.01	0.27 +/- 0.01
6 MV	9.2	3 MU	0.41 +/- 0.02	0.219 +/- 0.007

Our quantification of ghosting results are compared with the ghosting results of Polischuk<sup>3</sup> *et al.* and Debie<sup>5</sup> *et al.* Both of these laboratories use a-Se flat-panel detectors. However, due to incomplete information, direct comparison between these two imaging systems and our system is very difficult.

Polischuk<sup>3</sup> *et al.* have documented results for ghosting quantification for a 500  $\mu\text{m}$  thick a-Se detector where the a-Se layers have been suitably alloyed to optimize the electronic transport properties. They investigated the performance of the a-Se detector in a mixed-mode application, i.e. radiographic exposures followed by a fluoroscopic dose rate, by analyzing the ghosting (memory) effects. This can be accomplished by multiple radiographic exposures where the ghosting is quantified immediately afterwards. They used a priming sequence comprised of an initial fluoroscopic dose rate of 140  $\mu\text{R/s}$  (1.22  $\mu\text{Gy/s}$  for approximately 5 s) followed by 25 radiographic pulses of 0.6 mR (5.24  $\mu\text{Gy}$ ) each, where the radiographic pulses were delivered over a total time of approximately 70 s. The mean beam energy of 55 keV was used and the applied electric field was between 10 and 20 V/ $\mu\text{m}$ . The ghost magnitude initially increased and then leveled off at about 9  $\mu\text{R/s}$  (0.079  $\mu\text{Gy/s}$ ) after a cumulative radiographic exposure of approximately 5 mR (43.65  $\mu\text{Gy}$ ). This is equivalent to about 2000 electrons which the authors claim is close to the electronic noise of most read out systems.

Debie<sup>5</sup> *et al.* have also quantified ghosting in a 200  $\mu\text{m}$  thick a-Se flat-panel detector with an applied electric field between 15 and 20 V/ $\mu\text{m}$ . The detector used is the same as the detector we used for the research described in this thesis. A 28 kVp x-ray beam from a mammographic generator with a 0.3 mm focal spot using a molybdenum target was used as a radiation source. A high contrast object was irradiated with an x-ray

exposure of 183 mR (1597.6  $\mu$ Gy) and the image was acquired. A flat field irradiation of 5.8 mR (50.6  $\mu$ Gy) was acquired 30 s later (due to a limitation of the x-ray generator). The display contrast was windowed and leveled to an equivalent 1.6 mR (14.0  $\mu$ Gy) but Debrie *et al.* state that no appreciable ghost could be found. It is questionable whether the display contrast was leveled sufficiently to observe any kind of ghost. If the 1.6 mR (14.0  $\mu$ Gy) is normalized to the initial x-ray exposure of 183 mR (1597.6  $\mu$ Gy) the result is 0.87 %. This is higher than our result for  $C_1$  of 0.75 % from Table 4.5 obtained with different parameters (125 kVp x-rays, 5.2 s/frame, 87  $\mu$ Gy (10 mR, exposure time of 3.0 ms), 200  $\mu$ m of a-Se at 5 V/ $\mu$ m). It would be expected that Debrie *et al.* should have observed lower ghosting than we did due to the use of a higher applied electric field across the a-Se. Perhaps, they should have used sufficiently lower window and leveling to display the ghosting. Further comparison is difficult because they used a multi-exposure method, while we used a single-exposure method.

Figures 4.38 – 4.40 show our " $C_n$ " values as a function of time after exposure for two x-ray beam energies (125 kVp and 6 MV), three frame times (5.2, 7.2 and 9.2 s/frame) and parameters listed in the figure captions. The contrast is slightly lower for the MV photon beam. This dependence can be explained in the same manner as it was for the lag results, i.e. the lower energy photons deposit more energy in the upper layers of a-Se than the lower layers. With this particular detector biased such that the pixel electrodes collect electrons, the larger number of electrons generated in the upper layers of a-Se for the 125 kVp x-ray beam, must travel a larger distance to the pixel electrodes and thus have a higher probability of being trapped. For the 6 MV photon beam, the

energy is deposited more or less uniformly in the a-Se layer (due to the use of the 1.2 mm Cu build-up) resulting in a relatively lower number of electrons being trapped.

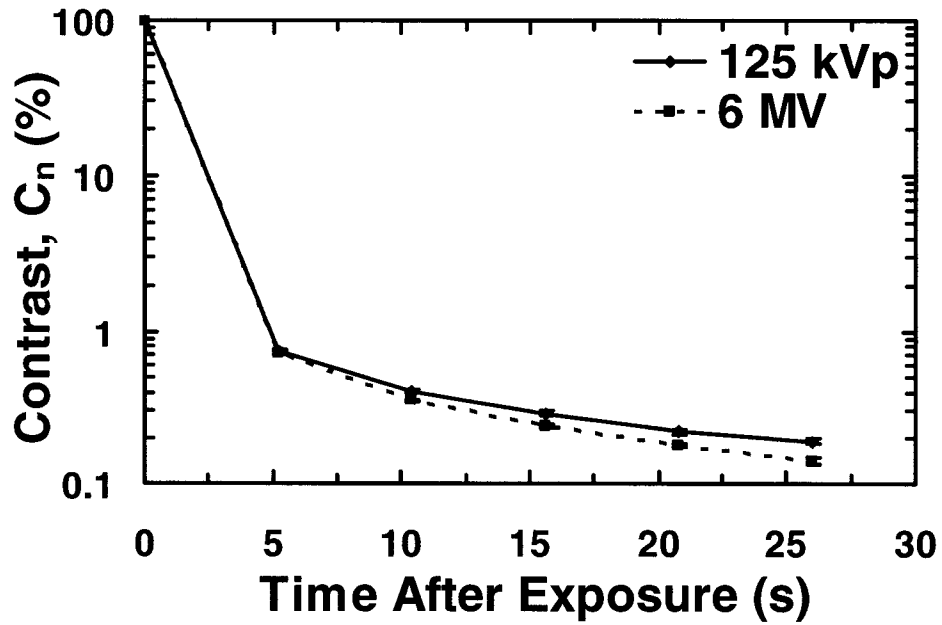


*Fig. 4.38:* Experimental contrast values as a function of time after exposure for 5.2 s/frame, 87  $\mu$ Gy (10 mR, exposure time of 3.0 ms) for 125 kVp and irradiation of 3 MU (250 MU/min) for 6 MV photons.



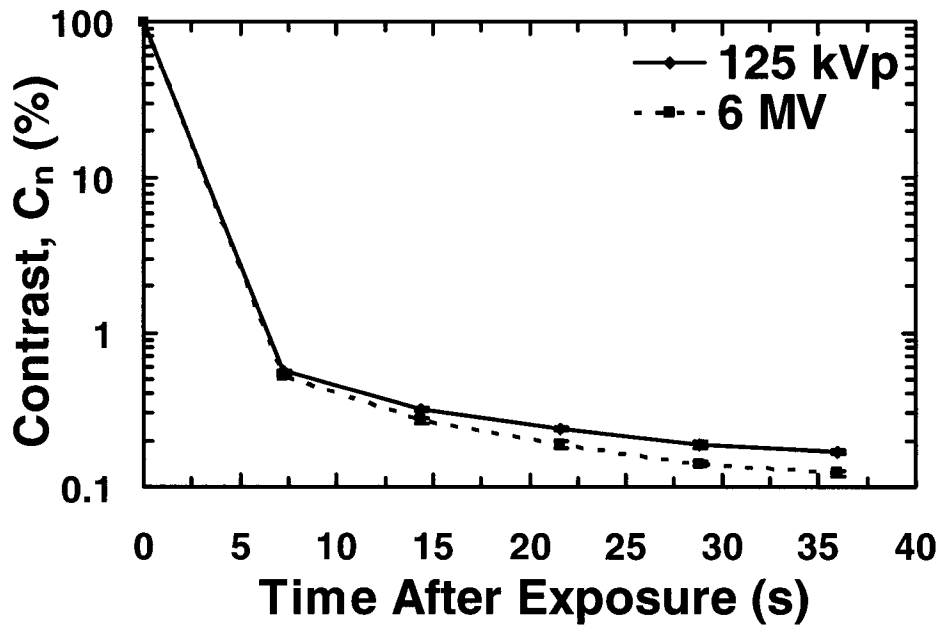


Fig. 4.39: Experimental contrast values as a function of time after exposure for 7.2 s/frame, 87  $\mu$ Gy (10 mR, exposure time of 3.0 ms) for 125 kVp and irradiation of 3 MU (250 MU/min) for 6 MV photons.

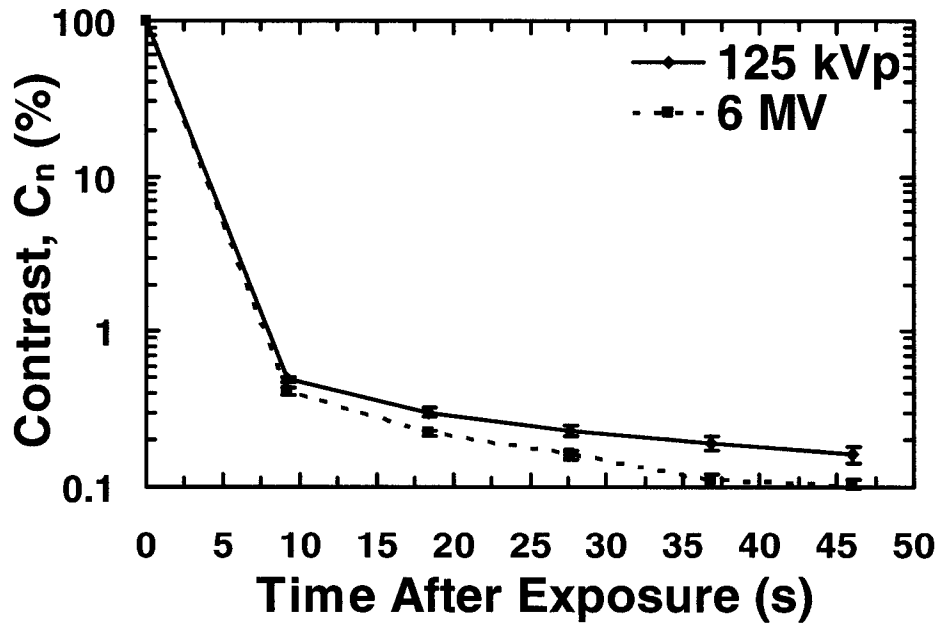
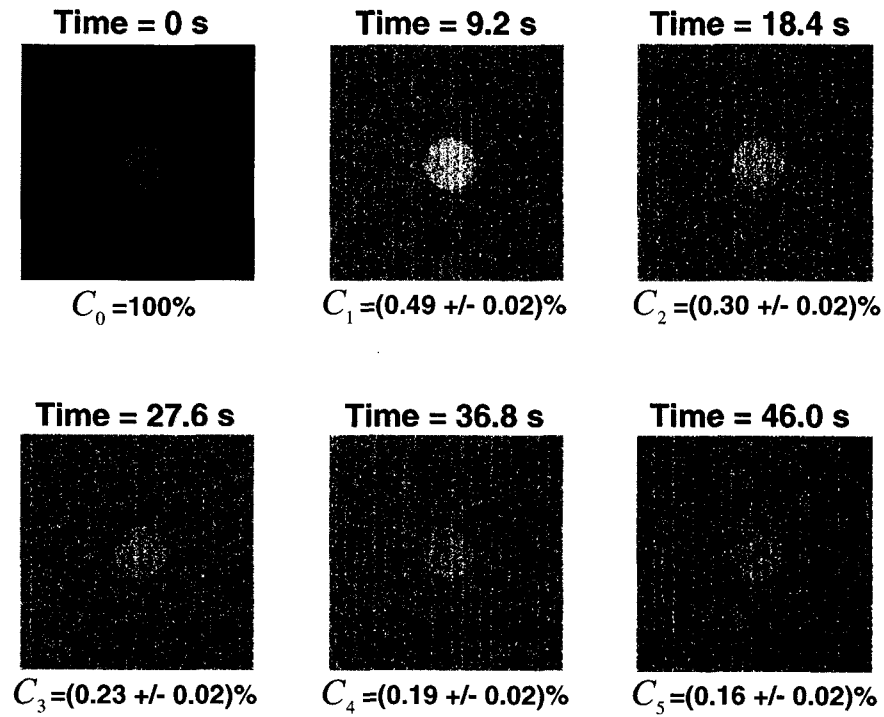
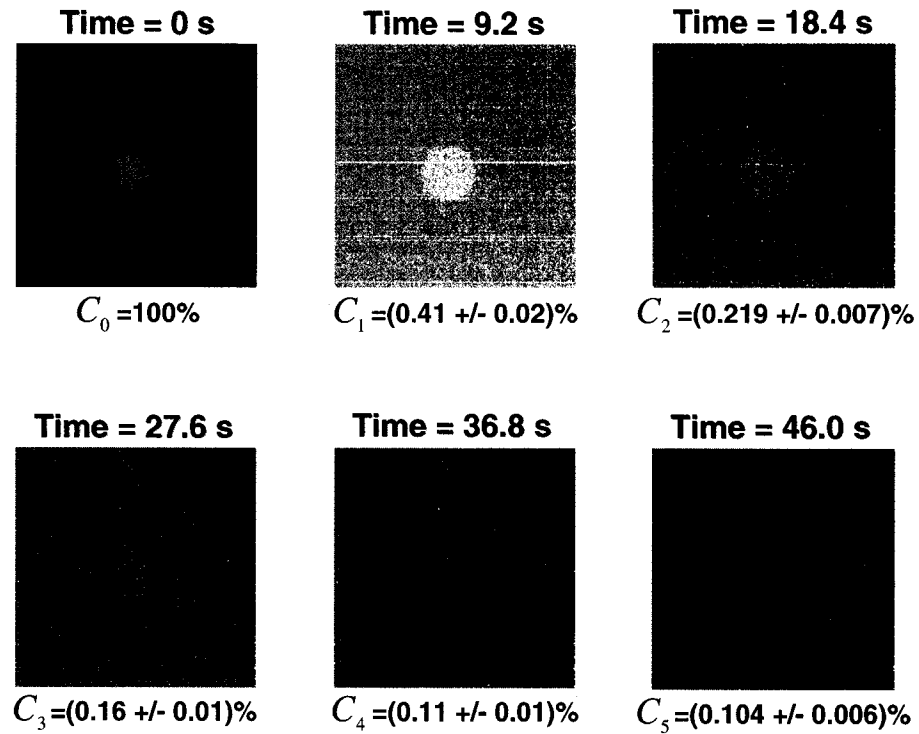


Fig. 4.40: Experimental contrast values as a function of time after exposure for 9.2 s/frame, 87  $\mu$ Gy (10 mR, exposure time of 3.0 ms) for 125 kVp and irradiation of 3 MU (250 MU/min) for 6 MV photons.

Figure 4.41 shows a sequence of corrected images of the high contrast phantom ( $I_{norm}$  in Eq. (3.7)) obtained at several time intervals after exposure for 125 kVp, 9.2 s/frame, and air-kerma of 87  $\mu$ Gy (10 mR, exposure time of 3.0 ms). The residual contrast from Eq. (3.4) is also shown for each image. Figure 4.42 shows a sequence of corrected images of the high contrast phantom ( $I_{norm}$  in Eq. (3.7)) and residual contrast values obtained at several time intervals after exposure for 6 MV, 9.2 s/frame, and irradiation of 3 MU (250 MU/min). These contrast values are significantly lower than those reported for indirect AMFPIs, e.g. a contrast value of approximately 25 % at 1 minute after x-ray exposure for similar experimental parameters (120 kVp, 6.4 s/frame, 87  $\mu$ Gy (10 mR)).<sup>1</sup> This decrease in ghosting of direct detectors is possibly due to the fact that the photons are converted directly to electronic charge without the necessity of a phosphor layer that converts x-rays to light before the electronic charge is created. The trapping within the a-Si:H photodiode in the indirect AMFPI may be significantly larger than the trapping in the a-Se layer used in the direct AMFPI. This may explain the larger ghosting values reported.



*Fig. 4.41:* Sequence of corrected images of the high contrast phantom ( $I_{norm}$  in Eq. (3.7)) obtained at several time intervals after exposure for 125 kVp, 9.2 s/frame, and 87  $\mu$ Gy (10 mR, exposure time of 3.0 ms). The residual contrast as calculated from Eq. (3.4) is also shown for each image.



*Fig. 4.42:* Sequence of corrected images of the high contrast phantom ( $I_{norm}$  in Eq. (3.7)) obtained at several time intervals after exposure for 6 MV, 9.2 s/frame, and 3 MU (250 MU/min). The residual contrast as calculated from Eq. (3.4) is also shown for each image.

### 4.3 Notes

[1] J. H. Siewerdsen and D. A. Jaffray, “A ghost story: Spatio-temporal response characteristics of an indirect-detection flat-panel imager,” *Med. Phys.* **26** (8), 1624-1641 (1999).

[2] S. Steciw, T. Stanescu, S. Rathee, and B. G. Fallone, “Sensitivity reduction in biased amorphous selenium photoconductors,” *J. Phys. D* **35**, 2716-2722 (2002).

- [3] B. Polischuk, Z. Shukri, A. Legros, and H. Rougeot, "Selenium direct converter structure for static and dynamic x-ray detection in medical imaging applications," Proc. SPIE **3336**, 494-504 (1998).
- [4] A. Tsukamoto, S. Yamada, T. Tomisaki, M. Tanaka, T. Sakaguchi, H. Asahina, and M. Nishiki, "Development of a selenium-based flat-panel detector for real-time radiography and fluoroscopy," Proc. SPIE **3336**, 388-395 (1998).
- [5] A. Debie, B. Polischuk, H. Rougeot, M. Hansroul, E. Poliquin, M. Caron, K. Wong, Z. Shukri, and J. Martin, "Quantitative analysis of performance of selenium flat-panel detector for interventional mammography," Proc. SPIE **3977**, 176-184 (2000).

## Chapter 5: Conclusions

The image lag and the ghosting due to lag in an a-Se direct AMFPI have been measured. The  $n=1$  and  $n=2$  frame lag for all energies studied ranges from 0.45 to 0.91 % and from 0.29 to 0.51 %, respectively. It has been shown that lag depends on the time after the x-ray exposure irrespective of the frame time. Because the number of trapped charges increases linearly with the incident energy fluence, the normalized lag values that we measured show no dependence on air-kerma. A possible physical reason for this is the decoupling of the charge detection and storage scheme in our detector. The relative lag values are very slightly lower for megavoltage (MV) photon energies mainly because the electron-hole pairs (EHPs) are generated more uniformly throughout the layers of a-Se while more EHPs are generated in the upper layers at diagnostic energies. The ghosting due to lag for all energies studied ranges from 0.41 to 0.75 % and from 0.219 to 0.41 % for the  $n=1$  and  $n=2$  frame, respectively. Our values for lag and ghosting due to lag are lower than those reported for indirect AMFPIs.

### 5.1 Future Work

Our results will aid in the design of direct AMFPIs for dynamic imaging such as fluoroscopy and CBCT. Any quantitative study using this type of detector should however, consider the effect of lag and ghosting due to lag on the results. Further investigation is needed to explore effects of other limits, including relevant issues such as detector recovery time, potential patient load and long-term photoconductor degeneration, before the clinical use of these systems.

## Bibliography

*The numbers in square brackets indicate the page(s) where the items have been referenced in the thesis.*

M. Abkowitz, "Density of states in a-Se from combined analysis of xerographic potentials and transient transport data," *Philos. Mag. Lett.* **58** (1), 53-57 (1988).  
[p. 33, 34]

P. R. Almond, P. J. Biggs, B. M. Coursey, W. F. Hanson, M. S. Huq, R. Nath, and D. W. O. Rogers, "AAPM's TG-51 protocol for clinical reference dosimetry of high-energy photon and electron beams," *Med. Phys.* **26** (9), 1847-1870 (1999).  
[p. 40]

L. E. Antonuk, Y. El-Mohri, J. H. Siewerdsen, J. Yorkston, W. Huang, V. E. Scarpine, and R. A. Street, "Empirical investigation of the signal performance of a high-resolution, indirect detection, active matrix flat-panel imager (AMFPI) for fluoroscopic and radiographic operation," *Med. Phys.* **24** (1), 51-70 (1997). [p. 3]

J. Beutel, J. M. Fitzpatrick, S. C. Horii, Y. Kim, H. L. Kundel, M. Sonka, and R. L. Van Metter, "Preface," in *Handbook of Medical Imaging, Volume 1: Physics and Psychophysics*, edited by J. Beutel, H. L. Kundel, and R. L. Van Metter (SPIE Press, Bellingham, 2000), pp. xi-xii. [p. 10]

J. Beutel and R. L. Van Metter, "Introduction to Part I," in *Handbook of Medical Imaging, Volume 1: Physics and Psychophysics*, edited by J. Beutel, H. L. Kundel, and R. L. Van Metter (SPIE Press, Bellingham, 2000), pp. xv-xvi. [p. 11]

J. W. Boag, "Xeroradiography," *Phys. Med. Biol.* **18** (1), 3-37 (1973). [p. 13, 15, 20]

A. Brauers, N Conrads, G. Frings, U Schiebel, M. J. Powell, and C. Glasse, "X-ray sensing properties of a lead oxide photoconductor combined with an amorphous silicon TFT array," *Mat. Res. Soc. Symp. Proc.* **507**, 321-326 (1999). [p. 2]

T. J. C. Bruijns, P. L. Alving, E. L. Baker, R. Bury, A. R. Cowen, N. Jung, H. A. Luijendijk, H. J. Meulenbrugge, and H. J. Stouten, "Technical and clinical results of an experimental flat dynamic (digital) x-ray image detector (FDXD) system with real-time corrections," *Proc. SPIE* **3336**, 33-44 (1998). [p. 3, 33]

J. T. Bushberg, J. A. Seibert, E. M. Leidholdt, Jr., and J. M. Boone, *The Essential Physics of Medical Imaging*, Second ed. (Lippincott Williams & Wilkins, Philadelphia, 2002). [p. 11, 12, 13]

C. F. Carlson, "Electron photography," U.S. Patent 2221776 (1938). [p. 19, 21]



C. F. Carlson, "Electrophotography," U.S. Patent 2297691 (1939). [p. 20, 21]

C. F. Carlson, "Process for developing an electrostatic image," U.S. Patent 2842456 (1955). [p. 20, 21]

H. P. Chan, K. Doi, S. Galhotra, C. J. Vyborny, H. MacMahon, and P. M. Jokich, "Image feature analysis and computer-aided diagnosis in digital radiography. I. Automated detection of microcalcifications in mammography," *Med Phys* **14** (4), 538-548 (1987). [p. 11]

A. Debie, B. Polischuk, H. Rougeot, M. Hansroul, E. Poliquin, M. Caron, K. Wong, Z. Shukri, and J. Martin, "Quantitative analysis of performance of selenium flat-panel detector for interventional mammography," *Proc. SPIE* **3977**, 176-184 (2000). [p. 28, 29, 31, 87]

T. Falco, H. Wang, and B. G. Fallone, "Preliminary study of a metal/a-Se-based portal detector," *Med Phys* **25** (6), 814-823 (1998). [p. 21]

P. P. Fatouros and G. U. V. Rao, "Ch. 19: Xeroradiography and electron radiography," in *The Physical Basis of Medical Imaging*, edited by C. M. Coulam, J. J. Erickson, F. D. Rollo, and A. E. James, Jr. (Appleton-Century-Crofts, New York, 1981), pp. 265-277. [p. 20]

M. L. Giger, N. Ahn, K. Doi, H. MacMahon, and C. E. Metz, "Computerized detection of pulmonary nodules in digital chest images: Use of morphological filters in reducing false-positive detections," *Med Phys* **17** (5), 861-865 (1990). [p. 11]

P. R. Granfors, "Performance characteristics of an amorphous silicon flat panel x-ray imaging detector," *Proc. SPIE* **3659**, 480-490 (1999). [p. 3, 33]

P. B. Greer and C. C. Popescu, "Dosimetric properties of an amorphous silicon electronic portal imaging device for verification of dynamic intensity modulated radiation therapy," *Med. Phys.* **30** (7), 1618-1627 (2003). [p. 3]

[http://www.chemsoc.org/viselements/pages/data/selenium\\_data.html](http://www.chemsoc.org/viselements/pages/data/selenium_data.html). [p. 15]

L. S. Jeromin and H. L. Hoyt, III, "Development apparatus for latent electrostatic images," U.S. Patent 3640246 (1969). [p. 21]

L. S. Jeromin and L. M. Klynn, "Electronic recording of x-ray images," *J. Appl. Photo. Engin.* **5**, 183-189 (1979). [p. 13]

H. E. Johns and J. R. Cunningham, *The Physics of Radiology*, Fourth ed. (Charles C Thomas, Springfield, 1983). [p. 18, 38]

N. Jung, P. L. Alving, F. Busse, N. Conrads, H. M. Meulenbrugge, W. Rütten, U. Schiebel, M. Weibrecht, and H. Wiczorek, "Dynamic x-ray imaging system based on an amorphous silicon thin-film array," Proc. SPIE **3336**, 396-407 (1998). [p. 3, 33]

J. Kalade, E. Montrimas, and J. Rakauskas, "The mechanism of sensitivity reduction in selenium layers irradiated by x-rays," Phys. Stat. Sol. A **25**, 629-636 (1974). [p. 35]

C. A. Klein, "Band gap dependence and related features of radiation ionization energies in semiconductors," J. Appl. Phys. **39**, 2029-2038 (1968). [p. 16]

M. Lachaîne and B. G. Fallone, "Calculation of inelastic cross-sections for the interaction of electrons with amorphous selenium," J. Phys. D: Appl. Phys. **33**, 551-555 (2000). [p. 16]

M. Lachaîne and B. G. Fallone, "Monte Carlo simulations of x-ray induced recombination in amorphous selenium," J. Phys. D: Appl. Phys. **33**, 1417-1423 (2000). [p. 17, 18]

M. Lachaîne and B. G. Fallone, "Design considerations for direct and indirect active matrix flat-panel portal imagers," Radiol. Oncol. **35** (1), 63-71 (2001). [p. 3]

M. Lachaine, E. Fourkal, and B. G. Fallone, "Detective quantum efficiency of a direct-detection active matrix flat panel imager at megavoltage energies," *Med. Phys.* **28** (7), 1364-1372 (2001). [p. 3, 28]

M. Lachaine, E. Fourkal, and B. G. Fallone, "Investigation into the physical characteristics of active matrix flat panel imagers for radiotherapy," *Med. Phys.* **28** (8), 1689-1695 (2001). [p. 3, 29, 32]

D. L. Lee, L. K. Cheung, and L. S. Jeromin, "A new digital detector for projection radiography," *Proc. SPIE* **2432**, 237-249 (1995). [p. 2]

D. L. Lee, L. K. Cheung, B. Rodricks, and G. F. Powell, "Improved imaging performance of a 14 x 17-inch Direct Radiography™ System using Se/TFT detector," *Proc. SPIE* **3336**, 14-23 (1998). [p. 3]

R. Luhta and J. A. Rowlands, "Feasibility of a large area x-ray sensitive vidicon for medical fluoroscopy: Resolution and lag factors," *Med Phys* **24** (5), 621-631 (1997). [p. 13]

D. Mah, J. A. Rowlands, and J. A. Rawlinson, "Sensitivity of amorphous selenium to x rays from 40 kVp to 18 MV: Measurements and implications for portal imaging," *Med. Phys.* **25** (4), 444-456 (1998). [p. 3, 18]

J. W. May and A. R. Lubinsky, "High-resolution computed radiography by scanned luminescent toner xeroradiography," Proc. SPIE **1896**, 296-312 (1993). [p. 13]

B. M. C. McCurdy, K. Luchka, and S. Pistorius, "Dosimetric investigation and portal dose image prediction using an amorphous silicon electronic portal imaging device," Med. Phys. **28** (6), 911-924 (2001). [p. 3]

E. A. Montrimas, B. K. Rakauskene, and J. Rakauskas, "Investigation of quantum efficiency of selenium electroradiographic layers," Lietuv. Fiz. Rink. **10**, 941 (1970). [p. 17]

J. Mort, *The Anatomy of Xerography* (McFarland & Company, Jefferson, 1989). [p. 15]

P. Munro and D. C. Bouius, "X-ray quantum limited portal imaging using amorphous silicon flat-panel arrays," Med. Phys. **25** (5), 689-702 (1998). [p. 3]

U. Neitzel, I. Maack, and S. Gunther-Kohfahl, "Image quality of a digital chest radiography system based on a selenium detector," Med Phys **21** (4), 509-516 (1994). [p. 13]

L. Onsager, "Initial recombination of ions," Phys. Rev. **54**, 554-557 (1938). [p. 18]

D. R. Ouimette, S. Nudelman, and R. Aikens, "A new large area x-ray image sensor," Proc. SPIE **3336**, 470-476 (1998). [p. 2]

G. Pang, D. L. Lee, and J. A. Rowlands, "Investigation of a direct conversion flat panel imager for portal imaging," Med. Phys. **28** (10), 2121-2128 (2001). [p. 3]

G. Pang, W. Zhao, and J. A. Rowlands, "Digital radiology using active matrix readout of amorphous selenium: Geometrical and effective fill factors," Med Phys **25** (9), 1636-1646 (1998). [p. 28]

B. Polischuk, H. Rougeot, K. Wong, A. Debie, E. Poliquin, M. Hansroul, J. Martin, T. Truong, M. Choquette, L. Laperrière, and Z. Shukri, "Direct conversion detector for digital mammography," Proc. SPIE **3659**, 417-425 (1999). [p. 3, 29, 30]

B. Polischuk, Z. Shukri, A. Legros, and H. Rougeot, "Selenium direct converter structure for static and dynamic x-ray detection in medical imaging applications," Proc. SPIE **3336**, 494-504 (1998). [p. 33, 80, 81, 82, 87]

W. Que and J. A. Rowlands, "X-ray imaging using amorphous selenium: Inherent spatial resolution," Med Phys **22** (4), 365-374 (1995). [p. 21]

W. Que and J. A. Rowlands, "X-ray photogeneration in amorphous selenium: Geminate versus columnar recombination," *Phys. Rev. B* **51** (16), 10500-10507 (1995). [p. 16, 17]

P. K. Rieppo and J. A. Rowlands, "X-ray imaging with amorphous selenium: Theoretical feasibility of the liquid crystal light valve for radiography," *Med Phys* **24** (8), 1279-1291 (1997). [p. 13]

J. A. Rowlands and S. O. Kasap, "Amorphous semiconductors usher in digital x-ray imaging," *Phys. Today* **50** (11), 24-30 (1997). [p. 33, 35]

J. A. Rowlands and J. Yorkston, "Ch. 4: Flat panel detectors for digital radiography," in *Handbook of Medical Imaging, Volume 1: Physics and Psychophysics*, edited by J. Beutel, H. L. Kundel, and R. L. Van Metter (SPIE Press, Bellingham, 2000), pp. 223-328. [p. 1, 2, 11, 13, 14, 15, 18, 19]

E. Samei and M. J. Flynn, "An experimental comparison of detector performance for direct and indirect digital radiography systems," *Med. Phys.* **30** (4), 608-622 (2003). [p. 3]

R. M. Schaffert, *Electrophotography*, Second ed. (Focal Press Limited, London, 1975). [p. 15]

R. M. Schaffert, R. C. McMaster, and W. E. Bixby, "Electroradiography," U.S. Patent 2666144 (1950). [p. 20, 21]

U. Schiebel, T. Buchkremer, G. Frings, and P. Quadflieg, "Deep trapping and recombination in a-Se:As x-ray sensitive photoreceptors," *J. Non-Cryst. Solids* **115**, 216-218 (1989). [p. 35]

K. S. Shah, P. Bennett, L. Cirignano, Y. Dmitriyev, M. Klugerman, K. Mandel, L. P. Moy, and R. A. Street, "Characterization of x-ray imaging properties of  $\text{PbI}_2$  films," *Mat. Res. Soc. Symp. Proc.* **487**, 351-360 (1998). [p. 2]

K. S. Shah, P. Bennett, M. Klugerman, L. P. Moy, and G. Entine, "Lead iodide films for x-ray imaging," *Proc. SPIE* **3032**, 395-404 (1997). [p. 2]

J. H. Siewerdsen, L. E. Antonuk, Y. El-Mohri, J. Yorkston, W. Huang, J. M. Boudry, and I. A. Cunningham, "Empirical and theoretical investigation of the noise performance of indirect detection, active matrix flat-panel imagers (AMFPIs) for diagnostic radiology," *Med. Phys.* **24** (1), 71-89 (1997). [p. 3]

J. H. Siewerdsen and D. A. Jaffray, "A ghost story: Spatio-temporal response characteristics of an indirect-detection flat-panel imager," *Med. Phys.* **26** (8), 1624-1641 (1999). [p. 3, 33, 36, 40, 63, 80, 91]



J. H. Siewerdsen and D. A. Jaffray, "Cone-beam computed tomography with a flat-panel imager: Effects of image lag," *Med. Phys.* **26** (12), 2635-2647 (1999). [p. 3]

S. Steciw, T. Stanescu, S. Rathee, and B. G. Fallone, "Sensitivity reduction in biased amorphous selenium photoconductors," *J. Phys. D* **35**, 2716-2722 (2002). [p. 35, 72]

M. F. Stone, W. Zhao, B. V. Jacak, P. O'Connor, B. Yu, and P. Rehak, "The x-ray sensitivity of amorphous selenium for mammography," *Med. Phys.* **29** (3), 319-324 (2002). [p. 3]

A. Tsukamoto, S. Yamada, T. Tomisaki, M. Tanaka, T. Sakaguchi, H. Asahina, and M. Nishiki, "Development of a selenium-based flat-panel detector for real-time radiography and fluoroscopy," *Proc. SPIE* **3336**, 388-395 (1998). [p. 33, 80, 82, 83]

S. Vedantham, A. Karellas, S. Suryanarayanan, D. Albagli, S. Han, E. J. Tkaczyk, C. E. Landberg, B. Opsahl-Ong, P. R. Granfors, I. Levis, C. J. D'Orsi, and R. E. Hendrick, "Full breast digital mammography with an amorphous silicon-based flat panel detector: Physical characteristics of a clinical prototype," *Med. Phys.* **27** (3), 558-567 (2000). [p. 3]

R. L. Weisfield, M. Hartney, R. Schneider, K. Aflatooni, and R. Lujan, "High performance amorphous silicon image sensor for x-ray diagnostic medical imaging applications," Proc. SPIE **3659**, 307-317 (1999). [p. 33]

M. J. Yaffe and J. A. Rowlands, "X-ray detectors for digital radiography," Phys. Med. Biol. **42** (1), 1-39 (1997). [p. 12, 14]

W. Zhao, G. DeCrescenzo, and J. A. Rowlands, "Investigation of lag and ghosting in amorphous selenium flat-panel x-ray detectors," Proc. SPIE **4682**, 9-20 (2002). [p. 3, 33, 35]

W. Zhao, W. G. Ji, A. Debie, and J. A. Rowlands, "Imaging performance of amorphous selenium based flat-panel detectors for digital mammography: Characterization of a small area prototype detector," Med. Phys. **30** (2), 254-263 (2003). [p. 3]

W. Zhao and J. A. Rowlands, "A large area solid-state detector for radiology using amorphous selenium," Proc. SPIE **1651**, 134-143 (1992). [p. 2, 3]

W. Zhao and J. A. Rowlands, "X-ray imaging using amorphous selenium: Feasibility of a flat panel self-scanned detector for digital radiology," Med. Phys. **22** (10), 1595-1604 (1995). [p. 3]

## Appendix

*Table A.1:* Complete lag measurement data for 81 kVp x-rays.

Frame Time (s/frame)	Air Kerma ( $\mu\text{Gy}$ )	$L_1$ (%)	$L_2$ (%)	$L_3$ (%)	$L_4$ (%)	$L_5$ (%)
5.2	23.6	0.91 +/- 0.05	0.51 +/- 0.02	0.37 +/- 0.09	0.32 +/- 0.08	0.27 +/- 0.06
5.2	42.8	0.86 +/- 0.04	0.50 +/- 0.04	0.39 +/- 0.01	0.31 +/- 0.03	0.30 +/- 0.04
5.2	77.7	0.84 +/- 0.02	0.49 +/- 0.02	0.37 +/- 0.02	0.28 +/- 0.03	0.24 +/- 0.02
5.2	96.0	0.83 +/- 0.03	0.49 +/- 0.02	0.37 +/- 0.02	0.29 +/- 0.03	0.24 +/- 0.03
7.2	23.6	0.7 +/- 0.1	0.42 +/- 0.04	0.36 +/- 0.09	0.25 +/- 0.05	0.21 +/- 0.05
7.2	42.8	0.59 +/- 0.04	0.37 +/- 0.02	0.32 +/- 0.03	0.27 +/- 0.04	0.22 +/- 0.06
7.2	77.7	0.60 +/- 0.02	0.37 +/- 0.04	0.28 +/- 0.02	0.25 +/- 0.03	0.18 +/- 0.01
7.2	96.0	0.64 +/- 0.03	0.40 +/- 0.03	0.31 +/- 0.02	0.27 +/- 0.03	0.25 +/- 0.03
9.2	23.6	0.55 +/- 0.05	0.33 +/- 0.05	0.26 +/- 0.06	0.20 +/- 0.03	0.11 +/- 0.05
9.2	42.8	0.50 +/- 0.03	0.30 +/- 0.02	0.25 +/- 0.03	0.22 +/- 0.03	0.18 +/- 0.04
9.2	77.7	0.56 +/- 0.02	0.37 +/- 0.02	0.29 +/- 0.02	0.23 +/- 0.02	0.21 +/- 0.01
9.2	96.0	0.56 +/- 0.02	0.37 +/- 0.03	0.28 +/- 0.02	0.23 +/- 0.02	0.20 +/- 0.02

*Table A.2:* Complete lag measurement data for 125 kVp x-rays.

Frame Time (s/frame)	Air Kerma ( $\mu\text{Gy}$ )	$L_1$ (%)	$L_2$ (%)	$L_3$ (%)	$L_4$ (%)	$L_5$ (%)
5.2	23.6	0.8 +/- 0.1	0.48 +/- 0.07	0.41 +/- 0.06	0.30 +/- 0.06	0.28 +/- 0.07
5.2	42.8	0.80 +/- 0.04	0.46 +/- 0.04	0.36 +/- 0.01	0.28 +/- 0.02	0.22 +/- 0.01
5.2	77.7	0.80 +/- 0.03	0.45 +/- 0.02	0.34 +/- 0.01	0.27 +/- 0.01	0.22 +/- 0.03
5.2	96.0	0.80 +/- 0.01	0.45 +/- 0.01	0.311 +/- 0.008	0.25 +/- 0.01	0.21 +/- 0.03
7.2	23.6	0.53 +/- 0.03	0.33 +/- 0.04	0.24 +/- 0.09	0.28 +/- 0.06	0.2 +/- 0.1
7.2	42.8	0.66 +/- 0.03	0.40 +/- 0.05	0.32 +/- 0.07	0.23 +/- 0.01	0.24 +/- 0.03
7.2	77.7	0.61 +/- 0.02	0.38 +/- 0.03	0.32 +/- 0.03	0.24 +/- 0.03	0.20 +/- 0.01
7.2	96.0	0.63 +/- 0.03	0.37 +/- 0.02	0.29 +/- 0.03	0.25 +/- 0.02	0.20 +/- 0.02
9.2	23.6	0.45 +/- 0.06	0.30 +/- 0.03	0.21 +/- 0.03	0.13 +/- 0.05	0.15 +/- 0.04
9.2	42.8	0.52 +/- 0.02	0.34 +/- 0.02	0.26 +/- 0.02	0.21 +/- 0.04	0.17 +/- 0.02
9.2	77.7	0.51 +/- 0.02	0.33 +/- 0.03	0.25 +/- 0.02	0.21 +/- 0.02	0.17 +/- 0.01
9.2	96.0	0.58 +/- 0.02	0.37 +/- 0.01	0.30 +/- 0.01	0.22 +/- 0.01	0.21 +/- 0.01

Table A.3: Complete lag measurement data for a 6 MV x-ray beam.

Frame Time (s/frame)	Rad. Amt. (MUs)	$L_1$ (%)	$L_2$ (%)	$L_3$ (%)	$L_4$ (%)	$L_5$ (%)
5.2	1	0.80 +/- 0.03	0.43 +/- 0.02	0.31 +/- 0.02	0.25 +/- 0.01	0.206 +/- 0.008
5.2	2	0.81 +/- 0.02	0.429 +/- 0.008	0.30 +/- 0.01	0.23 +/- 0.02	0.19 +/- 0.02
5.2	3	0.78 +/- 0.01	0.400 +/- 0.009	0.271 +/- 0.003	0.206 +/- 0.004	0.166 +/- 0.007
5.2	4	0.79 +/- 0.02	0.40 +/- 0.02	0.28 +/- 0.02	0.21 +/- 0.02	0.18 +/- 0.01
7.2	1	0.60 +/- 0.02	0.34 +/- 0.02	0.24 +/- 0.02	0.187 +/- 0.009	0.17 +/- 0.02
7.2	2	0.60 +/- 0.02	0.33 +/- 0.02	0.24 +/- 0.02	0.19 +/- 0.02	0.17 +/- 0.02
7.2	3	0.60 +/- 0.03	0.33 +/- 0.04	0.25 +/- 0.03	0.20 +/- 0.02	0.17 +/- 0.02
7.2	4	0.57 +/- 0.01	0.31 +/- 0.02	0.22 +/- 0.02	0.17 +/- 0.02	0.15 +/- 0.02
9.2	1	0.50 +/- 0.04	0.30 +/- 0.02	0.22 +/- 0.02	0.17 +/- 0.02	0.15 +/- 0.02
9.2	2	0.51 +/- 0.04	0.31 +/- 0.03	0.23 +/- 0.03	0.19 +/- 0.02	0.16 +/- 0.02
9.2	3	0.51 +/- 0.06	0.32 +/- 0.04	0.24 +/- 0.04	0.20 +/- 0.04	0.17 +/- 0.03
9.2	4	0.48 +/- 0.03	0.29 +/- 0.02	0.21 +/- 0.02	0.17 +/- 0.02	0.15 +/- 0.02

Table A.4: Complete ghosting measurement data for 125 kVp x-rays.

Frame Time (s/frame)	Air Kerma ( $\mu$ Gy)	$C_1$ (%)	$C_2$ (%)	$C_3$ (%)	$C_4$ (%)	$C_5$ (%)
5.2	87	0.75 +/- 0.01	0.41 +/- 0.01	0.29 +/- 0.01	0.220 +/- 0.009	0.190 +/- 0.007
7.2	87	0.565 +/- 0.007	0.32 +/- 0.01	0.240 +/- 0.007	0.19 +/- 0.01	0.171 +/- 0.005
9.2	87	0.49 +/- 0.02	0.30 +/- 0.02	0.23 +/- 0.02	0.19 +/- 0.02	0.16 +/- 0.02

Table A.5: Complete ghosting measurement data for a 6 MV x-ray beam.

Frame Time (s/frame)	Rad. Amt. (MUs)	$C_1$ (%)	$C_2$ (%)	$C_3$ (%)	$C_4$ (%)	$C_5$ (%)
5.2	3	0.73 +/- 0.02	0.355 +/- 0.004	0.238 +/- 0.005	0.180 +/- 0.004	0.142 +/- 0.007
7.2	3	0.53 +/- 0.01	0.27 +/- 0.01	0.19 +/- 0.01	0.142 +/- 0.005	0.122 +/- 0.006
9.2	3	0.41 +/- 0.02	0.219 +/- 0.007	0.16 +/- 0.01	0.11 +/- 0.01	0.104 +/- 0.006